On the Separation and Composition of Liquid Crystals in Athabasca Bitumen

by

Kejie Wang

A thesis submitted to the Faculty of Graduate Studies and Research

in partial fulfillment of the requirements for the degree of

Master of Science

in

Chemical Engineering

Chemical and Materials Engineering

Summer 2015

Edmonton, Alberta

Abstract

Hydrocarbon-based liquid crystal domains have been identified in unreacted heavy fractions of petroleum from Athabasca bitumen and other hydrocarbon resources worldwide. These liquid crystal domains have also been shown to transfer from the hydrocarbon-rich phase to the water-rich phase during SAGD production, and primary separation of mined bitumen where their composition is enriched relative to bitumen and inorganic constituents. In this work, liquid crystal rich material was further isolated from SAGD produced water that also contains dispersed drops of bitumen rich material mineral matter and clay among its constituents. The physical and chemical isolation methods are described and the outcomes are validated using cross-polarized light microscopy and chemical analysis, including: elemental analysis and Fourier Transform Ion Cyclotron Resonance Mass Spectrometry (FT-ICR MS) using a negative-ion Electrospray Ionization (ESI) source (heteroatom class distributions, detailed DBE and O/C ratio). From the elemental and other analyses, the liquid crystal rich material is shown to include humic substances (humic acid, fulvic acid, humin) among the principal components as these are the only categories of species known to be present that have high enough oxygen contents to meet the mass balance constraint imposed by the elemental analysis. Naphthenic acids and other potential candidate species do not have high enough oxygen contents comprise a significant mass fraction of the constituents.

Acknowledgements

First and foremost, I thank my parents and my little sister, for their support, encouragement and love throughout my whole life.

I thank my supervisor Dr. John Shaw and my colleagues in the petroleum thermodynamic group. I especially thank Mr. Chuan Qin for training and instructions at the initial stage of my project, Ms. Mildred Becerra, for technical assistance, and Ms. Linda Kaert for administrative assistance – and cake on my birthday! I also thank Dr. Yongyong Li and Dr. Quan Shi for help testing samples using FT-ICR MS and instructions about data analysis at China University of Petroleum, Beijing.

The support from external collaborators is also important and I thank Mr. Nestor Zerpa (Nexen Energy ULC) for providing samples for analysis and for discussions regarding technical questions.

Table of Contents

List of Figures

List of Tables

Nomenclature

HC	Hydrocarbon
SAGD	Steam Assisted Gravity Drainage
CHWE	Clark Hot Water Extraction
PFT	Paraffinic Froth Treatment
NFT	Naphthenic Froth Treatment
FWKO	Free Water Knock Out
IGF	Induced Gas Flotation
ORF	Oil Removal Filters
FTIR	Fourier Transform Infrared Spectroscopy
ESI	Electrospray
FT-ICR	Fourier Transform Ion Cyclotron Resonance
MS	Mass Spectrum
OTSG	Once Through Steam Generator
PSV	Primary Separation Vessel
SARA	Saturate, Aromatic, Resin and Asphaltene
AB	Athabasca Bitumen
PLM	Polarized Light Microscope
ASRS	Anion Self Regenerating Suppressor
ANSA	1-amino-2-napthol-4-sulfonic acid
IC	Inorganic Carbon
DIC	Dissolved Inorganic Carbon
NDIR	Non-dispersive Infrared

FIA	Flow Injection Analysis
ICP	Inductively Coupled Plasma
RF	Radio Frequency
TOF	Time-Of-Flight
FFT	Fast Fourier Transform
RP	Resolving Power
KMD	Kendrick Mass Defect
NAFCs	Naphthenic Acid Fraction Components
HULIS	Humic-Like Substances
DOM	Dissolved Organic Matter
HVGO	Heavy Vacuum Gas Oil Fraction
HOA	Hydrophobic Acids

Chapter 1 Introduction

1.1 Liquid Crystals

1.1.1 What are Liquid Crystals

There are three classic states of matter: liquid, solid and gas. The liquid crystal state is an intermediate state between the liquid state and the rigid crystalline solid state. Liquids have no long-range order and flow. Rigid crystalline solids are ordered in three dimensions. Liquid crystals have order in one or two dimensions and do not lose the ability to flow [1]. The transition between solid and liquid crystal states is complex [2]. Here only three classic physical structures are discussed.

1.1.2 Types of Liquid Crystals

The nature of the liquid crystals formed is determined by molecular structure. There are three types as illustrated in Figure 1-1. Molecules in nematic liquid crystals tend to align in the same direction but have no positional order. Columnar liquid crystals have long-range order in two dimensions, where the molecules order in two dimensions to assemble together forming the discotic columns [3, 4]. Molecules in sematic liquid crystals tend to align in layers and the layers stack on top of one another.

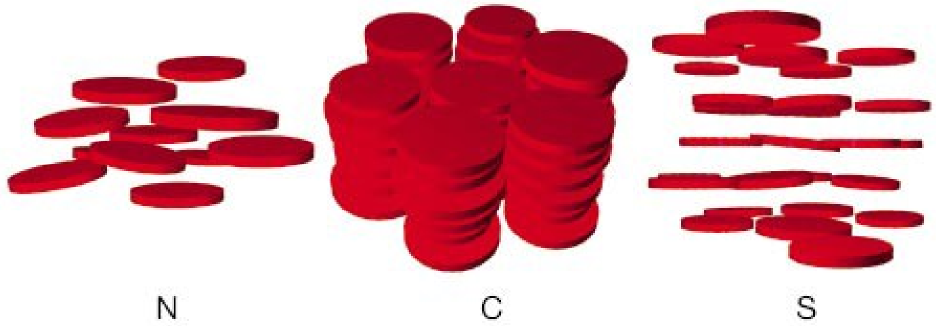

Figure 1-1 Structure schematic of the three classic classes of liquid crystals: the nematic phase (left), the columnar phase (middle), the sematic phase (right) [5]

1.2 Liquid Crystals in Petroleum

Petroleum is a complex mixture which consists of thousands if not millions of diverse compounds [6-14]. The important observation of liquid crystals in petroleum in 2010 contributes to a better understanding of the phase behavior and properties of petroleum [15]. Liquid crystals were observed in many unreacted petroleum fractions such as Athabasca, Cold Lake, Safaniya heptane asphaltenes and Maya pentane asphaltenes [16] since then. All of the liquid crystals exhibit thermotropic properties with varying phase transition temperatures to and from liquid crystal states. The liquid crystal forming temperatures are 340 K for Maya C5 asphaltenes, 338 K for Athabasca C5 asphaltenes, 341 K for Safaniya C7 asphaltenes and 371 K for Cold Lake C5 asphaltenes. The disappearance temperatures are: 423 K for Maya C5 asphaltenes, 435 K for Athabasca C5 asphaltenes, 433 K for Safaniya C7 asphaltenes and 431 K for Cold lake C5 asphaltenes. These materials also present transient liquid crystalline domains on exposure to toluene vapour at room temperature. Liquid crystals that exhibit both thermal and composition dependence are known as amphotropic liquid crystals. This is a key known attribute of the liquid crystalline domains in unreacted bitumen fractions. The nature of the liquid crystals (nematic, columnar and discotic) remains unclear [17]. Liquid crystalline domains have also been observed at oil-water interfaces [18, 19] where they influence the stability of water-in-oil emulsions [20]. Transfer of liquid crystal domains from the bitumen to the water-rich phase has been demonstrated in Steam Assisted Gravity Drainage (SAGD) facilities and laboratory measurements [21].

Qualitative and quantitative measurement of the mass fraction and composition of the liquid crystal fractions has proven challenging. One approach was to extract and analyze liquid crystal enriched asphaltene samples [22]. In this approach, C5 Athabasca asphaltene samples were placed on a glass slide and held at 418 K for one hour. On cooling the samples were immersed in a mixture of heptane 90 vol. % + toluene 10 vol. % for half an hour. Then the solution containing dissolved liquid crystal material was evaporated at 95 °C. In this way, approximately 0.5 mg of liquid crystal rich material was collected. Figure 1-2 shows that the molar mass range identified using FT-ICR MS for this liquid crystal enriched sample is from 200 to 500 and the most abundant compound classes are shown in Figure 1-3. The relative abundance of molecules with one sulfur atom (S_1), is greater in value than for unsubstituted compounds the hydrocarbon class (HC), and compounds with one nitrogen or one oxygen substitution (N_1 and O_1), and multipli-substituted compounds. The ordering of the compound classes for C7 Athabasca asphaltenes, Figure 1-4, differs significantly. While the difference is suggestive, and heteroatom substituted molecules may play an important role in liquid crystal formation, this result is not quantitative, and it must be interpreted with caution.

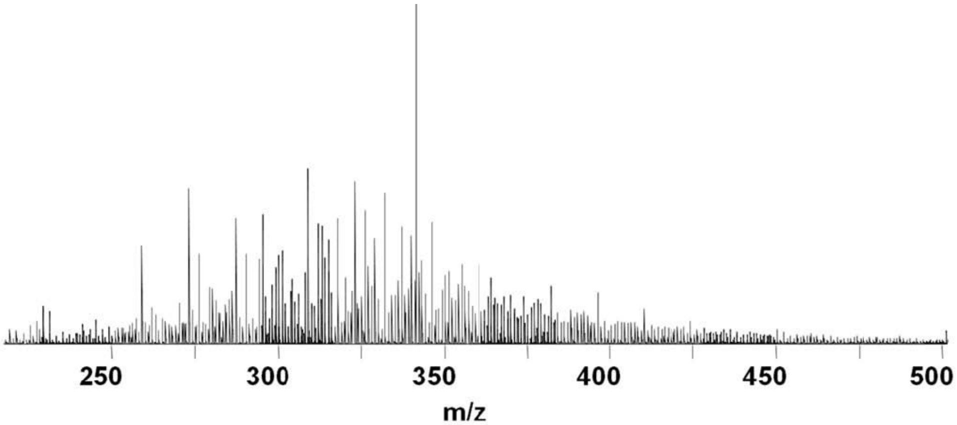

Figure 错误!文档中没有指定样式的文字。**-2** Broadband positive-ion APPI 9.4 T FT-ICR MS spectrum of liquid crystal-enriched C5-asphaltene fraction isolated from Athabasca bitumen [23]

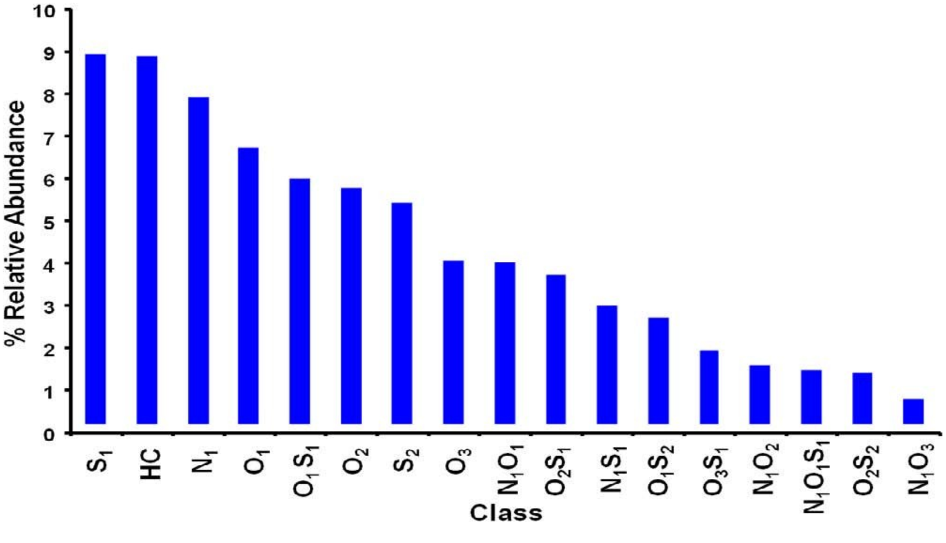

Figure 错误!文档中没有指定样式的文字。**-3** Heteroatom class distribution for liquid crystal-enriched C5 asphaltene isolated from Athabasca bitumen [23]

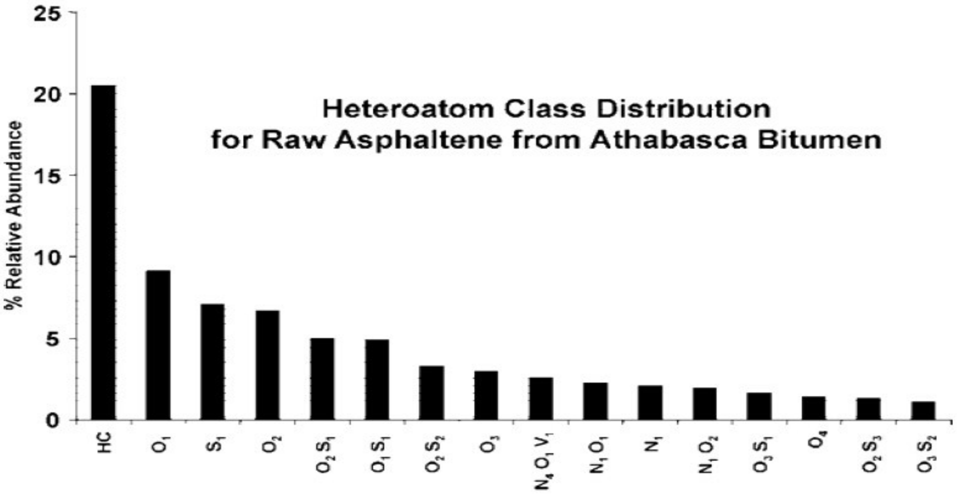

Figure 错误!文档中没有指定样式的文字。**-4** Heteroatom class distribution for Athabasca C7 asphaltenes [23]

1.3 Classes of Molecules That May Form Liquid Crystals in Petroleum

Many types and shapes of molecules form liquid crystals [24]. Illustrative examples are shown in Tables 1-1 and 1-2. These were chosen because they fall into compound classes, possess hydrogen to carbon ratios, and molar mass ranges that may exist in petroleum fractions. There are many additional examples in references [24-26]. As is clear from Tables 1-1 and 1-2, numerous compound classes identified in asphaltene and liquid crystal enriched samples include compounds that may form liquid crystals and the range of the search is not limited to a specific compound class.

Table 1-1 Compounds known to form liquid crystals [24-26]

Compound	**DBE**	**MM (g/mol)**	**H:C**
HC Class			
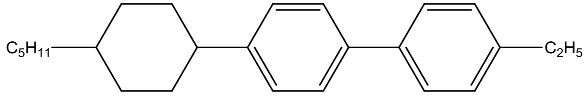 $C_{25}H_{34}$	9	335	1.36
S_1 Class			

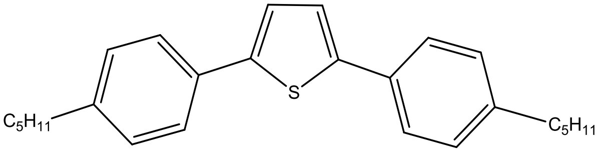 $C_{26}H_{32}S$	11	377	1.23
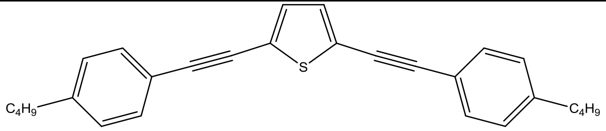 $C_{28}H_{28}S$	15	397	1
N_1 Class			
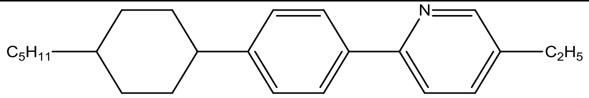 $C_{24}H_{33}N$	9	336	1.38
O_1 Class			
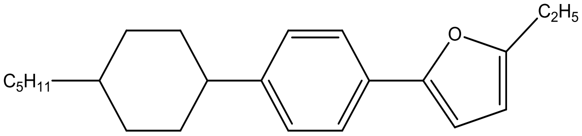 $C_{23}H_{32}O$	8	325	1.39
O_2 Class			
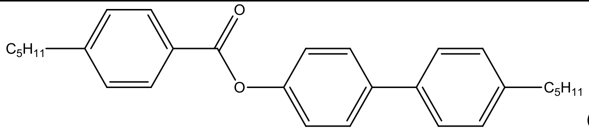 $C_{29}H_{34}O_2$	13	415	1.17
SO Class			
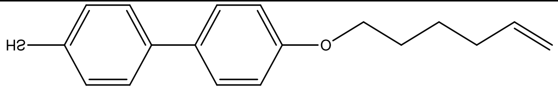 $C_{18}H_{20}OS$	9	284	1.11
SO_2 Class			
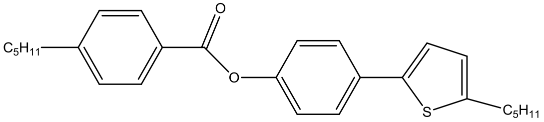 $C_{27}H_{32}O_2S$	12	421	1.19
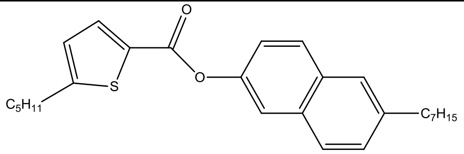 $C_{27}H_{34}O_2S$	11	423	1.26

Table 1-2 Multiclass mass compounds forming liquid crystals

<table>
<tr>
<td>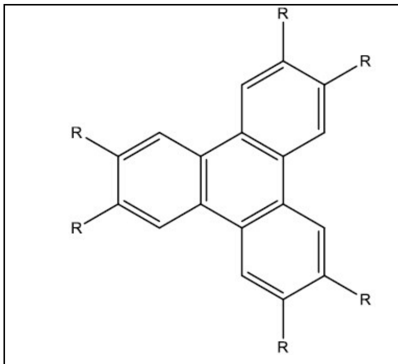 </td>
<td colspan="2">R
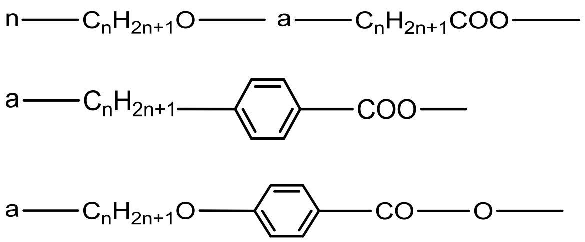 </td>
</tr>
<tr>
<td colspan="3">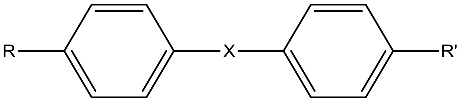 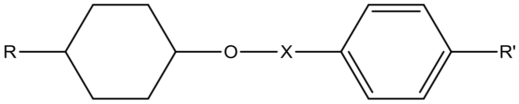
Elongated molecule</td>
</tr>
<tr>
<td>R</td>
<td>X</td>
<td>R’</td>
</tr>
<tr>
<td>$C_nH_{2n+1}-$</td>
<td>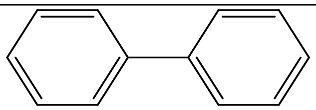</td>
<td>R</td>
</tr>
<tr>
<td>$C_nH_{2n+1}O-$</td>
<td>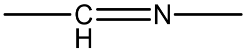$-CH=N-$</td>
<td>$-C\equiv N$</td>
</tr>
<tr>
<td>$C_nH_{2n+1}COO-$</td>
<td>– COO –</td>
<td>– Cl</td>
</tr>
<tr>
<td>$C_nH_{2n+1}OCOO-$</td>
<td>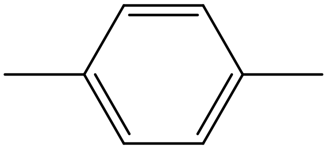</td>
<td>– Br</td>
</tr>
<tr>
<td></td>
<td>$-C\equiv C-$</td>
<td>– F</td>
</tr>
<tr>
<td></td>
<td></td>
<td>$-NO_2$</td>
</tr>
</table>

1.4 Bitumen recovery processes for surface oil sands deposits

1.4.1 Open-pit Mining and Water-based Extraction Processes

Approximately 20% of the oil sands lie close enough (<50 m) to the surface to be mined. Although the percentage of the near surface oil sands resource is not big, surface mining is critical to the oil sands industry in Canada. The primary extraction technology is the Clark Hot Water Extraction process (CHWE) which was first used in 1967, and has been subject of further refinement and development over time. This technology arose because there is a thin layer of water between individual sand grains and the surrounded bitumen [27]. Variants of this technology are used by Albian Sands Energy Inc., Suncor Energy Inc., Syncrude Canada Ltd., etc. A simplified schematic of one CHWE process variant is shown in Figure 1-5. Mined sand is crushed and mixed with hot water (50−80 °C) to form a slurry. The slurry is then pumped through a pipeline to the primary separation vessels (PSV) where bitumen is separated from the sand and recovered by flotation as bitumen froth. The recovered bitumen froth contains 10 wt % mineral solids, 30 wt % water and 60 wt % bitumen.

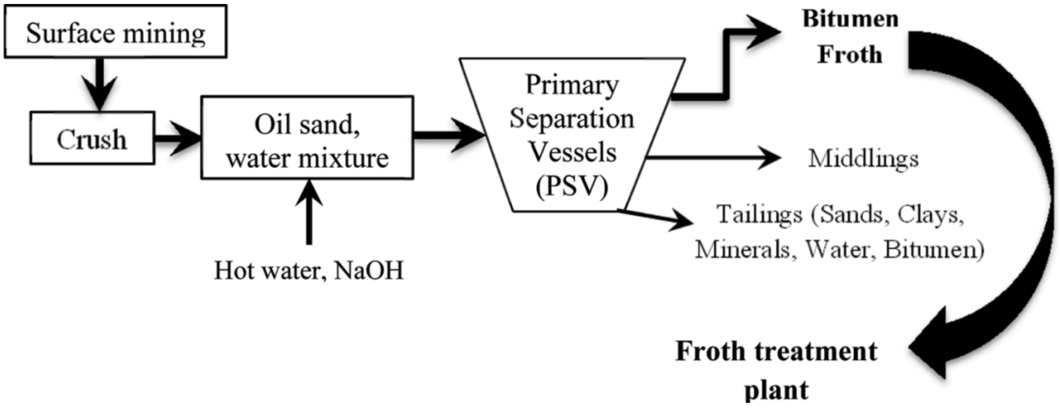

Figure 1-5 Schematic diagram of the surface mining and flotation process for the extraction of bitumen from oil sands [28]

1.4.2. Froth Treatment

Froth treatment is used to further separate the bitumen froth. Paraffin and naphtha, are two diluents, applied to lower the viscosity and density of bitumen froth to enhance the separation from residual sand and water. Paraffinic froth treatment (PFT) and naphthenic froth treatment (NFT) processes are both used industrially. Figure 1-6 shows a schematic of a two-stage NFT process. Multistage centrifugation and the application of demulsifiers are introduced to remove water-in-oil emulsions and solids from the diluent-bitumen solutions. Rag layers are mixtures of relative mineral particles, flocculated water drops and emulsions generated from centrifugation process in froth treatment. Liquid crystal-like behavior is observed in the model rag layers obtained in laboratory by Czarnecki and Moran [29].

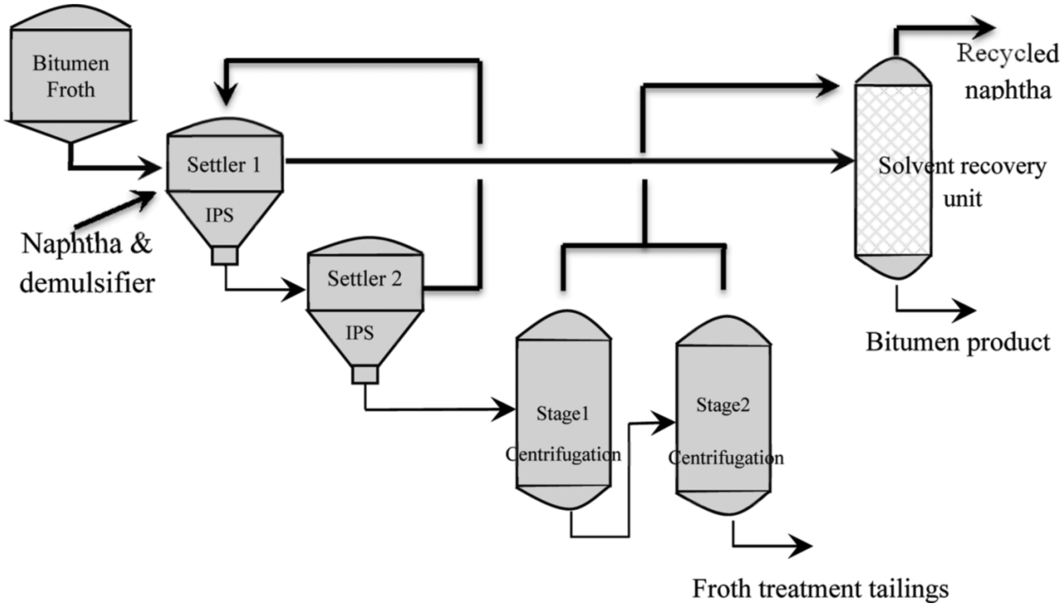

Figure 1-6 Schematic diagrams of bitumen froth treatment process with two stages [28]

1.5 Bitumen Recovery Processes for Deep-buried Oil Sands Deposits

1.5.1 Overview

In-situ oil sands lies more than 70 metres below the surface and are too deep to be mined [30]. About 80% of the oil sands in Alberta are classed as in-situ and production of this part of the bitumen resource is dominated by the application of the Steam Assisted Gravity Drainage (SAGD) technology. In this technology, high-pressure steam is injected into the deposit through a horizontal well (injector well) that heats the bitumen to lower its viscosity enough to flow. The liquefied oil migrates towards a producer well that is lower in the formation than the injector well by gravity alone. The emulsions of the produced water, bitumen, condensate steam and other gases are pumped from the producer well to the surface facility, leaving the sands behind. Figure 1-7 shows a schematic of a SAGD process.

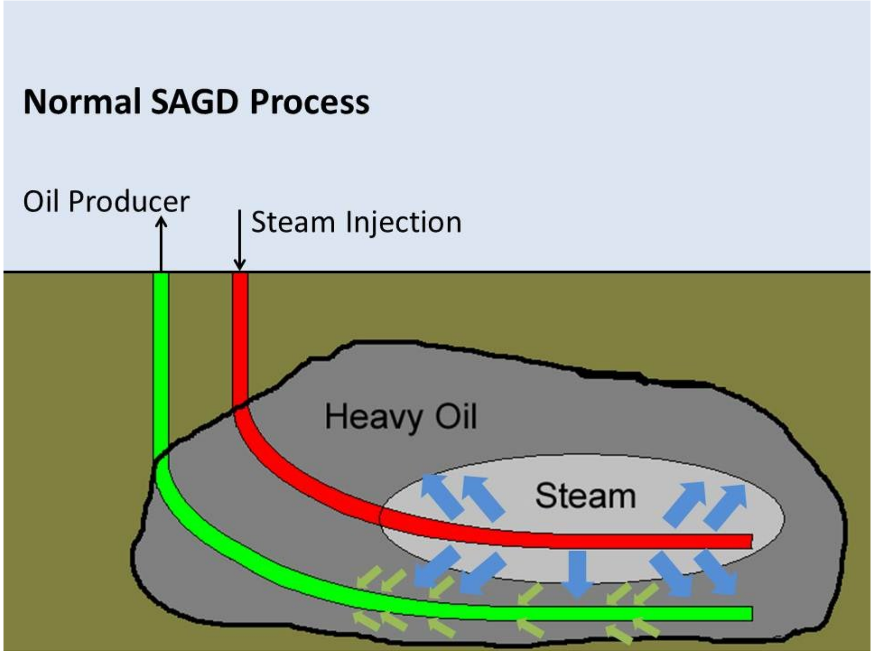

Figure 1-7 Schematic of Steam Assisted Gravity Drain (SAGD) process [31]

1.5.2 SAGD Produced Water Treatment Processes

The SAGD process requires large volume of water to generate the steam to heat the reservoir. The water is mainly groundwater instead of surface water. There are several reasons why the recycling of produced water is necessary. First, the water supply is limited; Second, produced water disposal is restricted; Third, if proper methods are applied to treat and reuse the produced water, process capital and operating costs can be lowered dramatically. Around 90% of the SAGD produced water is treated to meet water reuse quality requirements. SAGD water treatment includes de-oiling, where water is separated from the produced emulsion that mostly is bitumen, boiler feed water preparation, and steam generation and re-injection. The details of water recycling processes vary from operator to operator The Nexen Long Lake SAGD water recycle facility is described here with reference to Figure 1-8. Diluents and other chemicals (demulsifier, reverse demulsifier and inversion emulsion polymer, supplied by Baker Hughes Inc.) are added into the feed ahead of free water knock out (FWKO) drum to separate the oil from water by breaking the emulsion. The residual water is removed using an electrostatic grid treater connected with the FWKO drum. The water is then pumped into a skim tank, where sedimentation occurs before flowing into the second stage of water treatment. Induced Gas Flotation (IGF) connected with an Oil Removal Filter (ORF) followed with a de-oiling tank comprises the secondary de-oiling treatment. The oil content is reduced to less than 5 ppm by the ORF. Ca and Mg contents are then reduced using hot lime softening. Following secondary treatment the water is used to generate steam for re-injection.

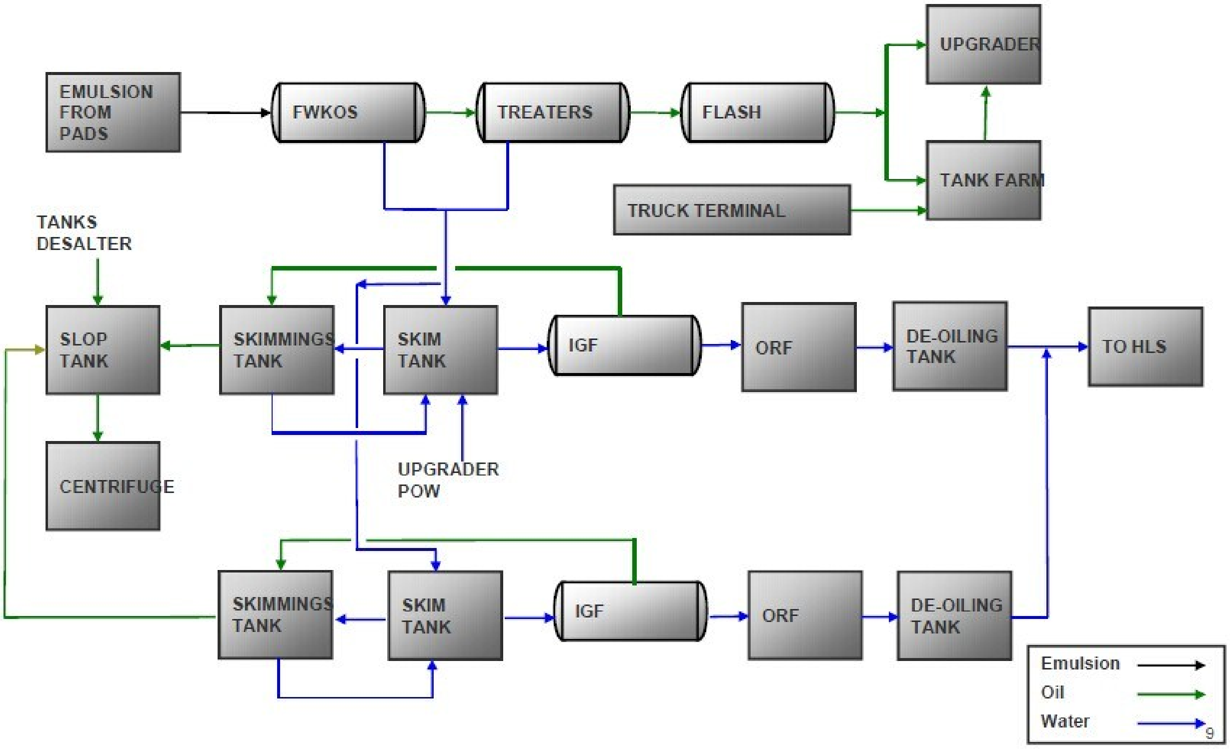

Figure 1-8 Schematic diagram of the Nexen Long Lake SAGD facilities [32]

1.6 Objectives and Thesis Outline

From the foregoing it is clear that the isolation of liquid crystal rich material directly from crude oil samples presents many challenges. As liquid crystal rich domains have been shown to transfer from bitumen-rich to water-rich phases both in the lab and in the field, the goals of this work are to isolate and then analyze the chemical composition of liquid crystal rich material from produced water samples obtained at the outlet of the FWKO drum at the Nexen Energy ULC Long Lake Facility. Large quantities of produced water are available and it is expected that large enough samples of liquid crystal rich material can be extracted from this source, so that reliable measurements can be made.

The balance of the thesis has the following structure. Chapter 2 concerns the development of techniques for the enrichment and isolation of the liquid crystal rich material from the water + Athabasca bitumen mixture. After a general treatment of the original sample, two methods of separation are tested and possible mechanisms for separation are discussed. Chapter 3 concerns the scale up of the separation methods and subsequent chemical analysis of the liquid crystal enriched samples. Elemental analysis (organic, inorganic and metal analysis), Fourier Transform Infrared Spectroscopy (FTIR) and Fourier Transform Ion Cyclotron Resonance Mass Spectrometer (FT-ICR MS) are applied to explore the chemical composition of the liquid crystals. In Chapter 4, the outcomes are discussed and then compared with the prior and current work of other researchers. Chapter 5 comprises the conclusions and recommendations for possible further work.

Chapter 2 Separation and Observation of Liquid Crystals in Water + Athabasca Bitumen Mixtures

2.1 Overview

While liquid crystals are readily detected using polarized light microscopy, several steps are required to separate liquid crystal rich materials from the water + Athabasca Bitumen mixture that comprises bitumen-rich domains, clay and other particles, and residual emulsion domains. In this work, after preliminary separation, two methods are used to further separate liquid crystal domains from this background: chemical deposition and the “coffee ring” effect [33, 34].

2.2 Materials

Water + Athabasca Bitumen Emulsion was obtained from the Nexen Energy ULC Long Lake facility. The sample point was the water rich effluent from the FWKO drum as shown in Figure 2-1. The emulsion sample included chemical reagents – a demulsifier, a reverse demulsifier and an emulsion polymer supplied by Baker Hughes Inc. Laboratory chemicals: toluene (assay 99.99 %) used for washing glass slides was supplied by Fischer Scientific; concentrated hydrochloric acid (assay 36.5-38.0%), supplied by Anachemia Canada Inc., was used to make dilute hydrochloric acid (~1 mol/L) to lower the pH.

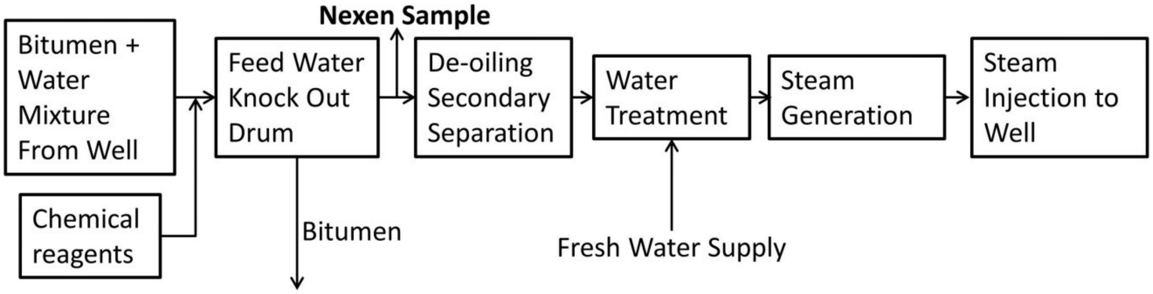

Figure 2-1 Schematic of SAGD water treatment process showing the sample point for the produced water sample

2.3 Experimental Apparatus

2.3.1 Simplified “Froth Treatment” System

The detailed configuration is shown in Figure 2-2. Samples were placed in the larger flask, that is connected to a second smaller flask within a vacuum oven (Model No.: 280A, Inside Dimensions 11.125”D x 9.75”W x 9.75”H, Vacuum Leak Rate: < 0.2” Hg per 24 hours, Temperature Range Ambient to 200°C) supplied by Fisher Scientific Inc.). Under vacuum at 80°C (353 K), froth was transferred from the larger to the smaller flask over a 30 minute interval. Aliquots of the froth were observed using cross polarized light microscopy. The residue was concentrated using a rotavapor, described below, prior to performing cross polarized light microscopy. In this way, the best source of liquid crystal enriched material that is as free as possible of mineral matter and oil drops could be identified.

2.3.2 Vacuum Rotary Evaporator

The rotary evaporator, shown in Figure 2-3, integrates a vacuum pump, vacuum controller and recirculating chiller into one reliable and easy-to-use system. The temperature range of the 4L water bath is 20 to 180°C (i.e. 293 to 453 K). The actual and set point temperature is shown on the large display continuously. In this work, the water temperature in the bath was set at 40°C and the temperature of the water in the recirculating chiller was 5°C.

Figure 2-2 Photo of “Froth Treatment” Reactor and heating system

Figure 2-3 Buchi R-210 Rotavapor: (1) Recirculating chiller, (2) Rotational velocity controller, (3) Vapor duct, (4) Distillate receiver (Receiving flasks), (5) Evaporating flask, (6) Height controller, (7) Heating bath, (8) Temperature controller, (9) LCD screen

2.3.3 Olympus GX 71 Inverted Microscope

An Olympus microscope (Figure 2-4, Model: GX 71) equipped with a polarizer (Model: GX-AN 360) and magnification objectives (Model: LM Plan FLN 5x, 10x, 20x, 50x and 100x) was used to observe samples and subsamples. An image acquisition and processing system is connected to the microscope so that images can be recorded and further processed using the Olympus Stream Software. Both cross-polarized light and normal light modes were applied in this work.

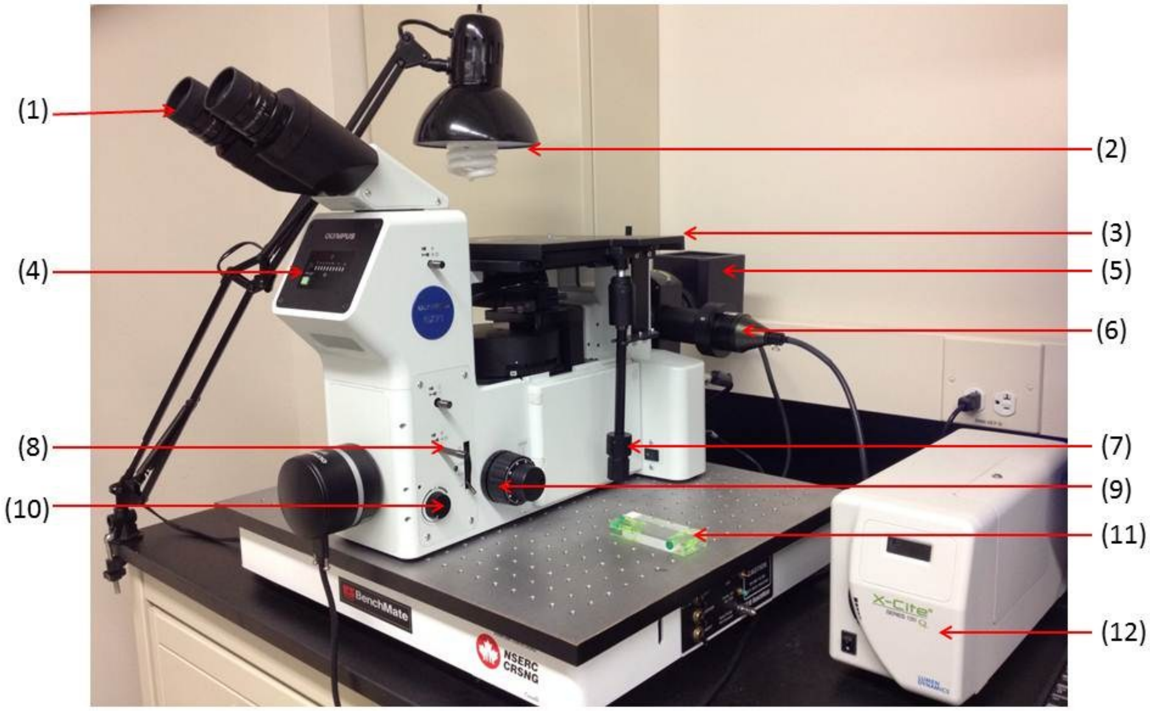

Figure 2-4 Olympus GX71 microscope system: (1) Ocular lens, (2) Natural light source, (3) Mechanical stage, (4) Light intensity indicator, (5) Halogen light source, (6) Fluorescent light connector, (7) Stage drive, (8) Digital camera switcher, (9) Focus adjustment knob, (10) Light intensity controller, (11) Bubble level gauge, (12) Fluorescent light source.

Cross polarized light microscopy is particularly useful for observing anisotropic materials like liquid crystals because anisotropic areas of a sample remain bright while the isotropic areas are dark when observed using cross polarized microscopy. The measurement principles are illustrated in Figure 2-5. The polarized light microscope has two polarizing filters in the optical path. One is located after the light source, the other one is placed between the sample and the observer. These two filters are perpendicular [35] so that the light which passes through the first filter is blocked by the second filter (analyzer) if the sample is isotropic. If the sample is anisotropic, it alters the direction of the polarized light and a fraction of it passes through the second filter to produce a Maltese cross, ring, or other pattern. Figure 2-6 shows what liquid crystal domains in Athabasca asphaltenes look like under cross polarized light.

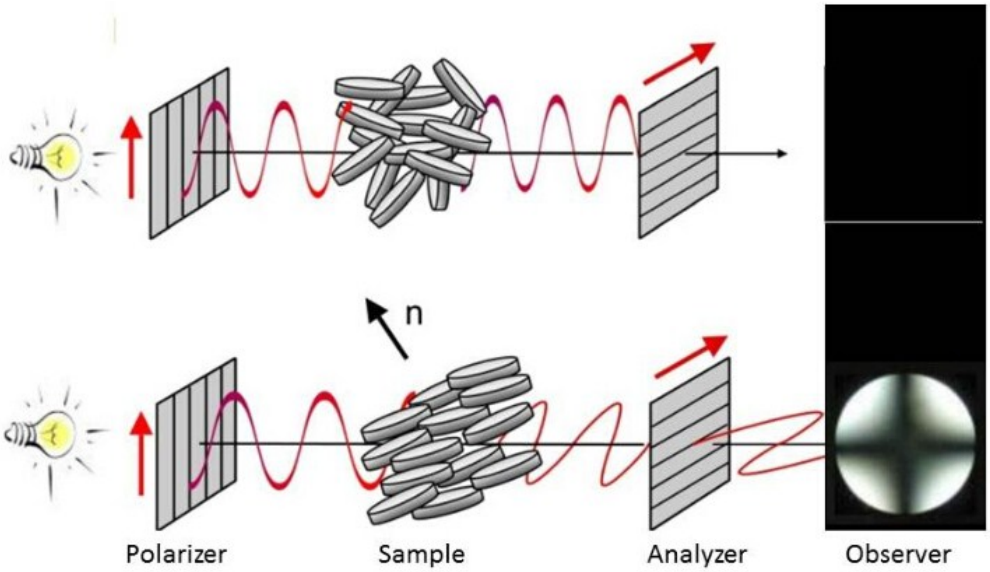

Figure 2-5 Principles of polarized light microscopy. Top image: isotropic or unordered samples under polarized light; bottom image: anisotropic or ordered samples under polarized light [21]

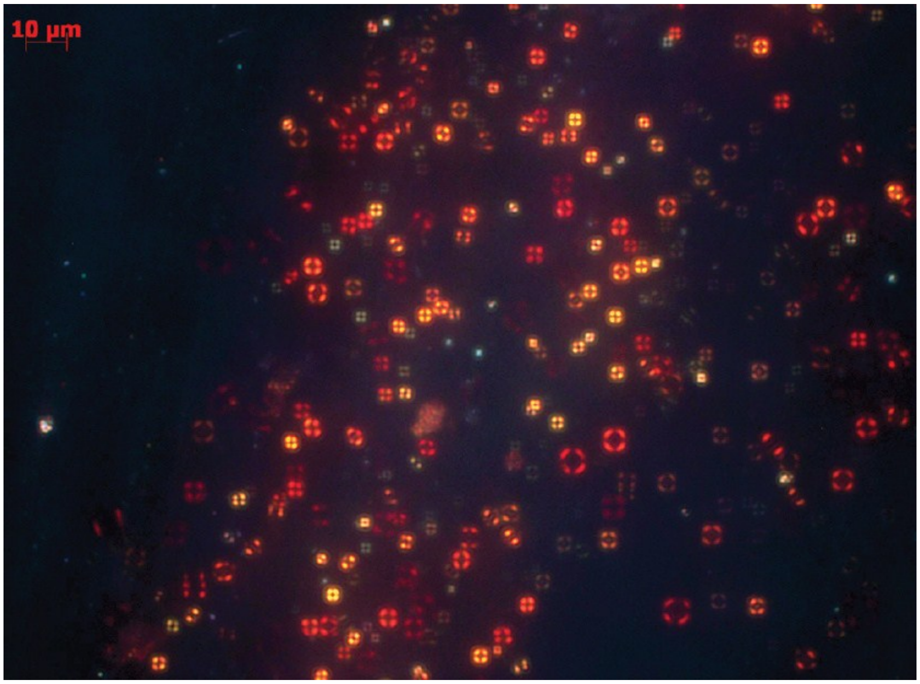

Figure 2-6. Liquid-crystal domains appear as Maltese crosses in Athabasca asphaltenes (C5) at 358 K. Reprinted from [36].

2.4 Liquid Crystal Enrichment

The froth treatment used in this work differs from the froth treatment process in industry, but the goals are the same: to decrease the influence of the aqueous contaminants and solids from the froth to make a cleaner product [37]. The Athabasca Bitumen + Water emulsion was placed in a flask and heated to 80°C for 30 minutes under vacuum. This temperature was chosen because bubble size and number and the stability of the froth inside of the flask influence the efficiency of separation. Microscopy observations showed that at this temperature, most of the mineral matter transferred to the froth and most of the liquid crystal domains remained with the residue. After 30 minutes, few bubbles were produced and the separation was halted. The physical appearances of the froth subsample comprising (~ 15 wt %) and the residue subsample comprising (~ 85 wt %) of the initial sample are shown in Figure 2-7. While it was possible to observe the froth subsamples directly under a microscope, residue subsamples were reduced to less than 15% of their volume in the Rotary Vacuum Evaporator at 40°C by evaporating water. The reduced residue subsample is referred to as “Sample 1”.

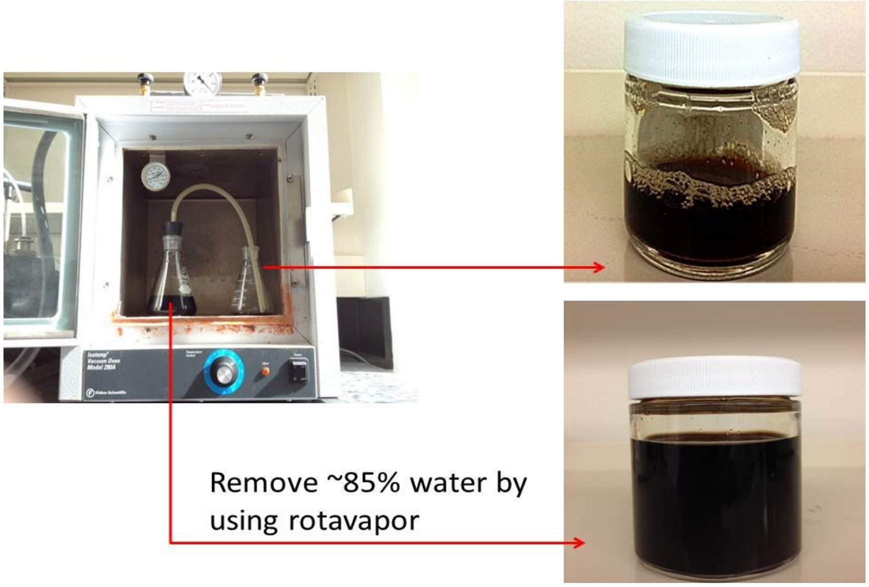

Figure 2-7. Appearance of the froth and residue subsamples.

2.5 Liquid Crystal Isolation

Liquid crystals were enriched in Sample 1, and both chemical deposition and physical deposition were used to isolate them further. The chemical deposition method was inspired by the work of Sundeep Srinivasa Rajagopalan and Jacob Masliyah [38, 39] who showed that in the oil sands process bitumen liberation was found to be influenced by water composition (pH, salt concentration) and the temperature. Bitumen liberation from the oil sand ore or mineral particles was promoted by high temperature and high pH values, while high salt concentration adversely affected bitumen liberation. In this work, the pH of Sample 1 was lowered to keep the mineral matter and bitumen together and to promote their deposition while leaving the liquid crystal rich domains suspended in the water. The pH of the sample was changed using a dilute hydrochloric acid solution. HCl was chosen because chloride is not present naturally in petroleum. Other acids such as HNO_3 and H_2SO_4 would introduce nitrogen, sulfur and oxygen, that would impact elemental analyses of the liquid crystals because petroleum, and bitumen in particular contain significant N, S, O contents. The appropriate pH range was found by reducing the pH of aliquots of Sample 1 from a starting value of 8 to values of ~ 6, 4, 2 and letting them settle overnight. Figure 2-8 (a) shows that samples with a pH of ~ 4 or less separate into two layers. The pH values for these preliminary tests were obtained approximately (pH indicator paper). A second set of measurements focused on the pH range 5 > pH > 3 and a pH meter was used. Samples separated into two layers for cases where the pH is ~ 3.3 (Figure 2.8 (b)) or less. Under these conditions bitumen, clay and other small mineral particles in the processed water sample settled in the lower layer (referred to as Sample 3). Dissolved inorganic salt and a fraction of the liquid crystal domains remained in the upper layer (referred to as Sample 2).

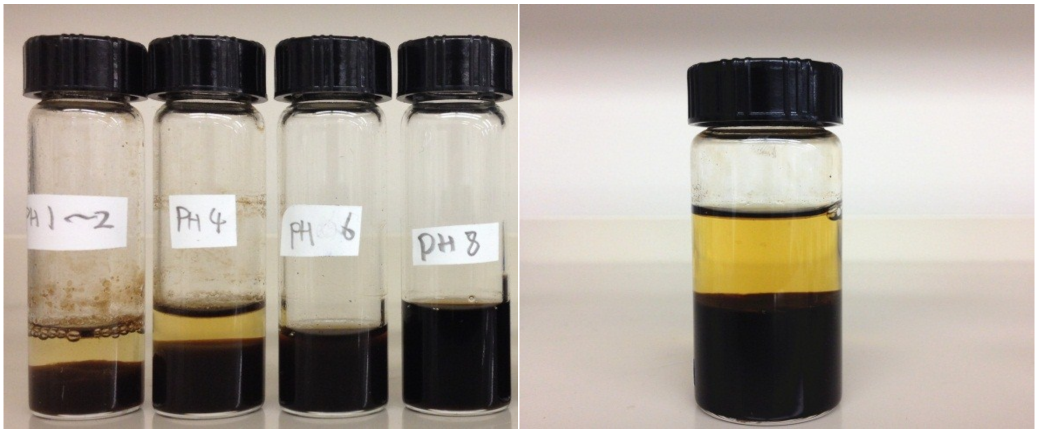

(a) **(b)**

Figure 2-8 Samples with different pH: (a) pH values are approximately 2, 4, 6, 8; (b) mixture at pH = 3.3

Physical deposition exploited the well-known coffee ring effect from colloid science where suspended particles in a drop of liquid migrate to the outer rim of the drop as the liquid dries on a solid substrate where they form a “ring”. The phenomenon, familiar to anyone who has observed the pattern of a dried coffee drop stain on a tabletop, is illustrated in Figure 2-9. There are three stages to the phenomenon for colloid sized drops suspended in a liquid: the drying stage; drop deformation at the rim; drop coalescence at the rim. During the drying stage colloids migrate to the rim and concentrate there. The colloids become pinned to the surface and to one another as the liquid evaporates. Once in contact with one another, colloid sized drops can pack, deform, and coalesce depending on their properties.

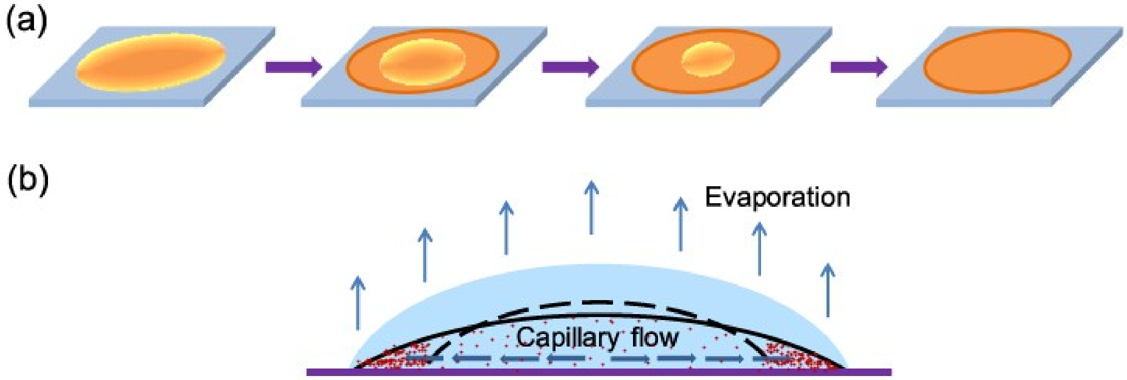

Figure 2-9 Schematic diagrams of (a) the drying process, (b) the evaporation process. Adapted from [40]

Physical separation of sample 1 was less successful as shown in Figure 2-10 a-c. drops of processed water, Figure 2-10 a, were placed on a glass slide using a syringe, Figure 2-10 b, and left to dry in air at room temperature (23°C), Figure 2-10 c. The rim area, from which Sample 4 was recovered, is dark and from a cursory microscopy inspection, liquid crystal domains are clearly mixed with bitumen and small solid particles. The central area is brown. Liquid crystal domains that were readily observed in sample 1 and 2 under polarized light do not appear to be selectively partitioned using this approach and chemical separated samples were selected for detailed study and chemical analysis.

(a) **(b)** **(c)**

Figure 2-10 (a) Bulk View of the processed water (Sample 1); (b) Sample 1 drop (~1cm in diameter); (c) Dried sample drop (Sample 4 and Sample 5)

2.6 Results and Discussion

2.6.1 Liquid Crystal Enrichment

A small number of liquid crystal domains can be observed in a drop of the process water using polarized light microscopy (Figure 2-11). Evaporation of the water in the droplet increases the local concentration of the liquid crystal domains. After “froth treatment”, most of the mineral matter, along with a few liquid crystal domains are eliminated - Figure 2-12 (a). In the center of Figure 2-12 (b), a few liquid crystal domains can be observed, but this inevitable loss of liquid crystal domains does not influence the enrichment of liquid crystal domains that occurs because most of the liquid crystal domains remain in the “froth treatment” residue. Their concentration along with the concentration of contaminants (small mineral particles, clay and bitumen) was concentrated by evaporating water from the residue as shown in Figure 2-13. In Figure 2-13 (a), the dark domains might be the mineral particles, clay and bitumen. For this reason further isolation was performed to obtain liquid crystal rich samples that were as free as possible from contaminants for further chemical analysis.

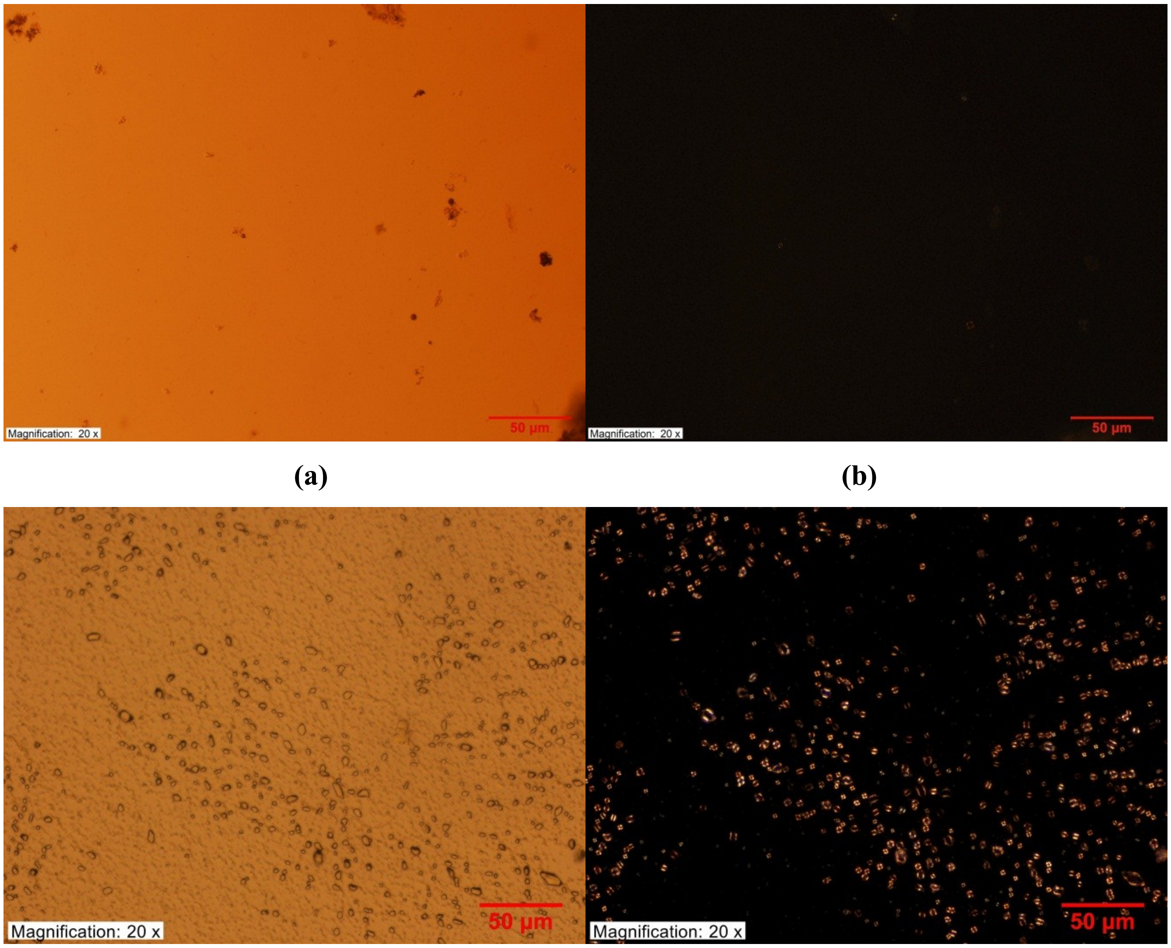

(a) **(b)**

(c) **(d)**

Figure 2-11. Raw sample: (a) raw sample under natural light; (b) raw sample under polarized light; (c) raw sample water-free residue under natural light; (d) raw sample water-free residue under polarized light

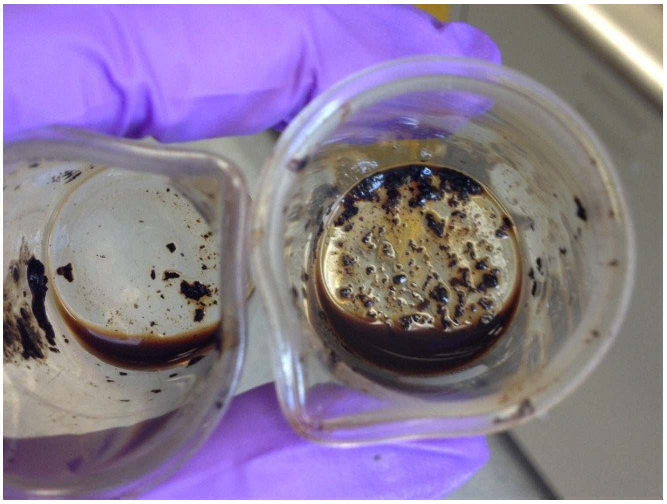

(a)

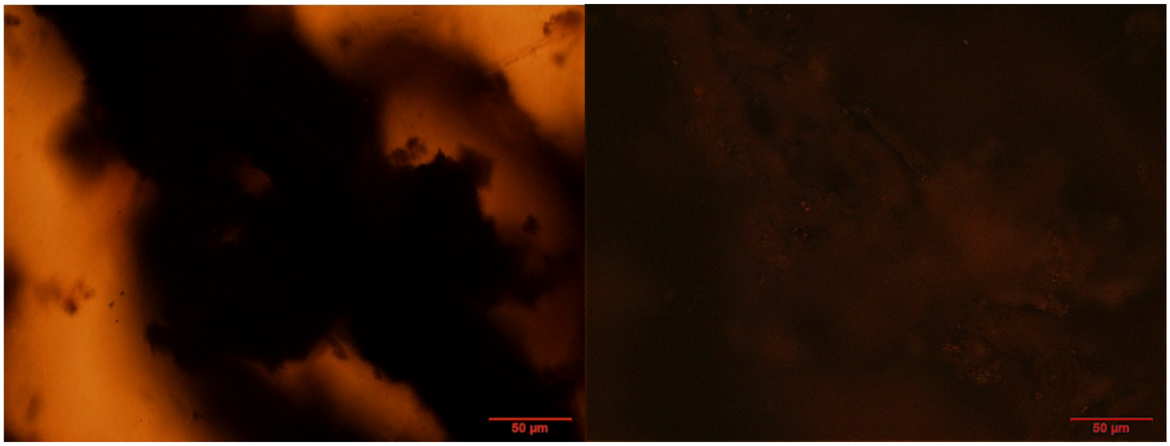

(b) **(c)**

Figure 2-12 (a) Bulk view of froth sample; (b) The microscope view of froth sample under natural light; (c) The microscope view of froth sample under polarized light

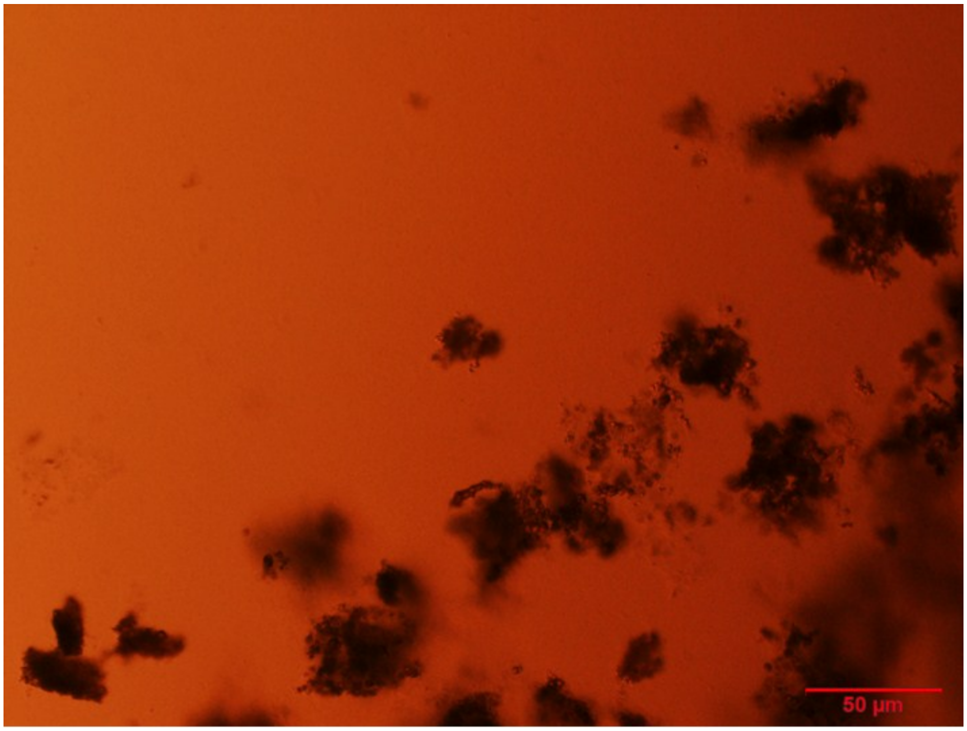

(a)

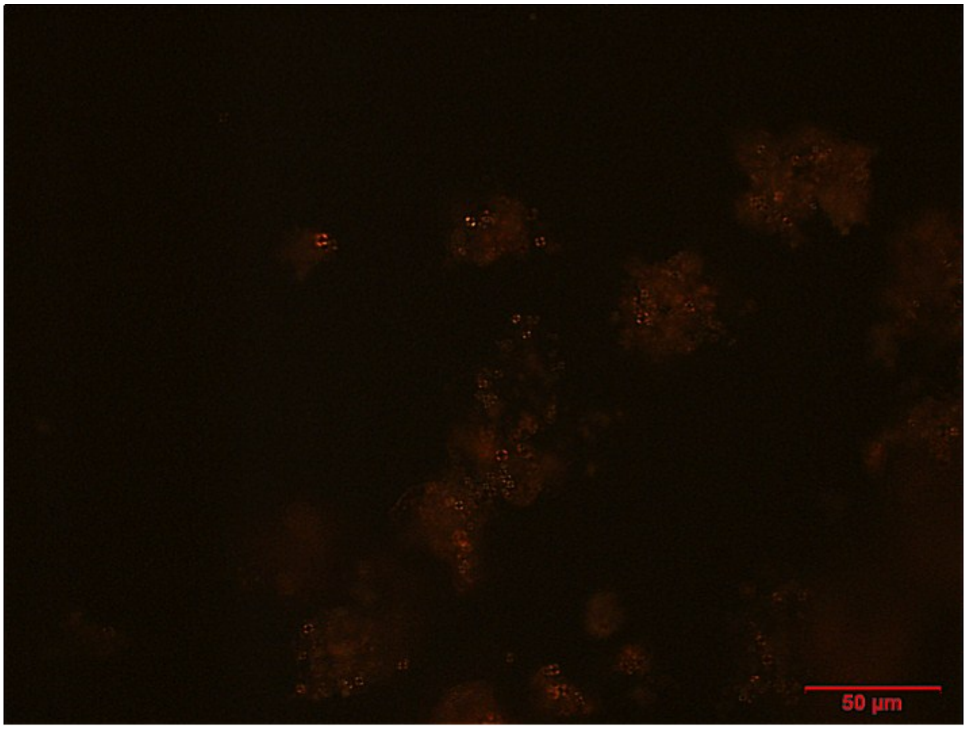

(b)

Figure 2-13 Processed water sample (Sample 1): (a) under natural light; (b) under polarized light

2.6.2 Liquid Crystal Isolation

The pH values of the samples in Figure 2-14 and Figure 2-15 were 3.3. In Figure 2-15, shiny streaks were observed under natural and polarized light. They were not liquid crystal domains. Bitumen was difficult to observe under polarized light as shown in Figure 2-14 and Figure 2-15 because bitumen is anisotropic and it is always mixed with mineral and clay particles. The post froth treatment sample (Sample 1) was separated to two layers. The upper layer was clear and is regarded as a liquid crystal rich sample with little interference with bitumen (Sample 2). The diameter of the liquid crystal domains ranged from 3 µm to 6 µm. The lower layer (Sample 3) is also liquid crystal rich but it remains mixed with bitumen.

The physical separation of Sample 1 is illustrated in Figures 2-16 and 2-17. In Figure 2-16, the edge area of an evaporated drop (from which Sample 4 was extracted) is shown under natural light and it might include liquid crystal domains and particles. From Figure 2-16 (b), the liquid crystal domains can be observed near the edge under polarized light. This area was black under natural light. This is attributed to the presence of bitumen, mineral matter and clay. In the central area of the evaporated drop, Figure 2-17, Maltese crosses (or rings) are not observed under polarized light. The ordered straight shiny steaks are not liquid crystals domains. According to these observations the central area, the source of Sample 5, might be similar to Sample 1 as only some of the liquid crystal domains moved to the edge area and most of the clays and mineral particles remained in the central area. The ordered shiny steaks might be formed by the inorganic components or the transform of the liquid crystal domains in the processed water sample.

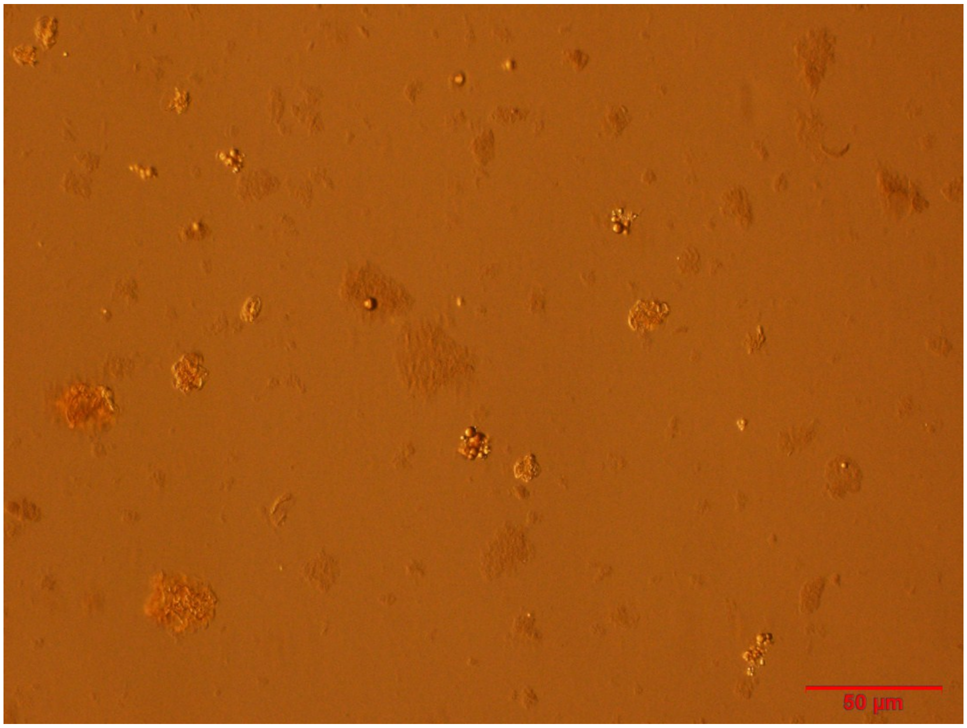

(a)

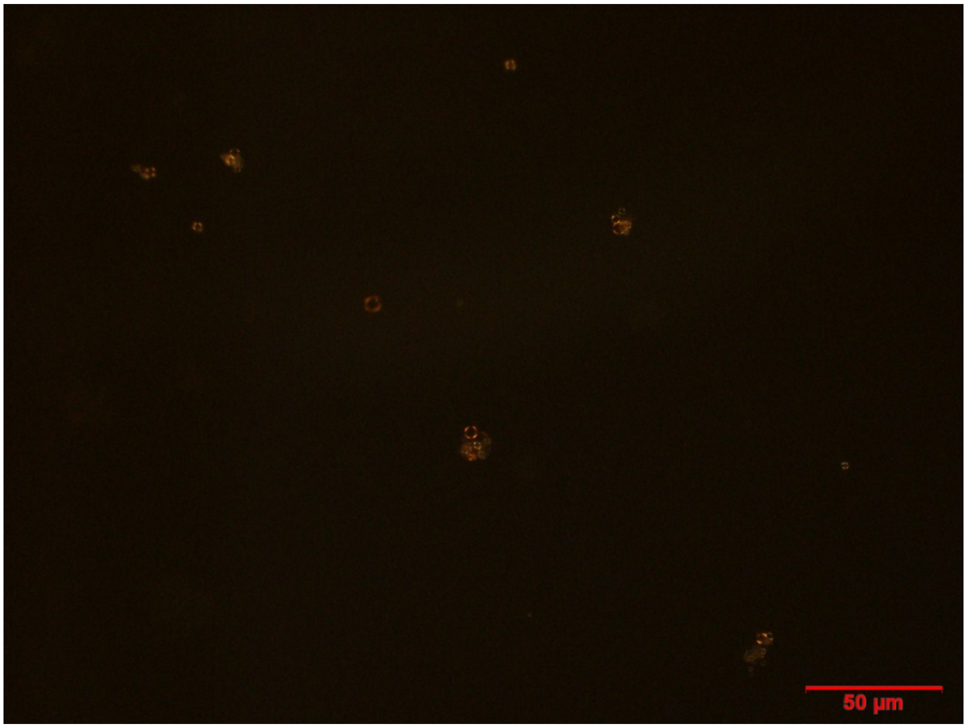

(b)

Figure 2-14 LC-rich sample with little interference from bitumen (Sample 2). (a) under natural light; (b) under polarized light

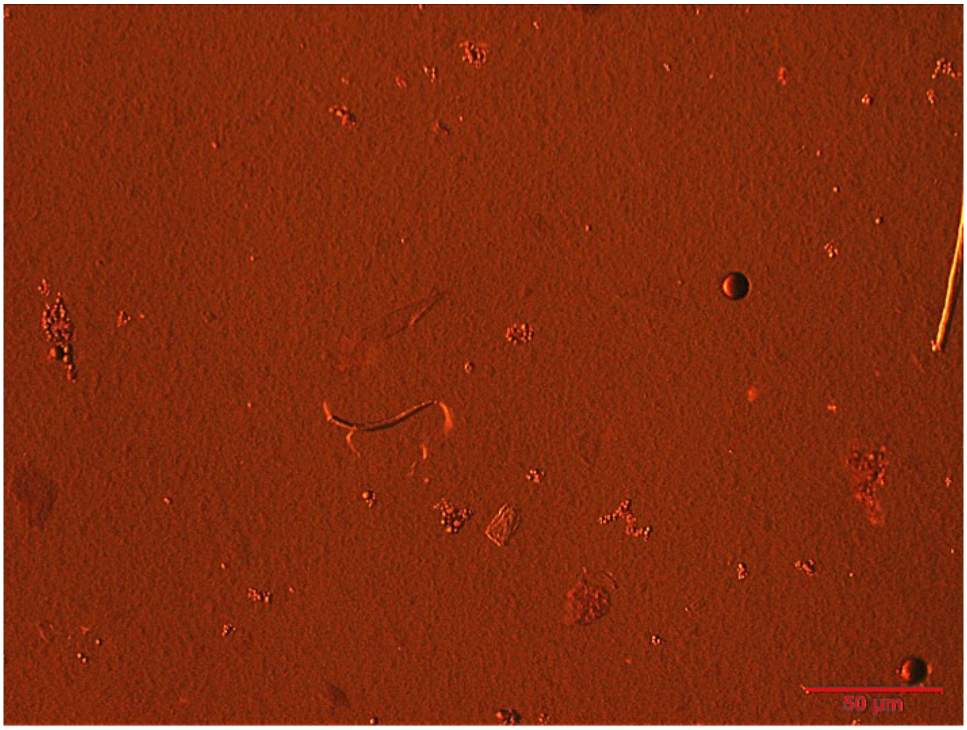

(a)

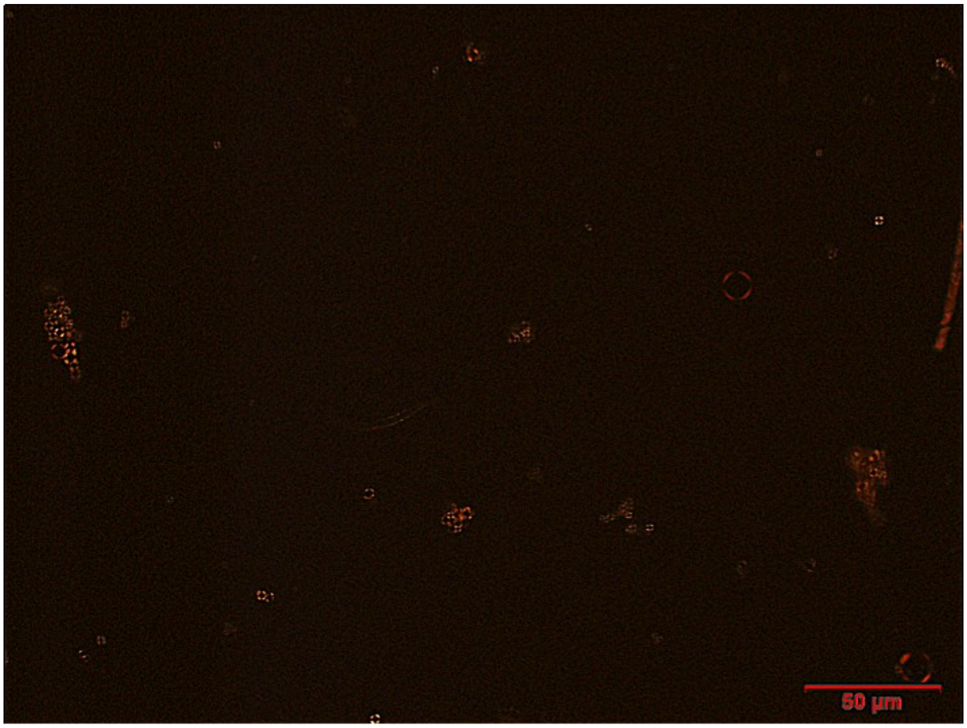

(b)

Figure 2-15 LC-rich sample mixed with bitumen (Sample 3). (a) under natural light; (b) under polarized light

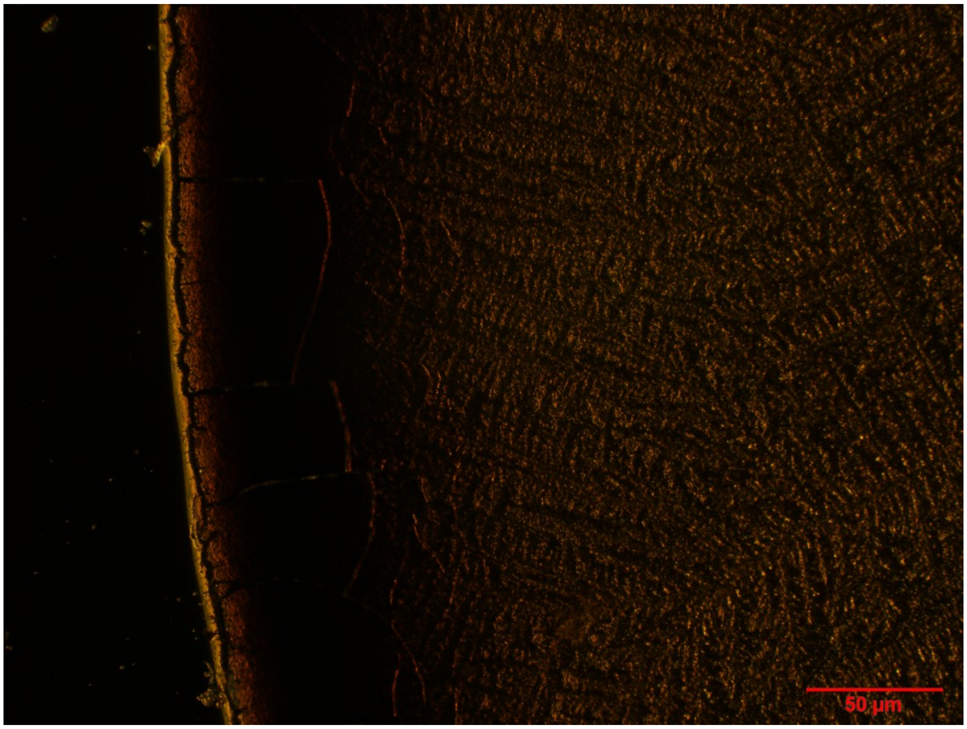

(a)

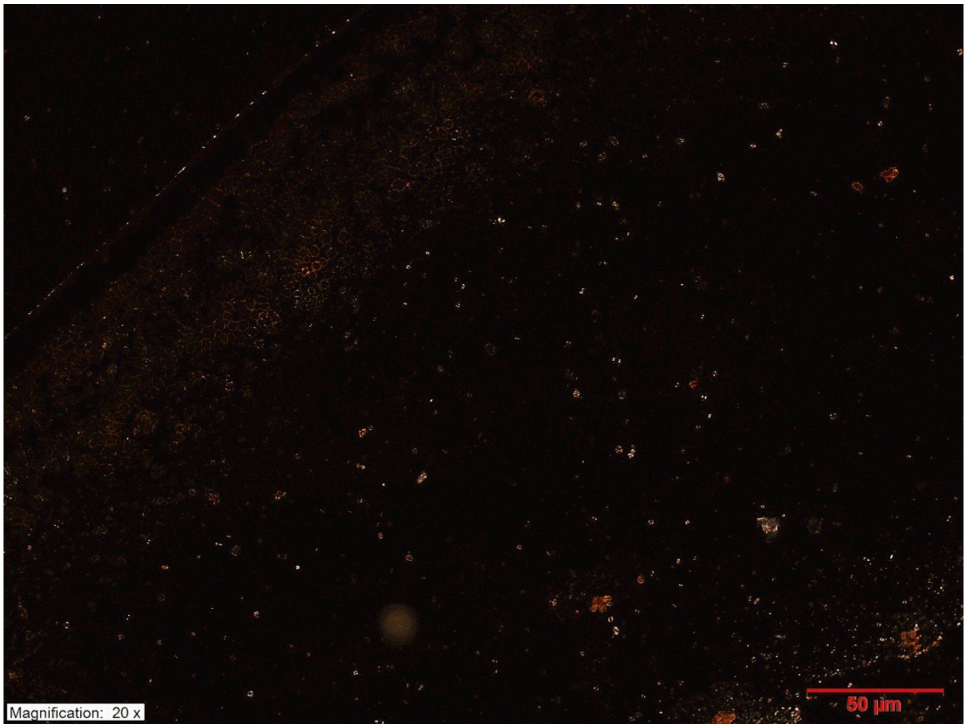

(b)

Figure 2-16 Edge area sample (Sample 4 dry): (a) under natural light; (b) under polarized light

(a)

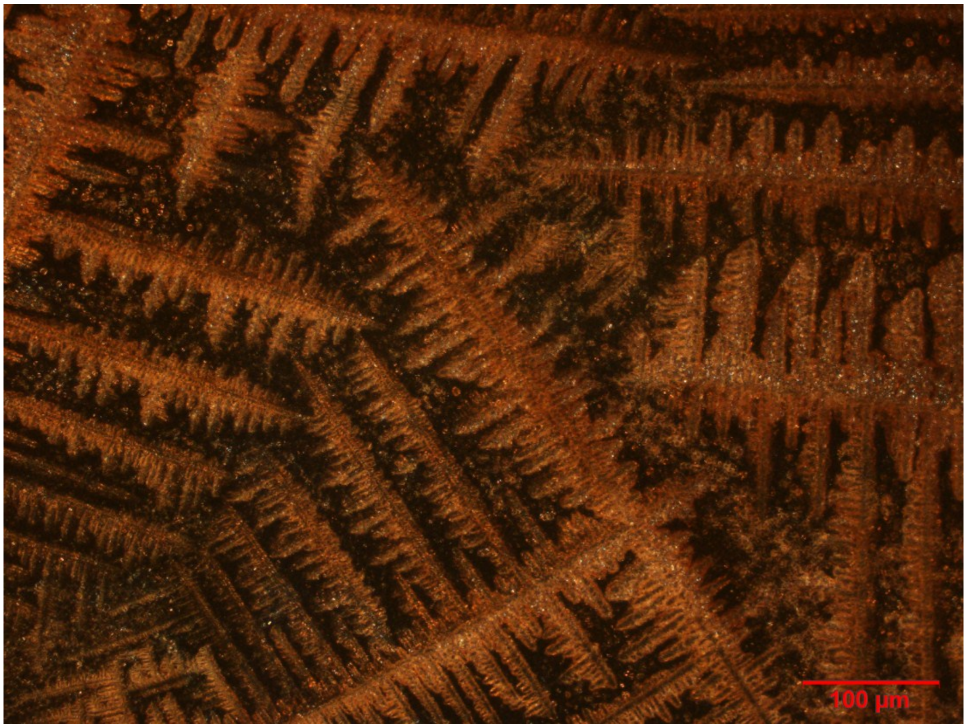

(b)

Figure 2-17 Central area powder sample (Sample 5 dry): (a) under natural light; (b) under polarized light

2.7 Summary

A SAGD process water sample was enriched in liquid crystal domains by froth treatment that removed most of the mineral matter and clay. This master sample, referred to as Sample 1, was further partitioned chemically by reducing the pH to yield a liquid crystal rich subsample largely free of contaminants, Sample 2, and a subfraction, Sample 3, with significant contamination with bitumen, mineral matter and clay. Sample 1 was also separated physically using the "coffee ring" effect by placing drops on a slide. Sample 4 was recovered from the edge area and Sample 5 from the central area of the evaporated drop. Based on their physical appearance, Sample 2, is the target sample for detailed analysis. The diameter of these liquid crystal domains observed in all samples ranged from 3 µm to 6 µm. Other observations are summarized in Table 2-1. The challenge of separating the liquid crystal shells from their isotropic cores remains unresolved.

Table 2-1 A brief description of the 5 samples observed in this work

Sample	Bulk view	Polarized light microscopy
1	Black, with sediments	Liquid crystal domains mixed with sediments
2	Bright yellow, transparent	Not so many liquid crystal domains but they are not mixed with bitumen
3	Deep black, with much floccule	Condensed liquid crystal domains mixed with floccule
4	Brown, with flocs	Liquid crystal domains are hard to be observed as they are condensed in the edge area and mixed with other materials
5	Black, with flocs	Liquid crystal domains are not observed because a salt formed when the drop dried

Chapter 3 Chemical analysis of liquid crystal rich material in Athabasca bitumen

3.1 Overview

The most promising separation methods identified in Chapter 2 were scaled up so that gram quantities of samples could be obtained for chemical analysis. Large scale sample production procedures are described and results from elemental analysis, Fourier Transform Infrared Spectroscopy (FTIR) and Fourier Transform Ion Cyclotron Resonance Mass Spectrometry (FT-ICR MS) where vapour phase samples were generated using Electrospray Ionization are reported.

3.2 Large Scale Sample Preparation

In Chapter 2, five samples were prepared and observed using polarized light microscopy. The samples comprised one or two small drops on glass slides and the quantities of recoverable material were very limited. This sample preparation procedure was scaled up by placing 25 or more drops on larger glass plates (20 × 20 centimeters) and then drying them for 90 minutes in a vacuum oven at 50°C. In this way, 30 mg batches were obtained, except with Sample 4. In this case, samples were only collected from the edge area of drops and the amount per batch was much smaller. At 50°C, and under vacuum, the rate of water evaporation was high enough but it did not further affect sample quality as the initial separation, described in Chapter 2, was performed at 80°C. Dried samples were then removed from the glass plates using a sharp blade. The procedure is illustrated in Figures 3-1 to 3-3. Images of wet and dried Sample 1 (Figure 3-1 a, and b) and Sample 2 (Figure 3-1 c and d) are provided. Sample 3 was prepared in the same manner. For these samples, all of the solids were scraped and collected (Figure 3-3) from the glass plates. Dried Sample 4 (outer edge area) and Sample 5 (central area) shown in Figure 3-2 were separated by carefully scraping the edge area of all dried drops and then the central area of all dried drops using the tip of a blade. The collected bulk samples are shown in Figure 3-3.

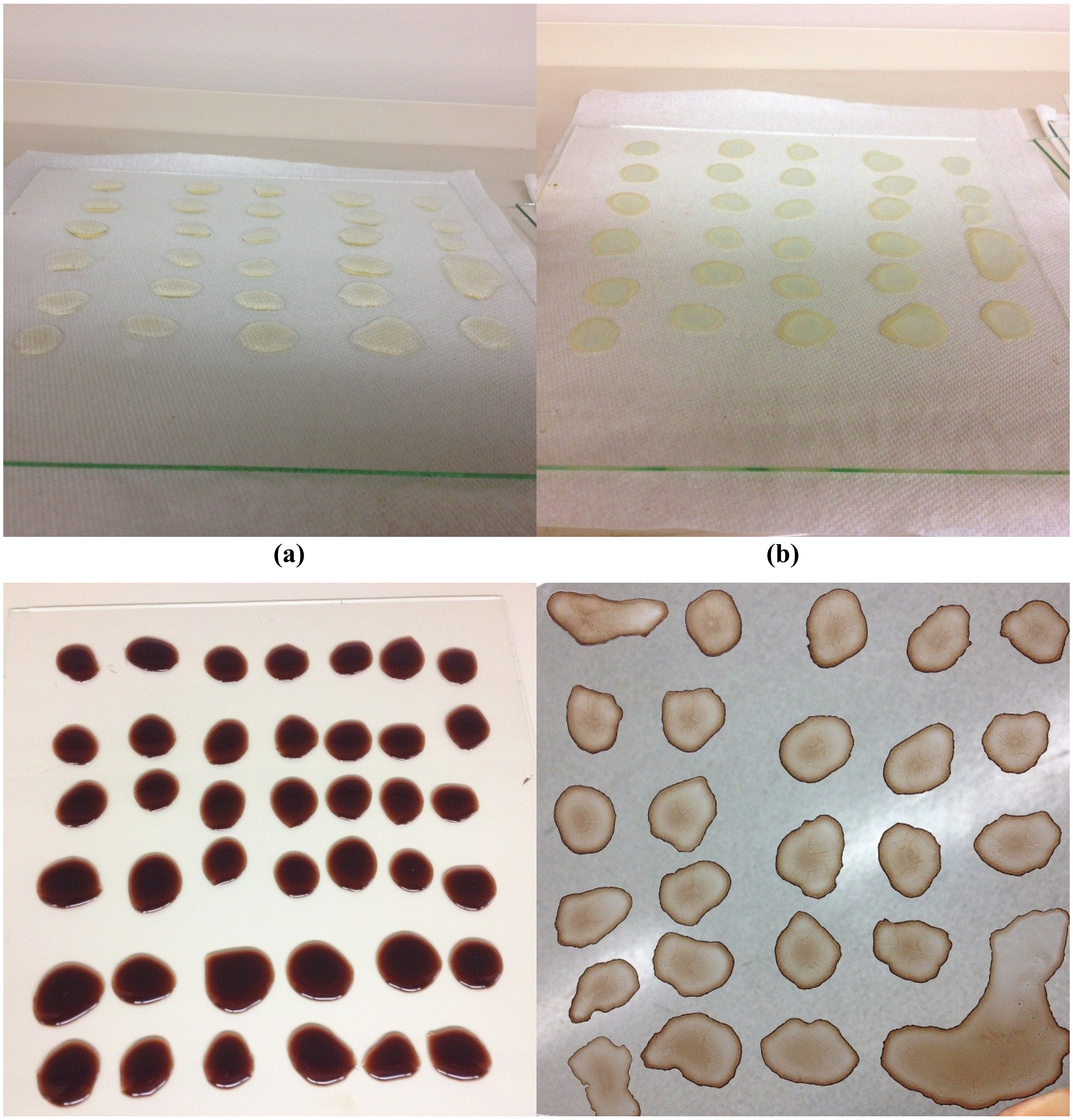

(a) (b)

(c) (d)

Figure 3-1 Illustration of the sample preparation scale up procedure: (a) wet, and (b) dried drops of the liquid crystal rich samples with little interference from bitumen (Sample 2); (c) wet and (d) dried drops of the processed water sample (Sample 1)

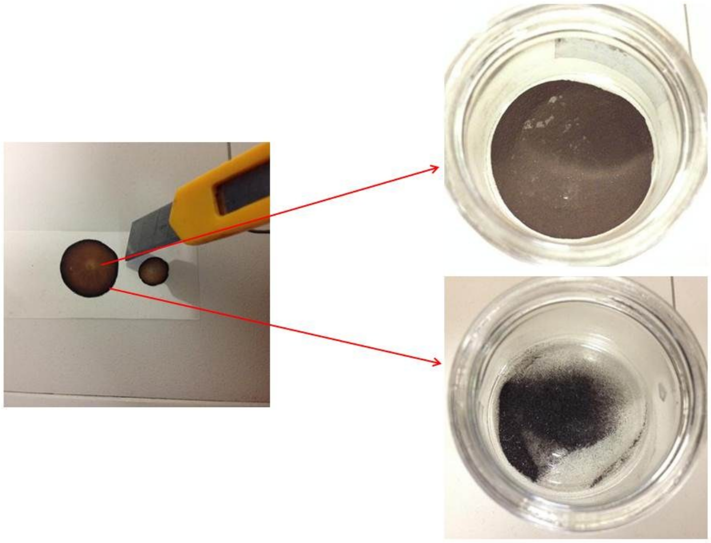

Figure 3-2 Images showing edge area sample (Sample 4, upper right) and central area sample (Sample 5, lower right) selection

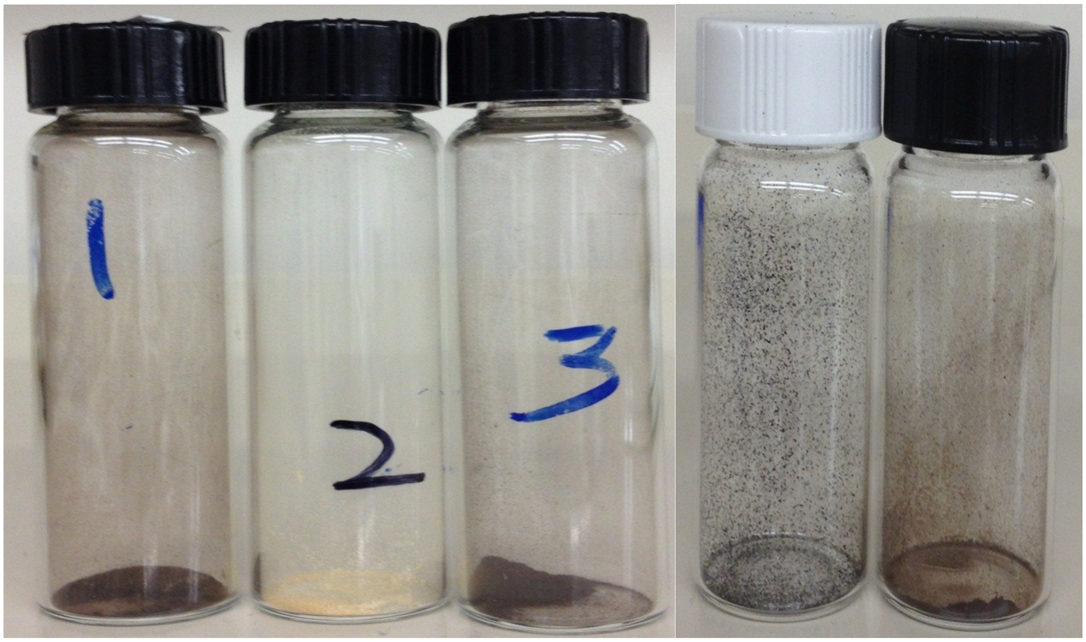

Figure 3-3 Bulk view of samples 1 to 5 (from left to right)

3.3 Analysis methods

3.3.1 Elemental analysis of organic and inorganic samples

Carbon, Hydrogen, Nitrogen, Sulfur and Oxygen analysis of organic materials were performed with a commonly used Flash 2000 CHNS/O Analyzer which quantifies carbon, hydrogen, nitrogen, sulfur, and oxygen in organic materials. In this work, the uncertainty of the measurements is +/- 0.14 wt%, +/- 0.05 wt%, +/- 0.06wt % and +/- 0.18 wt% for C, H, N and S respectively based on simultaneous analysis of samples with a mass of approximately 2.0 mg. Oxygen content is determined separately and has an uncertainty of +/- 0.09 wt %.

The procedures for the simultaneous determination of C, H, N and S contents in organic samples are summarized here. A sample containing tin cup is transferred into the combustion reactor using an autosampler swept with helium carrier gas to eliminate air. The combustion reactor is a vertical quartz tube maintained at 1000°C. The upper portion of the tube is filled with tungstic oxide (WO_3) on alumina – an oxidation catalyst. The lower portion is full of pure reduced copper wire. When a sample is in place, a small volume of pure oxygen is added to the helium carrier gas. The oxygen produces an environment which is highly oxidizing and samples burn completely. The carbon, hydrogen, nitrogen, and sulfur in samples are converted to CO_2, H_2O, NO_x, and SO_2 quantitatively. Extra oxygen is eliminated from the combustion chamber by reaction with the copper and NO_x is converted to N_2 [41]. The carrier gas (He) introduces the combustion products into a chromatographic column (Porapak QS, 4 mm ID, 2 m long), where the gases are separated and analyzed using a thermal-conductivity detector. Quantitative chromatographic peaks for carbon dioxide, water, nitrogen and sulfur dioxide are obtained and then displayed using Eager Xperience software.

The technique for oxygen determination in organic materials is based on the modified Unterzaucher method [42]. A sample is weighed in a silver foil container and put into a reactor heated to 1070 ºC to pyrolyze. Oxygen in the sample is quantitatively converted to carbon monoxide (CO) on a nickel coated carbon catalyst. The CO is separated from H_2,

N_2, and CH_4 in a chromatographic column (molecular sieve 5 Å) maintained at 65ºC, and quantified using a thermal conductivity detector.

The weight percentages of Carbon, Sulfur and Silicon in inorganic part of samples were analyzed using a Shimadzu 5000A TOC analyzer [43]. A minimum concentration of 200 mg/L and 40 ml volume (corresponding to ~8mg for samples 1-5) is required to guarantee the accuracy of the analysis. This corresponds to approximately 8 mg of samples 1-5. In this work, values for C, S, and Si content have uncertainties of +/- 0.20 wt %, +/- 0.01 wt % and +/- 0.15 wt %, respectively.

The procedures for the simultaneous determination of C, S and Si contents in inorganic samples are described here. Inorganic carbon is analyzed using a Shimadzu 5000A TOC analyzer (Shimadzu, Japan) and a simple sample analysis schematic is shown in Figure 3-4. Dissolved inorganic carbon (DIC) is defined as:

$$C_{DIC} = [CO_2] + [H_2CO_3] + [HCO_3^-] + [CO_3^{2-}]$$

The inorganic carbon (IC) reactor kit is applied to sparge the IC reaction solution (i.e. 75% orthophosphoric acid) together with the carrier gas. The samples are injected into the IC reactor vessel where IC reaction solution is filled, and all DIC is converted to volatilized carbon dioxide (CO_2):

$$CO_3^{2-} + 2H^+ = CO_2 + H_2O$$

$$HCO_3^{2-} + H^+ = CO_2 + H_2O$$

CO_2 is introduced into an infrared gas analyzer (NDIR) by the carrier gas, and total concentration of inorganic carbon is back-calculated against the calibration curve.

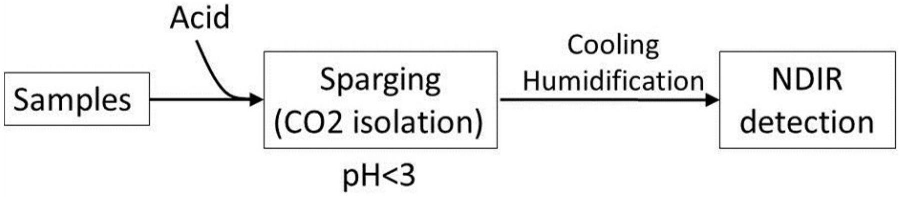

Figure 3-4. The schematic diagram showing the inorganic carbon analysis using Shimadzu 5000A TOC analyzer [43]

Sulfur in the anion (SO_4^{2-}) is detected using an ion chromatograph (Dionex DX600, Dionex, Sunnyvale, CA, USA). A small volume (50 µl) of sample is injected onto the anion separator column (Dionex AS9-HC column, 2 mm) protected by the anion guard column (Dionex AG9-HC, 2 mm). And SO_4^2 is detected with a conductivity detector (Conductivity cell, Dionex CD20). Data were generated using a Dionex Anion Self Regenerating Suppressor (ASRS, P/N 43187) and Dionex Peaknet Data Chromatography Software [44].

Inorganic silica in the samples is detected using a Lachat QuikChem 8500 Flow injection analysis (FIA) automated ion analyzer (Lachat Instruments, Colorado, USA). Dissolved silica compounds can react with molybdate in an acidic environment to form a yellow silicamolybdate compound which further reacts with 1-amino-2-napthol-4-sulfonic acid (ANSA) and bisulfite, producing a heteroploy blue complex which has a maximum absorbance at 820nm wavelength [45]. Absorbance at 820 nm is proportional to the original silica abundance in the sample. The standard flow injection analysis (FIA) equipment includes: an injection valve and an injection valve control; a Multichannel proportioning pump; a FIA manifold with flow cell and tubing heater that the example volumes and relative flow rates are detected as the schematic shown in Figure 3-5; an absorbance detector (820 nm, 10-nm bandpass) and data analysis system.

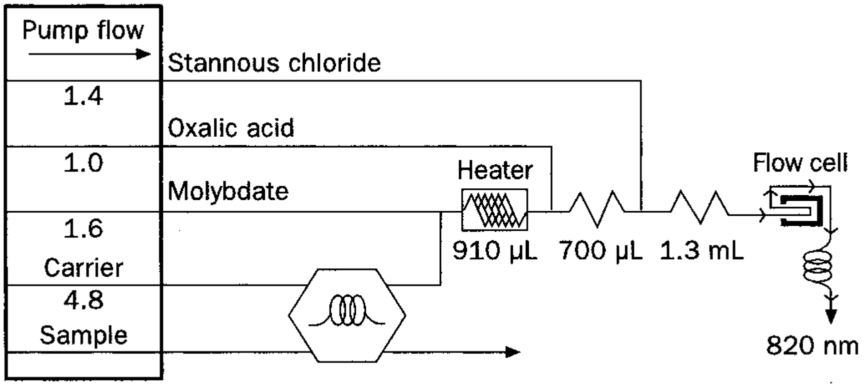

Figure 3-5 Schematic of flow injection analysis (FIA) manifold [45]

Metal element analysis was performed with an ICP-MS (Perkin Elmer 's Elan 6000). ICP-MS is comprised of Inductively Coupled Plasma (ICP) source maintained at high temperature and a mass spectrometer as the detector. The neutral forms of different species in the sample are converted to charged particles (i.e. ions), and introduced to mass spectrometer to be detected. Figure 3-6 mainly shows the schematic of an ICP-MS. There are concentric channels that are filled with argon gas in the ICP torch. A radio-frequency (RF) load coil is connected with a RF generator. Oscillating electric and magnetic fields are created at the end of the torch when the RF generator provides electrical power (1300W) to the load coil. As a spark is applied toe carrier gas inside the ICP torch, the electrons in the argon atoms are removed and argon ions are formed. Argon ions go into the oscillating fields to collide with other argon atoms to form a plasma or argon discharge. This plasma is a powerful ion source with a temperature of 6000-10000°C.

A sample is introduced into an ICP argon discharge which is full of high-energy particles as an aerosol. Gaseous atoms are generated from the elements of the samples. These gaseous atoms are then ionized and flow to the tail of the argon discharge. The desolvated ions (typically positive ions) are introduced to the mass spectrometer through two interface cones: the skimmer cone and the sampler cone that are metal disks with one 1mm hole in central area. The function of the interface cones is to sample the ions in the argon sample stream coming from the ICP torch and transmits the ions at higher pressure (100-300 Pa) to the low pressure (lower than 1 x 10^{-3} Pa in the detector (MS) [46]. The shadow stop (in Figure 3-6) is an ancillary equipment to block the photons that are from the ICP torch. Mass to charge ration of different charged ions are measured in mass spectrometer. There are three main types of mass spectrometers in ICP-MS instruments: time-of-flight (TOF), magnetic filter and quadrupole. The quadrupole was applied as the mass filter in the current work. The radio frequencies and voltages are changed by a quadrupole to ensure the ions of specific mass-to-charge ratio are stable within the robs that can therefore arrive in the detector, while other ions with different mass-to-charge ratio are ejected as they cannot go through. In order to cover a big mass range, the electrical power rapidly changes to control the conditions of the quadrupole to guarantee ions with different mass-to-charge ratio to go through. A dynode detector is used to count passed ions. When the passed ions strike the dynode, the active surface of the dynode will release electrons to trigger the amplification process: the released electrons from the first dynode would hit another dynode and more electrons are released and the electrons released from the second dynode would hit the third active surface and so on. This process continues until a measurable electrical pulse is produced. The instrument counts the ions that strike the first dynode by obtain the information of pulse generated by the detector [47].

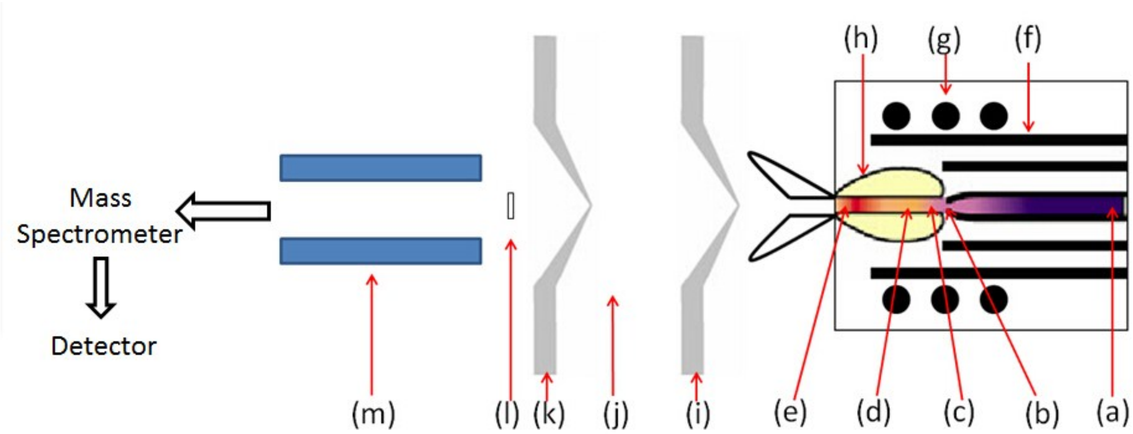

Figure 3-6 The schematic diagram of ICP-MS: (a) Aerosol; (b) Solid; (c) Gas; (d) Atoms; (e) Ions; (f) ICP Torch; (g) RF Load Coil; (h) Argon discharge (or Argon Plasma); (i) Sample Cone; (j) Vacuum; (k) Skimmer cone; (l) Shadow Stop; (m) Lens. [47]

3.3.2 Fourier Transform Infrared Spectroscopy (FTIR)

Infrared spectroscopy is used to identify functional groups in a sample. When infrared radiation passes through a sample, chemical bonds in molecules absorb energy at characteristic frequencies that generate different absorption peaks and are distinguished on this basis. Infrared spectra are unique for each sample, just like a fingerprint. Hence, the infrared Spectroscopy can differentiate and identify different kinds of materials, and the peak area reflects the relative quantity of a functional group [48]. A schematic of an FTIR is shown in Figure 3-7. An interferometer is used to measure all infrared frequencies at the same time. Two optical beams are generated from one infrared beam using a beam splitter in the interferometer. One beam reflects from a fixed mirror and the other reflects from a moveable mirror. The paths are different for the two beams, and the signal response in the beam splitter is the result of the interference of these two beams. The Fourier transform of the interferogram is the reported frequency spectrum [48].

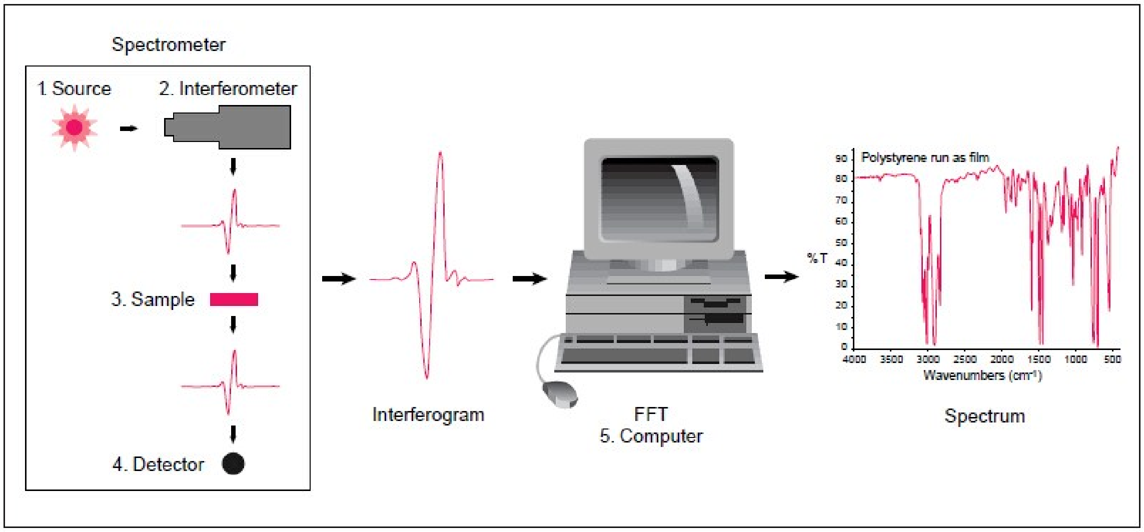

Figure 3-7 The schematic diagram of FTIR Spectroscopy [48]

In this work, a Thermo Scientific 8700 FTIR (Thermo Scientific, USA) is used with an attached Continuum FTIR microscope. OMNIC Series Software (Thermo Scientific, USA) is used to perform the Fast Fourier transform (FFT) to process the data. The KBr pellet method (~1-3% sample in KBr powder) was used [49], and scan range was 4000-400 wavenumbers. The five samples were put in a 50°C vacuum oven with caps opened to remove water absorbed from the environment. To quantify the effect of water absorption, an aliquot of Sample 2 was dried along with the five samples but in a sealed bottle.

3.3.3 Fourier Transform Ion Cyclotron Resonance Mass Spectrometer (FT-ICR MS)

FT-ICR MS is suitable for very complex mixtures (e.g. Athabasca bitumen), because it possesses ultrahigh resolving power (RP > 200000). RP is calculated as $m/\Delta m_{50\%}$, where $\Delta m_{50\%}$ is peak width at half-maximum peak height and very high mass accuracy (< 1 ppm).

FT-ICR MS instrument comprises four parts: an ion source, an ion accumulation (interface), an ion transmission and a detector. Electrospray ionization (ESI) source produces positively or negatively charged ions (only negative mode was performed in the current study) from polar molecules (e.g. molecules with functional groups like oxhydryl and carboxyl etc.). ESI is suitable for petroleum analysis because heteroatom-containing components (e.g. N, O, and S etc.) in petroleum are of high polarity, and can be easily charged in ESI and become gas-phase ions after desolvation. Though 90% of crude oil is hydrocarbon (CcHh), most problems in refining processes are caused by heteroatom-containing components (NnOoSs) [50]. A variety of compounds are ionized in order to generate a high resolution mass spectrum [51]. The details are thoroughly described in [52, 53]. Schematic diagrams of a FT-ICR MS and an ESI source are shown in Figure 3-8 and Figure 3-9, respectively.

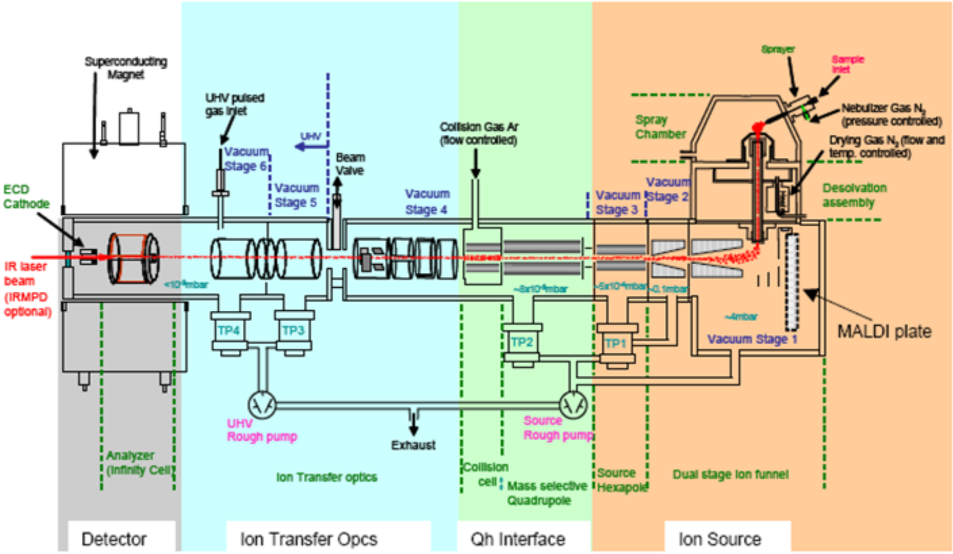

Figure 3-8 Schematic of the ion optics and pumping system of the apex-Qe FT-ICR MS [54]

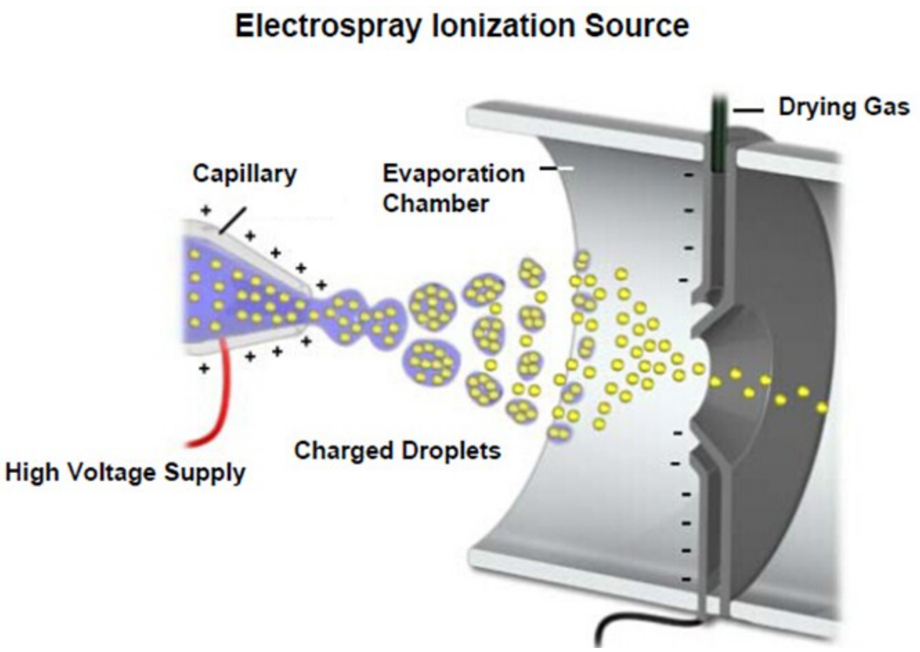

Figure 3-9 Schematic of an electrospray ionization unit. High voltage (0.5 - 4kV) is applied to the tip of the capillary through which dilute sample flows. Ions are converted into an aerosol spray and desolvation occurs along with dry nitrogen gas [55]

FT-ICR MS produces ultrahigh resolution mass spectrum. Positive-ion ESI/FT-ICR MS spectrum for methylated bitumen is shown as an example (Figure 3-10) [56]. The mass spectrum includes more than 8000 peaks with ~ 20 peaks at individual nominal mass [57]. The horizontal axis shows measured mass-to-charge ratio (m/z). Ions are usually singly charged, therefore, the measured mass-to-charge ratio is equal to molecular weight. Hence, data in Figure 3-10 indicates that molecular weights vary from 200 to 700 Da for methylated bitumen. The inset in Figure 3-10 is a zoom-in mass spectrum from m/z = 493.10 to 493.50, and different peaks in it represent different species in the sample.

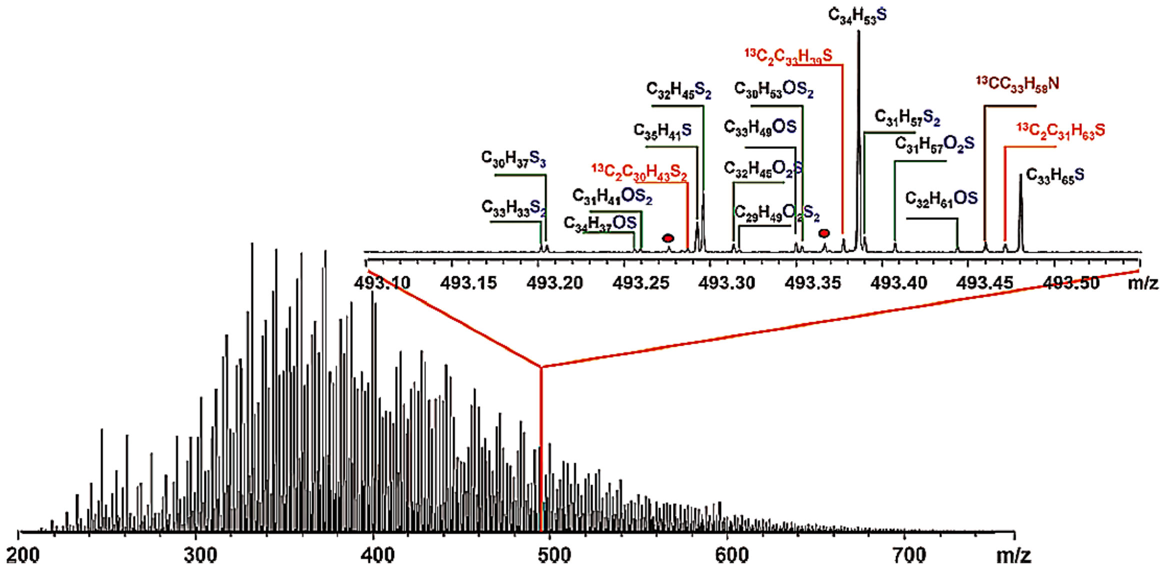

Figure 3-10 Broad-band positive-ion ESI/FT-ICR MS spectrum of the methylated bitumen. The inset shows an expanded mass scale spectrum at m/z 493. Compounds were identified based on mass measurement except for the two dotted peaks [56]

There are many compounds in petroleum. FT-ICR MS can help to explore the elemental composition of each corresponding peak in the spectrum, and compounds can be categorized into different classes or types. Compounds containing the same number of each heteroatom (nitrogen, oxygen, and sulfur) belong to individual classes, and those containing the same number of double bonds or rings [expressed as double bond equivalent

(DBE)] belong to additional classes. DBE measure the degree of unsaturation for compounds and is equal to the number of double bonds plus rings:

$$\mathrm{DBE}\ (C_cH_hN_nO_oS_s) = c - h/2 + n/2 + 1.$$

where c, h and n are the number of atoms of carbon, hydrogen and nitrogen in molecules. Oxygen and sulfur atoms do not contribute to the degree of unsaturation. From this definition, normal and branched alkanes possess DBE values of zero, regardless of molecular size. For aromatics and polynuclear aromatics, DBE values increase with the number of carbons in a molecule. For benzene (six carbons) the DBE = 4; for naphthalene (10 carbons) the DBE = 7; for phenanthrene (14 carbons) the DBE = 10; etc.

Results from FT-ICR MS analysis are presented as relative abundances of different types of heteroatom class (NnOoSs) and the DBE together with carbon distribution of the same type of heteroatom. The compounds with the same heteroatom class and same DBE belong to one group. The different number of methylene (CH_2) makes the relative molecular mass of these compounds differ an integral multiple of 14.01565.

In the current study, peaks with signal-to-noise ratio (S/N) ≥3 were imported into an Excel sheet and the measured m/z (i.e. relative molecular mass) were converted to the Kendrick Mass scale [58]:

$$\text{Kendrick Mass} = \text{IUPAC Mass} \times (14 / 14.01565).$$

The exact mass of CH_2 (14.01565) is converted to 14 by the Kendrick scale. The Kendrick Mass of different compounds which belong to one group differ an integral multiple of 14, while the decimal portions of the Kendrick Mass are the same. The Kendrick mass defect (KMD) is defined as the difference between the Kendrick mass and the nominal Kendrick mass which is the nearest integer of the Kendrick mass [59]:

$$\text{Kendrick mass defect (KMD)} = \text{Kendrick mass} - \text{nominal Kendrick mass}.$$

Therefore, compounds that only differ in numbers of CH_2 groups have identical KMD values. With high resolving power, the relative molar mass of all the ions are converted to KM. According to KMD, different classes and types can be detected quickly and precisely.

Three characteristics of samples can be obtained from the analysis of the data in FT-ICR MS spectra. With reference to methylated bitumen as an example [56], Figure 3-11 shows two characteristics: (i) the relative abundance of heteroatom classes (NnOoSs) (e.g. S_1, N_2S_1 and O_2S_1); (ii) the distribution of DBE for the within a heteroatom class. In Figure 3-11, different colors were used to represent the different DBE types. For instance, in Figure 3-11, the DBE of "S_1" class species varied from 1 to 18, and DBE = 2 – 11 are the major ones. The highest relative abundance of "S_1" class species is at a DBE=6. Another characteristic is the DBE and carbon number distributions for individual heteroatom classes. In Figure 3-12, the horizontal axis is the carbon number of the corresponding "S_1" class species, while the vertical axis is the DBE distribution. Dot sizes in Figure 3-12 represent the relative abundance of the compounds. DBE of "S_1" class species varies from 1 to 18, mainly at 2-11. The relative abundance of the compounds is high at DBE = 6 and 7. For "S_1" class species with 6 DBE, the carbon number varied from 14 to 47, mainly at 20-32. In this work, data obtained from FT-ICR MS analysis is presented in this manner.

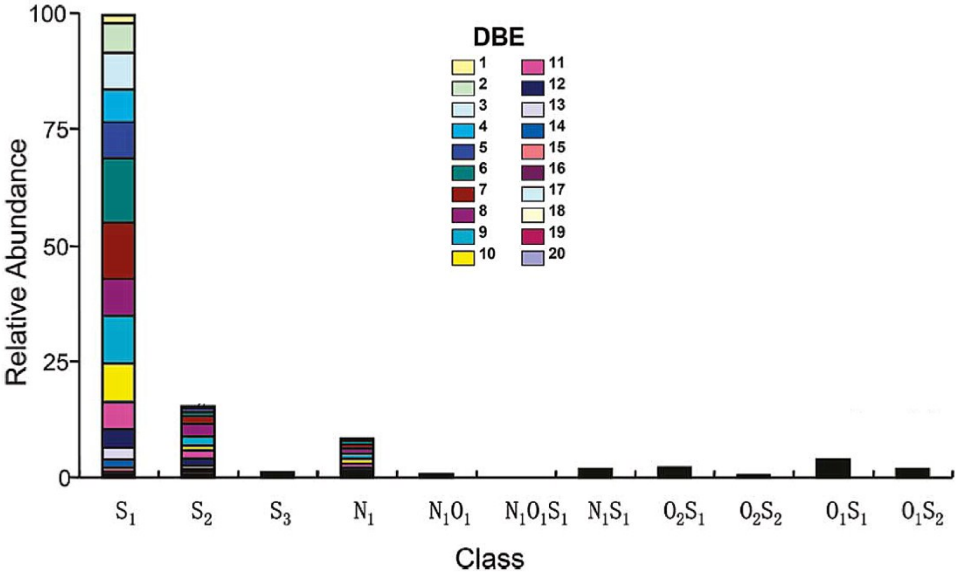

Figure 3-11 Heteroatom type, Double bond equivalent (DBE) and class (number of heteroatoms) distributions for methylated bitumen derived from a positive-ion ESI/FT-ICR MS spectrum [56]

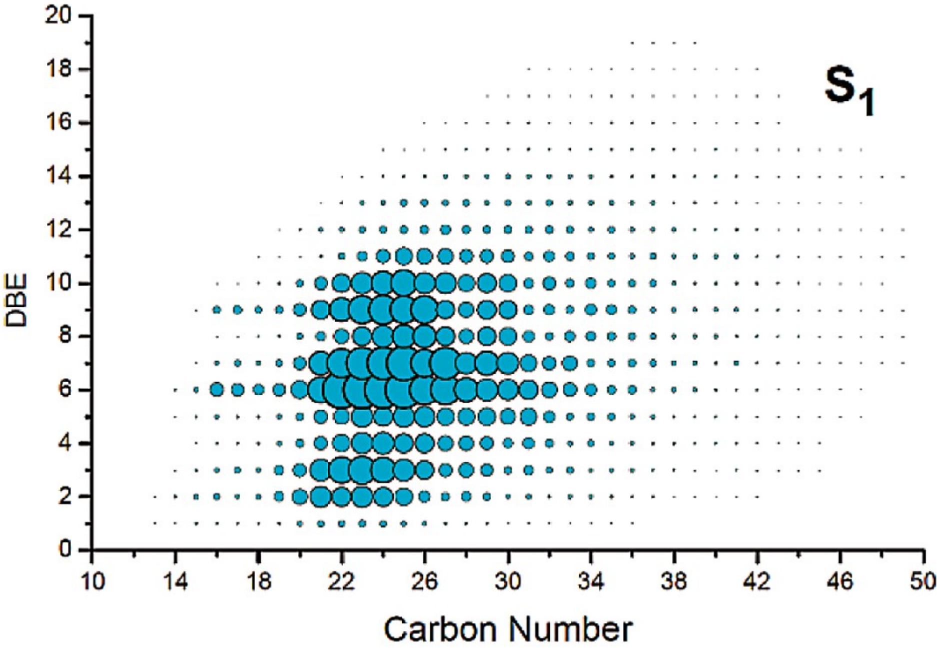

Figure 3-12 Plot showing DBE as a function of the carbon number for S_1 class species in methylated bitumen from positive-ion ESI/FT-ICR MS [56]

The five liquid crystal rich materials prepared as part of this work using physical and chemical deposition methods described in Chapter 2.5) were sent to a collaborating laboratory (State Key Laboratory of Heavy Oil Processing, China) for analysis on a 9.4 T FT-ICR MS (Bruker, Apex Ultra) equipped with an electrospray ion source (Bruker, Apollo II). The samples were dissolved in methanol and injected into the ESI source using a syringe pump. The operating conditions for negative-ion formation were: emitter voltage: 4.0 kV, capillary column introduced voltage: 4.5 kV, capillary column end voltage: -320 V. Mass range was set to m/z 150−1000. The word size of time domain data acquisition was 4 M. A number of 128 scan FT-ICR data sets were accumulated to enhance the dynamic range and signal-to-noise ratio. Prior to ESI/FT-ICR MS analysis, the samples are mixtures of organic and inorganic material. Considering that the inorganic compounds in the samples may influence the result, all of the samples were desalted during the experiment. Details are discussed in Chapter 3.

3.4 Results

3.4.1 Elemental Analysis

Brief descriptions of the five samples analyzed in this work are provided in Table 3-1. Extensive analysis was performed on each of these samples. Elemental analyses are presented in Table 3-2 and relative mole ratios, relative to carbon, are presented in Table 3-3 for N, S, H and O. Maximum uncertainties of the atom ratio, Table 3-3, were calculated based on the measurement uncertainties of N, C, H, S and O. If the uncertainty is smaller than 0.01, a value of zero is reported. From these data it is clear that Si is removed selectively from samples 2 and 3 relative to sample 1, and that both samples 4 and 5 are enriched in Si relative to sample 1. Sample 2 is enriched in P, Ni, Fe, and Na relative to sample 1 and samples 3-5. Sample 2 is also enriched in H, S and to a lesser extent oxygen relative to sample 1 and samples 3-5. From an organic material perspective, samples 1 and 3-5 are effectively the same within the uncertainty of these measurements. The inorganic material content and relative composition is quite variable. For example, samples 2 and 3 are reduced in C and Si relative to sample 1, while samples 3 and 4 are reduced in sulfur only. Mass balances on dominant elements are respected as are mass balances on trace inorganic elements, although both P and Ni contents in Samples 4 and 5 are too low relative to Sample 1.

Table 3-1 A brief description of the 5 samples analyzed in this work

Preparation	Sample name	Sample description
“Froth treatment” and Distillation treatment	Sample 1	Processed water sample
Chemical Deposition of Sample 1	Sample 2	LC-rich sample with little interference from bitumen
	Sample 3	LC-rich sample mixed with bitumen
Coffee Ring Effect of Sample 1	Sample 4	Edge area sample
	Sample 5	Central area sample
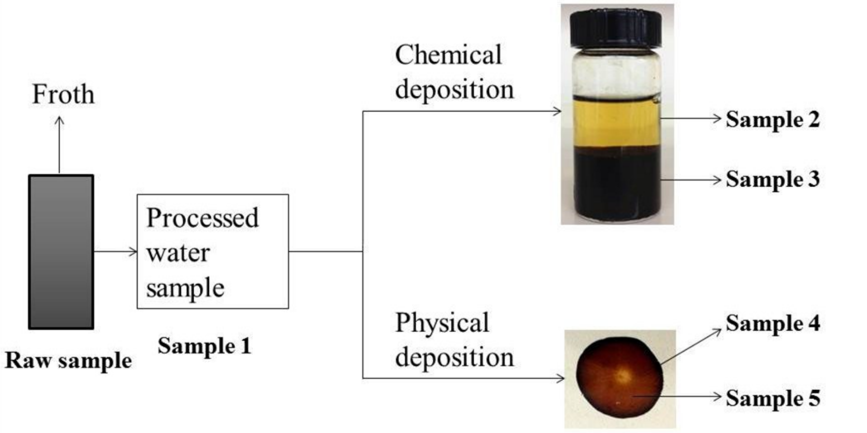		

Table 3-2 Weight percentage of the main elements in the 5 samples

Type	Element	Sample 1	Sample 2	Sample 3	Sample 4	Sample 5
Organic (Wt. %)	N	0.38	0.13	0.42	0.55	0.26
	C	22.53	5.08	21.64	34.13	20.03
	H	2.31	0.88	1.93	3.50	2.17
	S	1.18	0.79	1.23	1.56	1.17
	O	18.7	5.57	10.58	26.33	20.64
Inorganic (Wt. %)	C	1.70	<DL	<DL	2.20	1.75
	S	0.27	0.36	0.29	0.03	0.04
	Si	1.10	0.08	0.05	2.74	3.35
Metal (ppm)	Na	189×10^3	312×10^3	200×10^3	148×10^3	252×10^3
	B	724×10	488×10	557×10	155×10^2	111×10^2

	K	550 × 10	675 × 10	595 × 10	391 × 10	829 × 10
	Fe	596 × 10	109×10^2	166 × 10	170 × 10	623
	Ca	893	834	822	321 × 10	114 × 10
	P	892	2456	452	344	260
	Ni	329	736	51.0	5.00	2.00
	Al	250	293	219	503	333
	Li	224	259	237	187	180
	Mg	198	229	169	926	216
	V	2.55	2.10	2.01	2.60	3.71

Table 3-3 Atom ratios of Nitrogen, Hydrogen, Sulfur and Oxygen to Carbon (± maximum uncertainties)

Element	Sample 1	Sample 2	Sample 3	Sample 4	Sample 5
C	1	1	1	1	1
H	1.22 ± 0.07	2.09 ± 0.37	1.06 ± 0.07	1.22 ± 0.05	1.29 ± 0.08
S	0.02 ± 0.01	0.06 ± 0.03	0.02 ± 0.01	0.02 ± 0.00	0.02 ± 0.01
N	0.01 ± 0.00	0.02 ± 0.02	0.02 ± 0.01	0.01 ± 0.00	0.01 ± 0.01
O	0.62 ± 0.02	0.83 ± 0.08	0.37 ± 0.01	0.58 ± 0.01	0.77 ± 0.02

3.4.2 FTIR Analysis

The FTIR spectra in Figure 3-13 show the absorbance peaks for Sample 2-1 (after drying) and Sample 2-2 (without drying). The absorbance peaks for these two samples are the same but the heights of the peaks differ. Exposure to moisture during or following processing does not affect the functional groups identified from FTIR analyses. Sample 1 is compared with samples 2 and 3 in Figure 3.14, and sample 1 is compared with samples 4 and 5 in Figure 3-15. Typical functional group assignments [60] are shown in Figure 3-14. There are clearly both qualitative and quantitative differences between sample 1 and samples 2 and 3. Samples 1, 4 and 5 are qualitatively and quantitatively similar as shown in Figure 3-15. This means that the functional groups in the central area sample (Sample 5) and the edge area sample (Sample 4) are similar to Sample 1. Clearly the coffee ring effect does not partition Sample 1 on the basis of these functional groups. This outcome is consistent with the CHNOS elemental analysis above. Samples 1, 4, and 5 are comparable and Samples 2 and 3 differ from one another and from Sample 1.

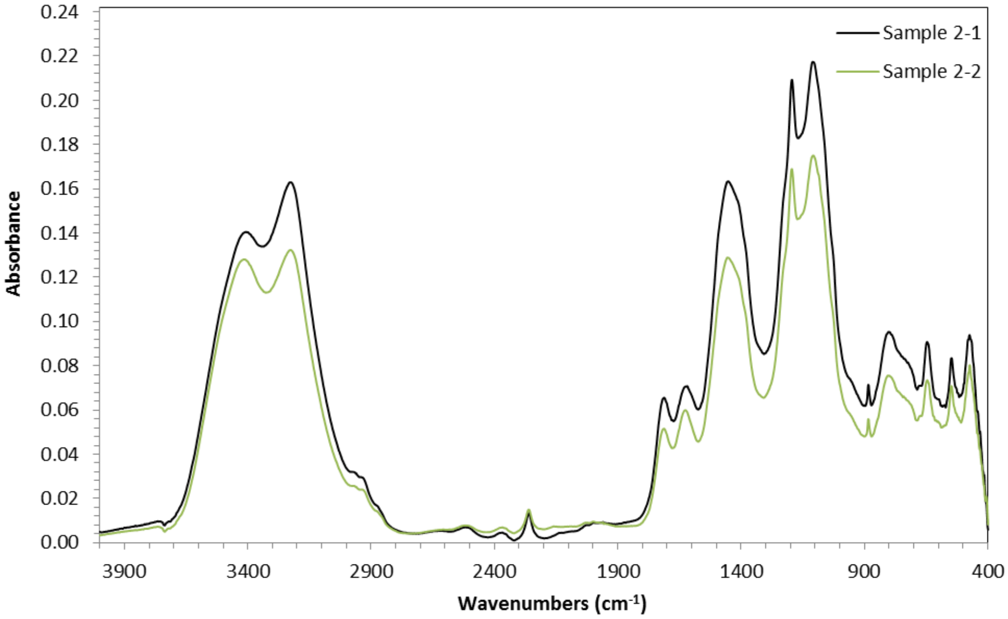

Figure 3-13 FTIR spectrum of Sample 2-1 (after drying) and Sample 2-2 (without drying)

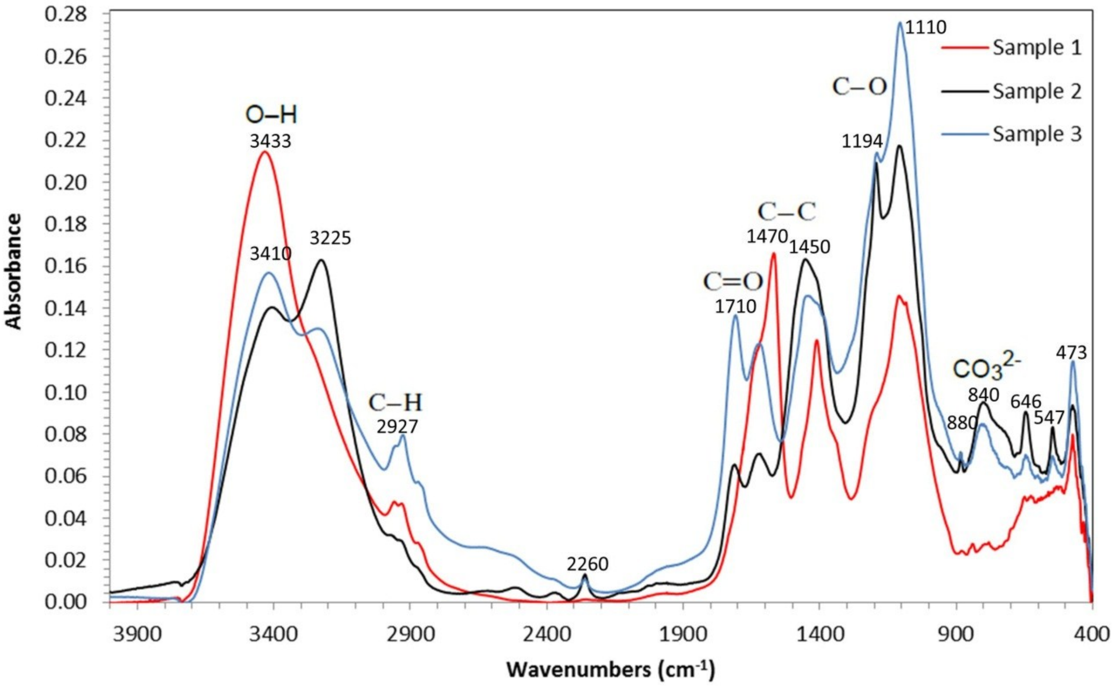

Figure 3-14 FTIR results of Sample 1, Sample 2 and Sample 3

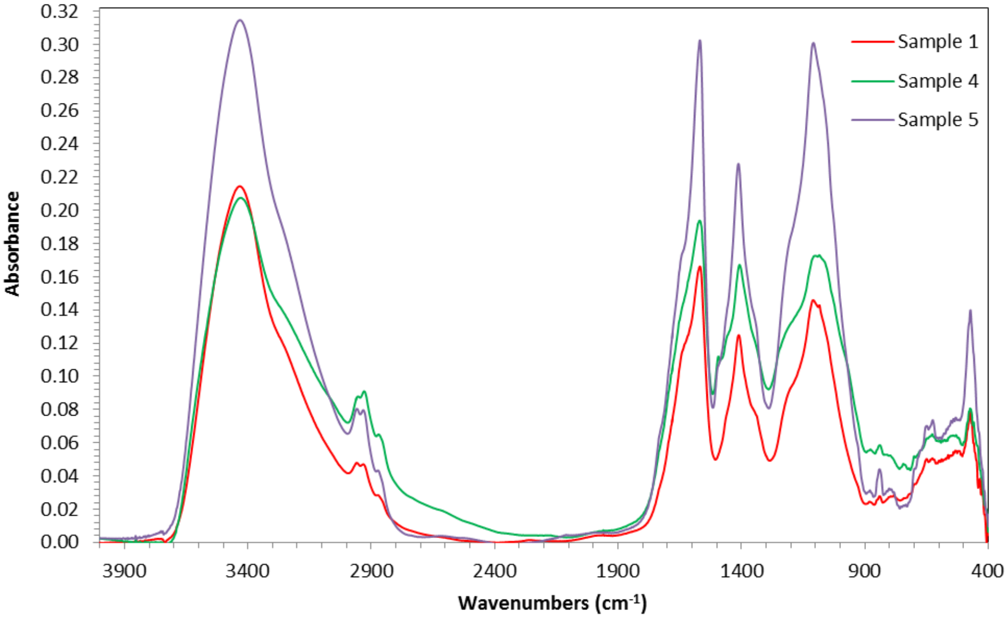

Figure 3-15 FTIR results of Sample 1, Sample 4 and Sample 5

3.4.3 Negative-ion ESI/FT-ICR MS Analysis

This analysis is severely impacted by salts. In a preliminary set of measurements, the samples were not desalinated, and the impact of sodium chloride salt is evident as shown in Figures 3-16 and 3-17. With reference to Figure 3-16, Samples 1 through 5 show intensive peak clusters at m/z ~ 293 and ~ 451. The peaks in Sample 2 and Sample 3 (marked by the red cycles) are consistent with adducts and isotopes of sodium chloride. The high intensity peaks shown in Figure 3-17 (a) indicate sodium chloride adducts, and adjacent peaks differ by one NaCl unit. Peaks in Figure 3-17 (b) show compounds composed of NaCl adducts and isotopes (i.e. ^{35}Cl and ^{37}Cl). The mass spectra of the organic material in these samples cannot be detected accurately due to the influence of salt, and desalination treatment was performed on all of the samples. Inorganic compounds (i.e. salt) were removed by water and dissolved organic matter (DOM) was concentrated in methanol using C18 solid phase extraction (SPE, 1g, 6cc, Waters, USA) method [61]. Here are some core steps: Samples 1-5 were dissolved in acid water (HCl solution, pH=2). The polar acid hydrophilic organic material in the water is called dissolved organic matter (DOM). DOM was introduced into C18 solid phase column and absorbed by C18 column. Then the salt was removed by the acidified water. The remaining material in the column is called hydrophobic acids (HOA). HOA is extracted using methanol and is then sent to FT-ICR MS for analysis. It is worth noting that organic materials with strong polarity may be removed (like these with more than 10 oxygen atoms) during this process. The HOA which is extracted by the C18 solid phase extraction method is defined as humic-like substances (HULIS) in this work because the extraction method is similar with Earl M. Thurman's work on humic substance in 1981[62]. Two things are different in the two methods: (i) the sources are different: in Thurman's work the natural organic matter (NOM) is natural water. In this work, the NOM is from SAGD processed water; (ii) In Thurman's work, the extraction column is XAD-8 resin. In this work, a C18 column was used. HULIS is a broad category that it cannot be used to determine candidate species that form liquid crystal domains. In next part of this work, humic substances are discussed in more detail.

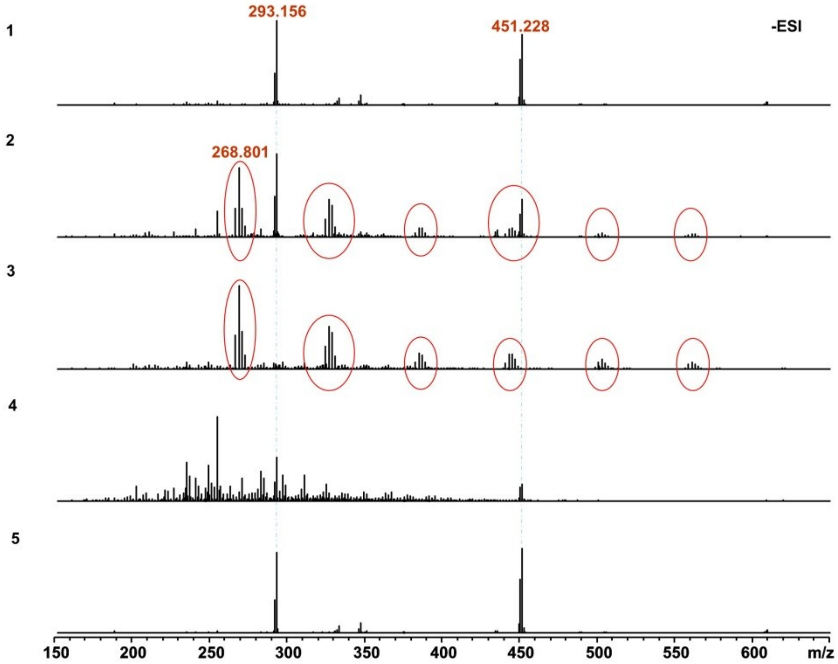

Figure 3-16 Negative-ion ESI/FT-ICR mass spectra of the 5 samples before desalination treatment. Peaks circled in red are known to include sodium chloride.

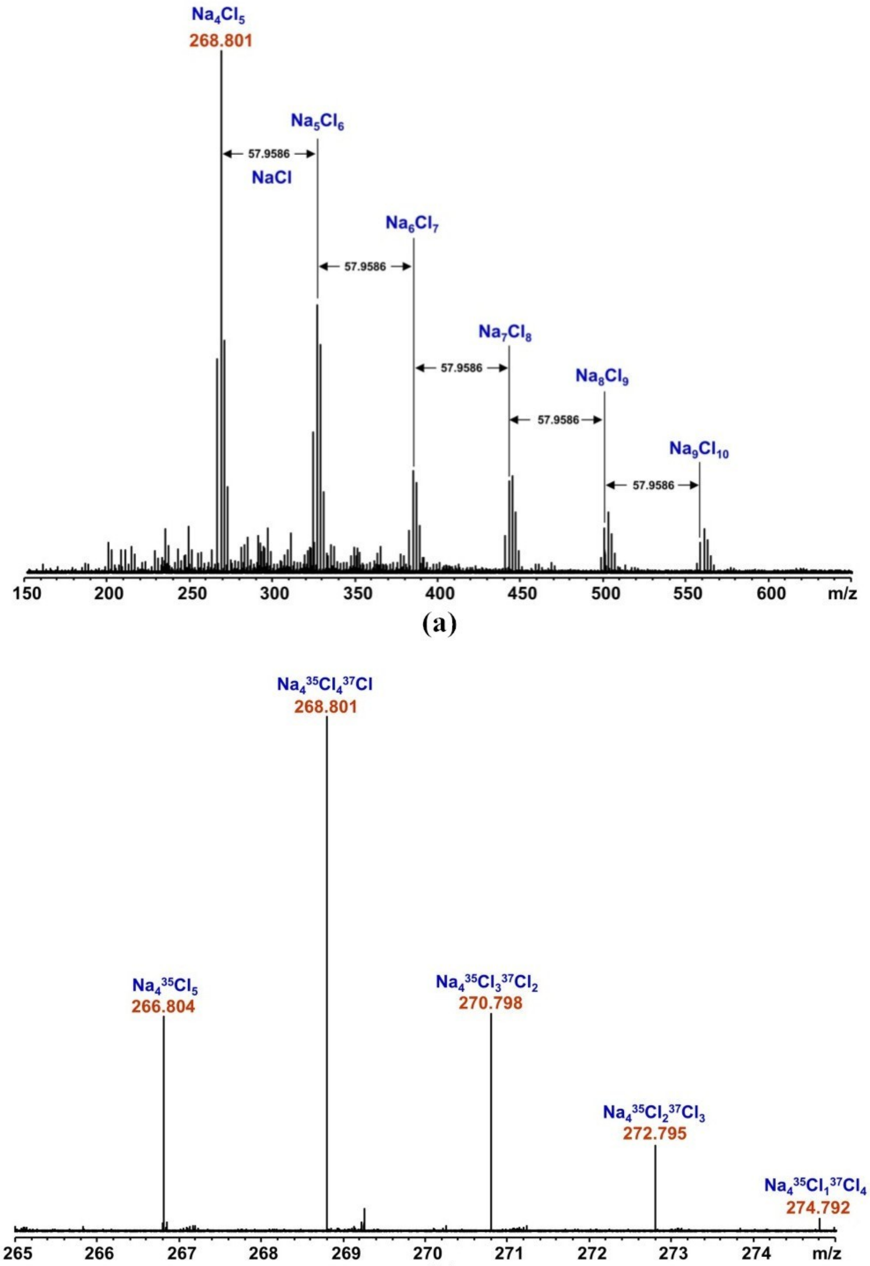

Figure 3-17 (a) Peak clusters in negative-ion ESI/FT-ICR mass spectra of Sample 3 before desalination; (b) Na_4Cl_5 and its isotopes in Sample 3 before desalination.

After desalination, samples were re-analyzed using negative-ion ESI/FT-ICR MS. The abundant molecular weights vary from m/z 150 to 600 as shown in Figure 3-18. The influence of salt in the samples was eliminated and the molecular constituents of all five samples are observed clearly in expanded mass scale spectrum at m/z 313 shown in Figure 3-19. Significant differences in the overall and the local mass distributions are evident. These differences were explored in greater detail and the results are reported in Figures 3-20 to 3-24 which show the type (DBE) and class (number of heteroatoms) analyses of the samples. "Relative abundance is defined as the magnitude of each peak divided by the sum of the magnitudes of all identified peaks in the mass spectrum [55]". The data shown in Figure 3-20 to Figure 3-24 are presented on this basis.

Figure 3-21 and Figure 3-22 show that the main species classes in Sample 2 and Sample 3 are O_2-O_{10}, N_1O_3-N_1O_8 and O_3S_1-O_8S_1. Some loss of O_{10+} material is expected and this may suppress the response of these classes of compounds. In Sample 2, the O_6 class species, especially those with 3-12 DBE, are most abundant, followed by the O_5 class species. The relative abundances of sulfur class species has the order of $O_4S_1 \approx O_6S_1 > O_5S_1 > O_3S_1 > O_7S_1 \approx O_8S_1$. In Sample 3 the O_4 class species were most abundant, especially these with 2-12 DBE, the O_4 was the second most relative abundant. These distributions differ significantly from Sample 1, shown in Figure 3-20. By contrast, the main classes and relative abundances, by DBE within classes for Sample 1, Figure 3-20, and Sample 5, Figure 3-24, are closely related. The main class species in Sample 1 and Sample 5 are O_2-O_{10}, N_1O_3-N_1O_8 and O_3S_1-O_9S_1. The O_4 class has the most abundance. For sulfur class species the two class species with largest abundances are O_3S_1 and O_4S_1. Figure 3-23 indicates that the main class species in Sample 4 are O_2-O_6, O_2S_1-O_4S_1 and N_1O_2-N_1O_4. The O_2 class species are dominant among all heteroatom classes especially those with 2-11 DBE. According to the heteroatom class species identified, all the samples include acidic material containing oxygen. O_4, O_5, O_6 and O_7 are four most abundant heteroatom classes in the five samples. Other categories of material are also present in these samples.

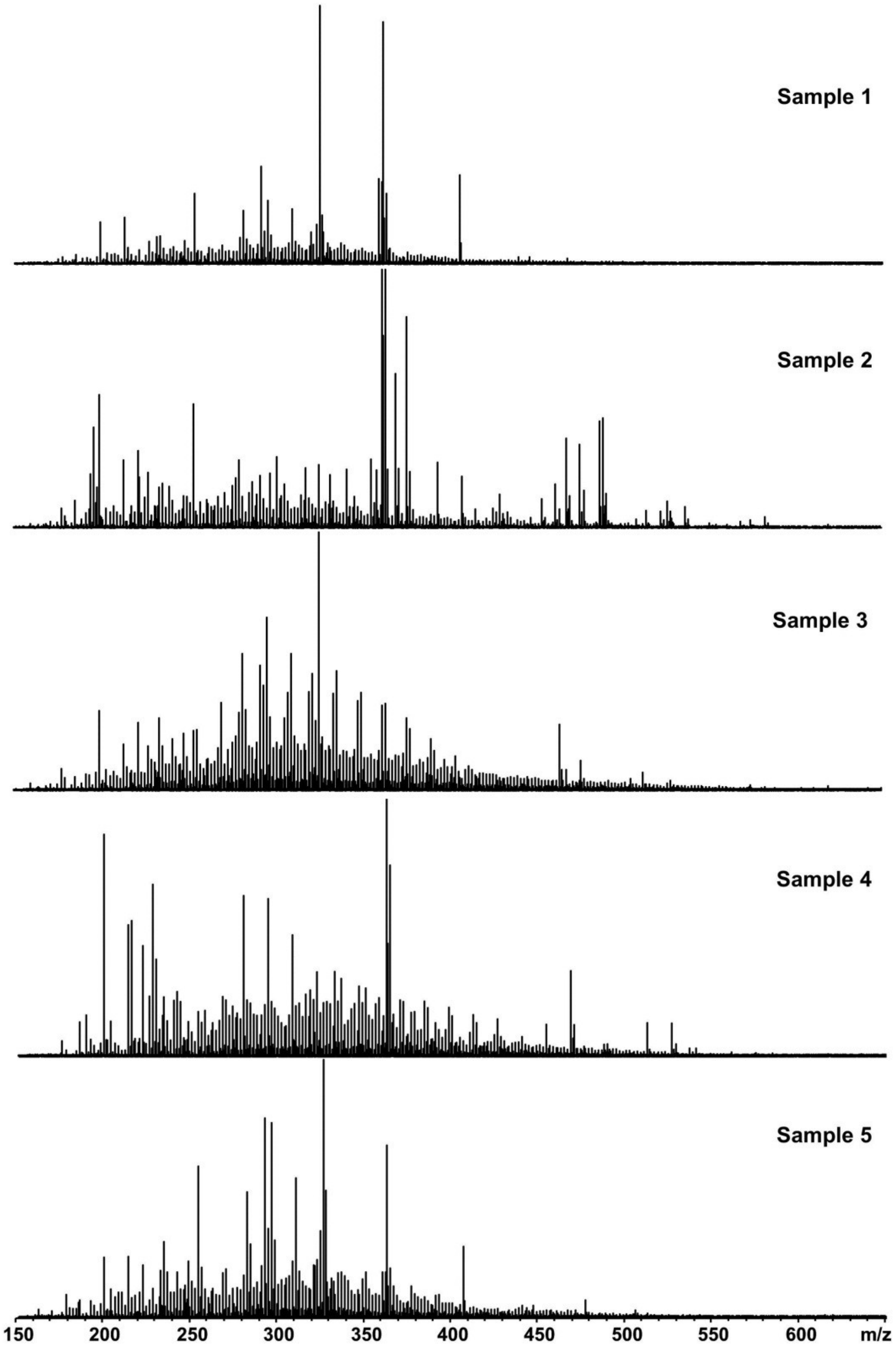

Figure 3-18 Negative-ion ESI FT-ICR mass spectra of the 5 samples after desalination.

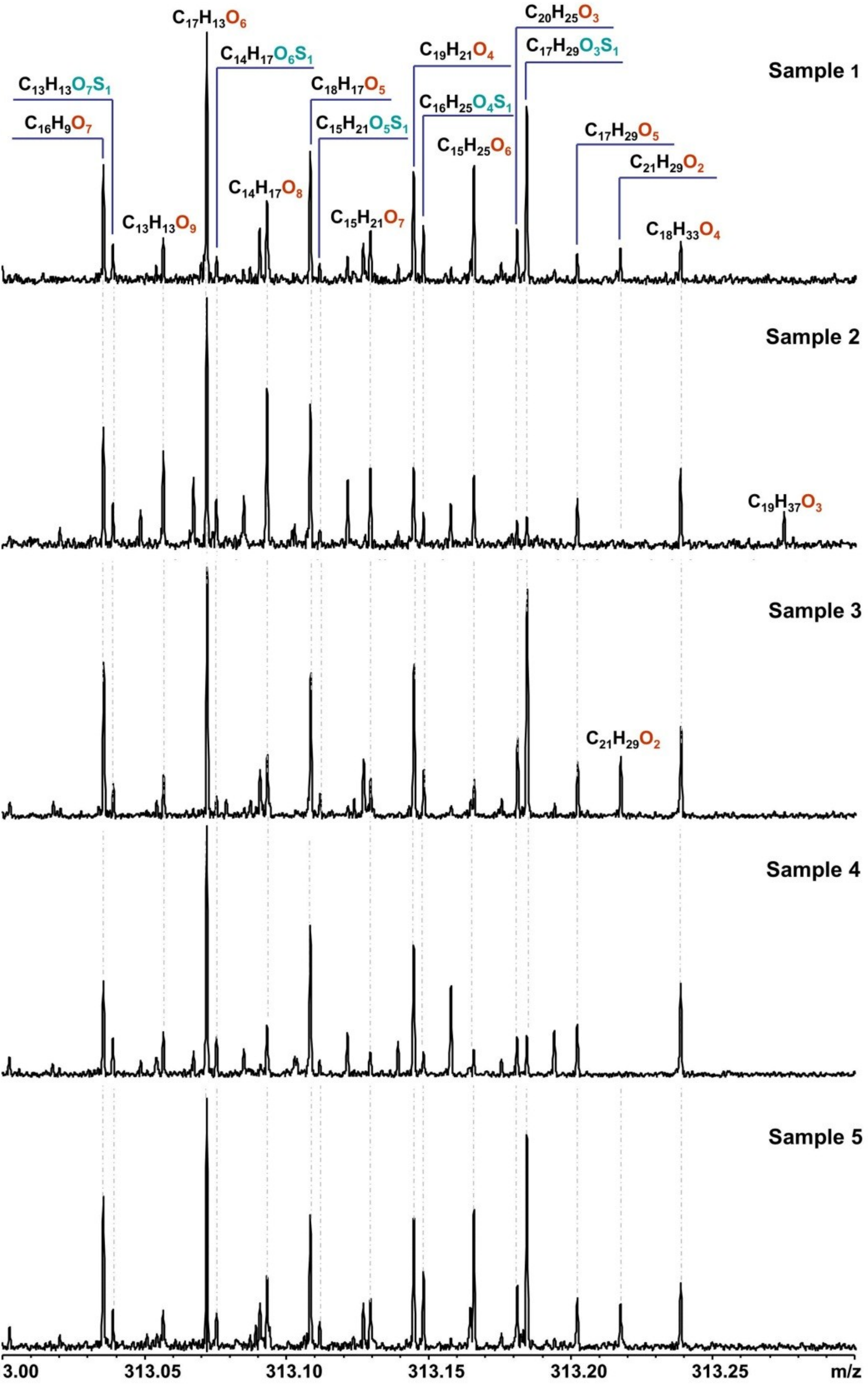

Figure 3-19 Expanded mass scale at m/z 313 for the 5 samples

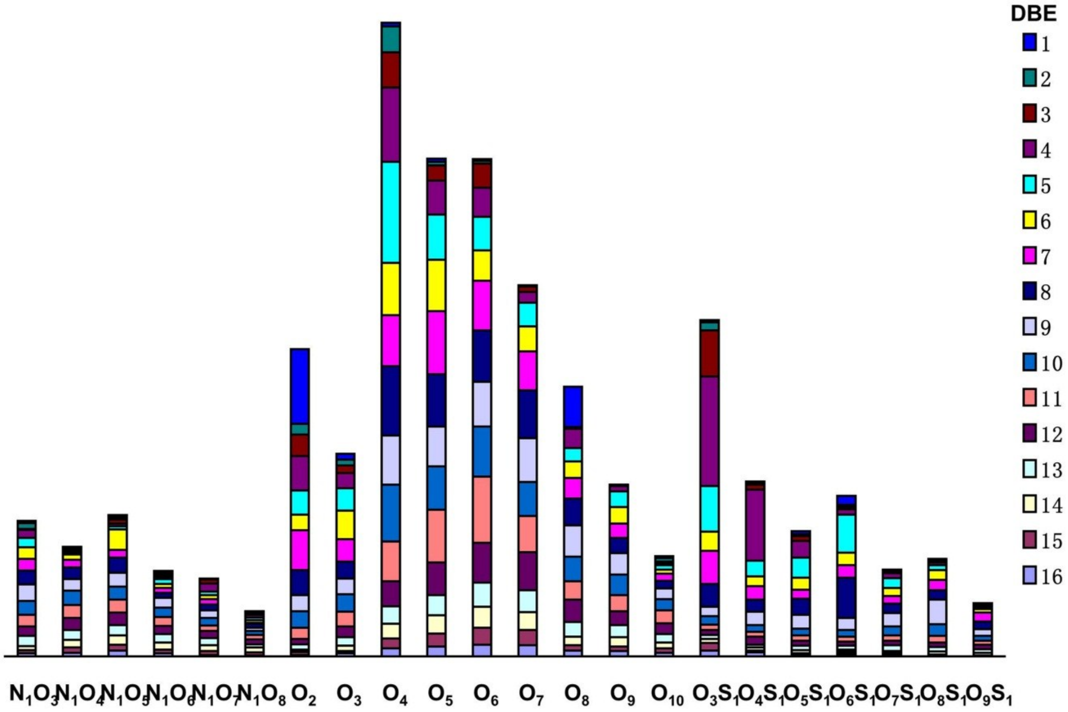

Figure 3-20 Heteroatom class (number of heteroatoms) and type (double bond equivalent) distribution for Sample 1 derived from a negative-ion ESI/FT-ICR MS spectrum

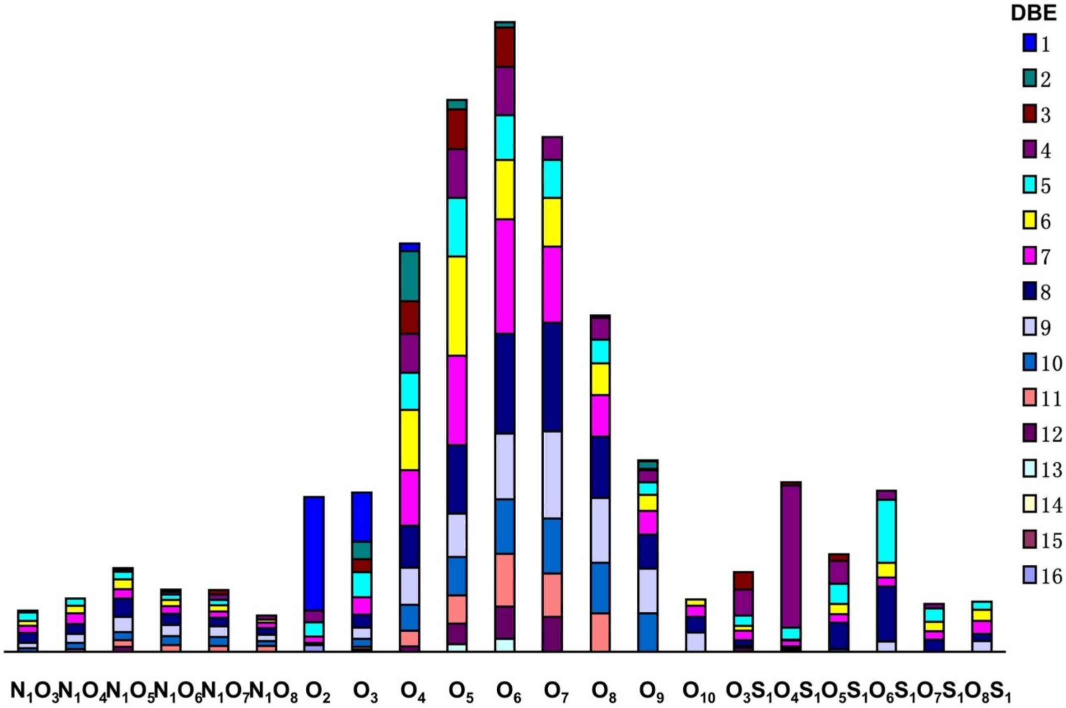

Figure 3-21 Heteroatom class (number of heteroatoms) and type (double bond equivalent) distribution for Sample 2 derived from a negative-ion ESI/FT-ICR MS spectrum

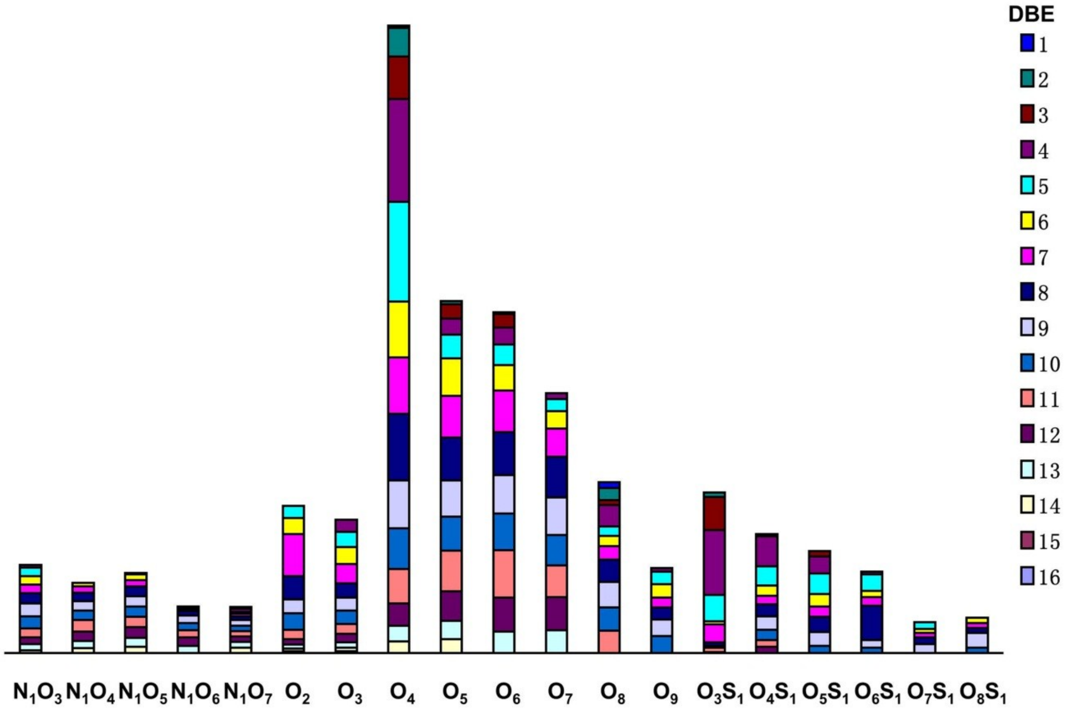

Figure 3-22 Heteroatom class (number of heteroatoms) and type (double bond equivalent) distribution for Sample 3 derived from a negative-ion ESI/FT-ICR MS spectrum

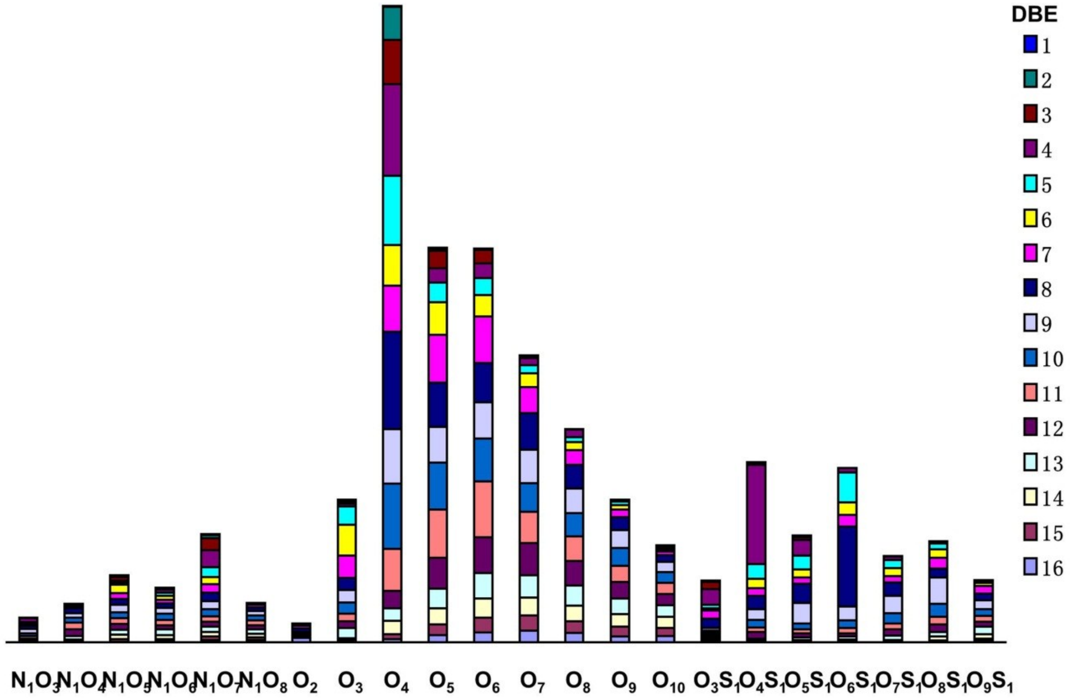

Figure 3-23 Heteroatom class (number of heteroatoms) and type (double bond equivalent) distribution for Sample 4 derived from a negative-ion ESI/FT-ICR MS spectrum

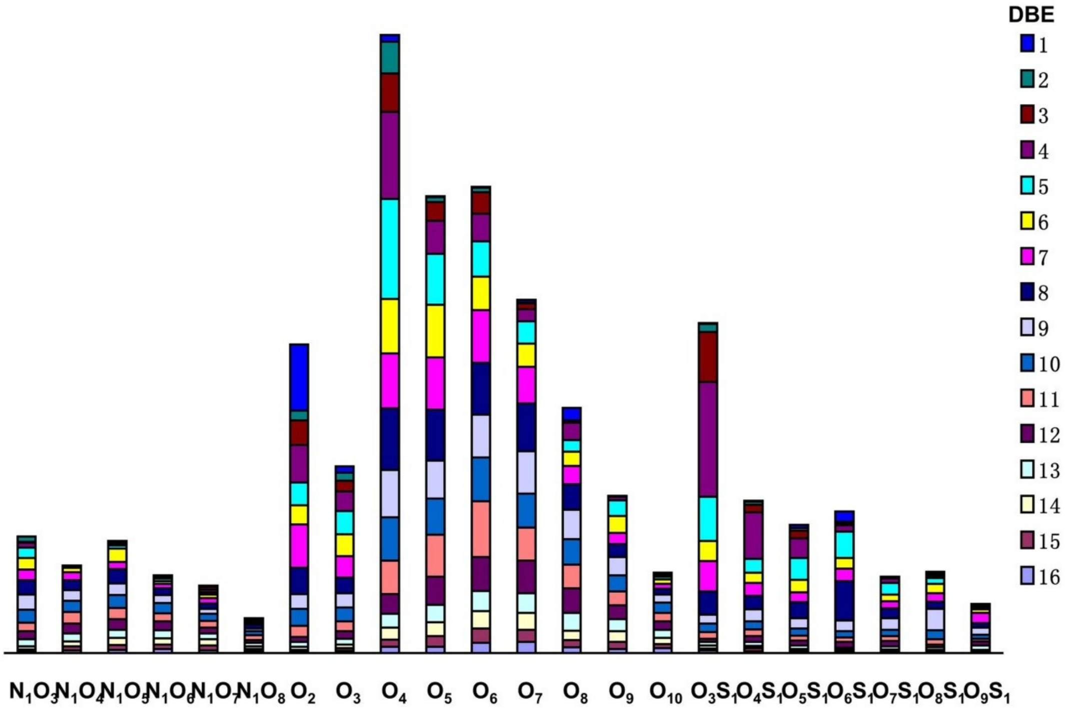

Figure 3-24 Heteroatom class (number of heteroatoms) and type (double bond equivalent) distribution for Sample 5 derived from a negative-ion ESI/FT-ICR MS spectrum

Heteroatom class (number of heteroatoms) and type (double bond equivalent) distributions, Figures 3-20 to 3-24, show the main classes identified and their abundances. However, molar mass distributions by class are not evident. As this is another way to discriminate samples, the mass ranges of species are presented in plots of DBE as a function of carbon number. Six common classes for each sample were chosen O_4, O_5, O_6, O_7, N_1O_4 and S_1O_3. Their isoabundance maps are presented in Figure 3-25. As is evident from these plots samples 1 and 5 cannot be discriminated on the basis of these data either. Detailed comparisons based on class follow:

O_x Class Species. The O_4 class was the most abundant class in all of the samples except Sample 2. For this class, as for the O_5 class the distributions for Samples 1 and 5 are essentially the same, while those for Samples 2-4 differ from sample 1 and one another both qualitatively and quantitatively. For the O_6 class, Samples 1, 3 and 5 are qualitatively similar, and Samples 2 and 4 are qualitatively similar. For the O_7 class, all five samples share common features and are qualitatively similar. In the maps of O_4 class species for Sample 1 and Sample 2. The biggest spot in the map was used as the benchmark so that other spot were small. For Sample 1, Sample 4 and Sample 5, the most two abundant O_4 class species had 6-12 DBE, 11-20 carbon number and 3-5 DBE, 16-24 carbon number. For Sample 3, the most abundant O_4 species had 3-5 DBE and 16-24 carbon number. From the range of DBE values and numbers of carbons/molecule, it is clear that the molecules comprise a broad mix of molecular structures from aromatic to naphthenic compounds and some include alkane functionalities. For O_5, O_6 and O_7 class species, the maps were similar. Totally, the most abundant O_{5-7} species had 6-12 DBE and 11-20 carbon number. The O_x class species varies over a wide range of DBE (1-16) and carbon number (5-30). But for Sample 2, the O_x species varies in a range of DBE (1-12) and carbon number (5-25). The carbon numbers shown in the x axis of Figure 3-25 for Sample 2 represented the liquid crystal rich material with little interference of bitumen is lighter than other samples. The relatively highly abundant O_x species (include O_4, O_5, O_6 and O_7 species) were at 5-9 DBE and 10-16 carbon numbers for Sample 2.

Nitrogen-Containing Species. From Figures 3-20 to 3-24, all five samples are relatively abundant in N_1O_x class species. The N_1O_4 class is shown in Figure 3-25. For Samples 1, 3, 4 and 5, the N_1O_4 class is most abundant in the 9-12 DBE and 16-20 carbon number range. By contrast, the N_1O_4 class in Sample 2 is most abundant at lower DBE. The N_1O_4 class species in Sample 2 have different molecular structures on average than those in the other samples.

Sulfur-Containing Species. Figures 3-20 to 3-24 show that the five samples are relatively abundant in S_1O_x class species. The S_1O_3 class is shown in Figure 3-25. This class with a DBE centred at 4 and possessing a carbon number range from 15-18 is common to all five samples and cannot be used to discriminate them.

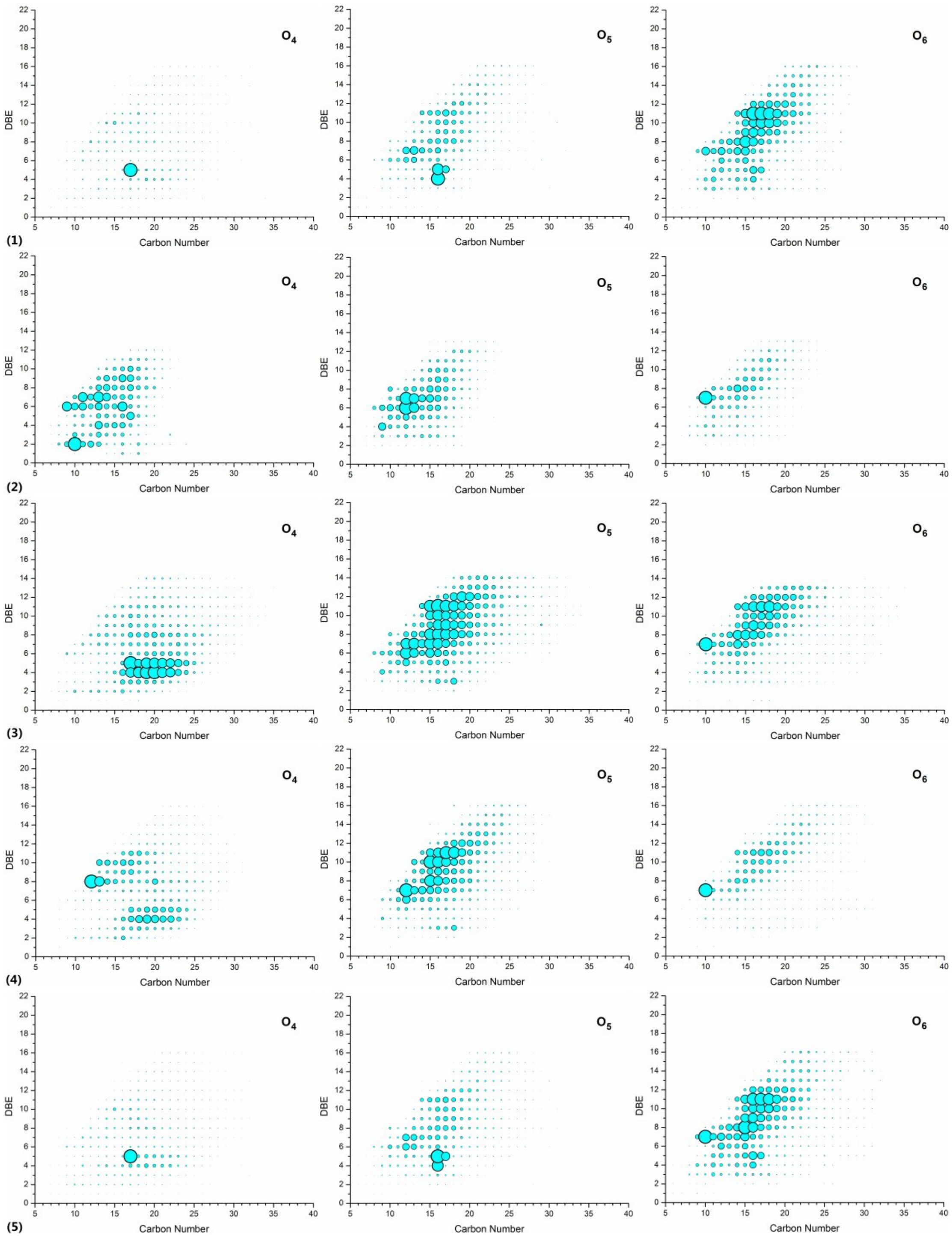
O4
O5
O6
DBE
Carbon Number
0 2 4 6 8 10 12 14 16 18 20 22
5 10 15 20 25 30 35 40
(1)
(2)
(3)
(4)
(5)

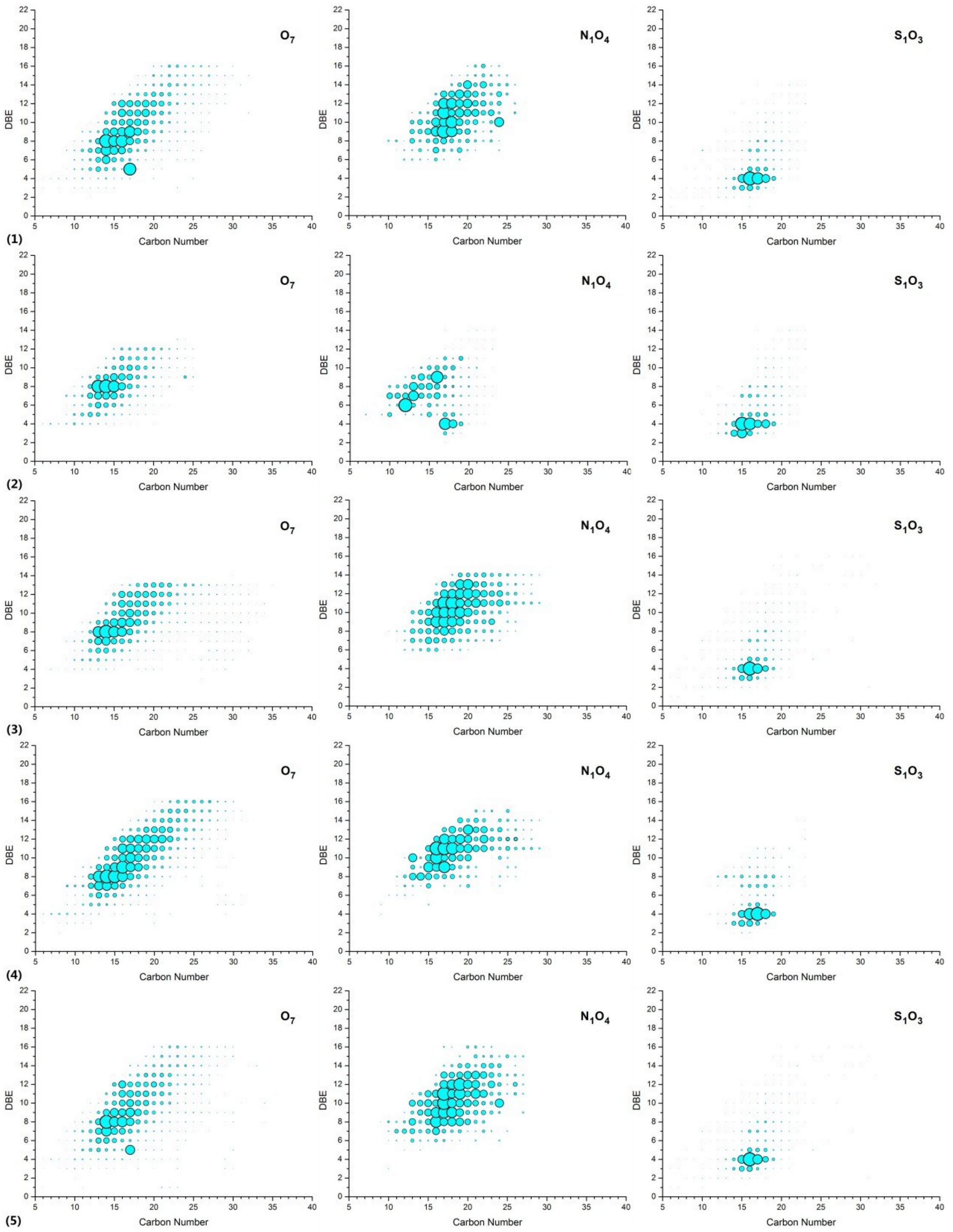

Figure 3-25 DBE vs carbon number abundance plots obtained using negative-ion ESI/FT-ICR MS for O_4, O_5, O_6, O_7, N_1O_4 and S_1O_3 species in samples 1 to 5

3.5 Summary.

The elemental analyses provide a measure of the composition of the 5 samples. The organic material present is significantly enriched in O relative to bitumen and Sample 2, the liquid crystal enriched sample with the best partitioning from contaminants, has the lowest weight percentage of HC class compounds. H, S and especially O are enriched in it. FTIR results provide information on functional groups present and their distribution differences among the samples. FT-ICR MS is also the core analysis. Possible molecular structures and the abundance of different heteroatom classes can be identified through the FT-ICR MS results. These results underscore the similarity of Samples 1, 4 and 5 and show that the coffee ring effect does not provide a mechanism for the selective separation of liquid crystal rich domains from other materials present. Sample 2 would appear to be most representative of the liquid crystal rich material. However, only a fraction of the liquid crystals are recovered in this sample. From the elemental analysis, it would appear that more than half of these domains remain in Sample 3 and care in the interpretation of the results is justified. The key analysis outcomes are summarized in Table 3-4.

Table 3-4 Summary of chemical analyses of Samples 1-5

Sample		1	2	3	4	5
Elemental analysis	Organic	Sample 1 and Sample 3-5 are similar; Organic compound in Sample 2 is less than 20 wt %; Sample 2 is enriched in H, S and to a lesser extent oxygen relative to Sample 1 and Samples 3-5.				
	Inorganic	Sample 2 is enriched in P, Ni, Fe, and Na relative to sample 1 and samples 3-5.				
FTIR	Function Group	-OH, -C=O, -COOH exist in Sample 1, 2 and 3; Sample 4 and 5 are not separated from Sample 1				
FTICR-MS	O_x	For O_5, O_6 and O_7 class species, the maps were similar. The most abundant O_{5-7} species had 6-12 DBE and 11-20 carbon number. For sample 2, the relatively highly abundant O_x species (include O_4, O_5, O_6 and O_7 species) were at 5-9 DBE and 10-16 carbon numbers.				
	NO_x	NO_x class in Sample 2 is most abundant at lower DBE than that of other samples.				
	SO_x	Samples 1 through 5 are similar.				

Chapter 4 General discussion

4.1 Overview

In this chapter, outcomes form physical observations and the different analytical techniques, summarized in Table 2-1 and Table 3-4 are discussed jointly. Possible issues that may affect the interpretation of the experimental analyses are discussed and possible compositions of liquid crystals are explored.

4.2 Combining Results from Observation and Elemental, ESI/FT-ICR MS and FTIR Analysis

As described in Chapter 2, Sample 1 is already enriched in liquid crystal rich material relative to bitumen but organic and inorganic materials remain present. Further isolation of liquid crystal rich material from Sample 1 was attempted using both chemical separation (Samples 2 and 3) and physical deposition (samples 4 and 5). Based on all of the measurements and observations there are no obvious composition differences between Samples 1 and 5. Organic materials are most enriched in Sample 4 but liquid crystal domains are mixed together with bitumen and inorganic materials. From their appearance, Samples 4 and Sample 3 are the darkest, and Sample 2 is the lightest. The presence of bitumen (black in colour) and organic material are detected preliminarily by color. Samples that are light in color have limited bitumen content. This observation (Chapter 2.6) is consistent with the elemental analysis (Table 3-2). Separation using the coffee ring effect, proved unsuccessful. Samples 1 and 5 are the same and Sample 4 includes diverse materials. Sample 4 provides some information by contrast with bitumen and bitumen mixed with liquid crystal domains but it does not provide information about liquid crystal rich material. The heteroatom class species in Athabasca bitumen and its distilled heavy vacuum gas oil fraction (HVGO) as well as acid-only and acid-free fractions isolated using an ion-exchange resin (acid-IER) and FT-ICR MS [63] are shown in Figure 4-2. For bitumen analyzed using the same FT-ICR MS technique, the dominant species classes are N_1, O_2, N_1S_1 and S_1O_2. Many of these do not have significant abundances in Samples 1-5. The abundant molar mass range for Samples 1-5 (m/z 200-500) (Figure 3-18) is lower than for Athabasca bitumen (m/z 400-700) (Figure 4-1). Thus the molar mass of liquid crystal rich materials is low relative to Bitumen.

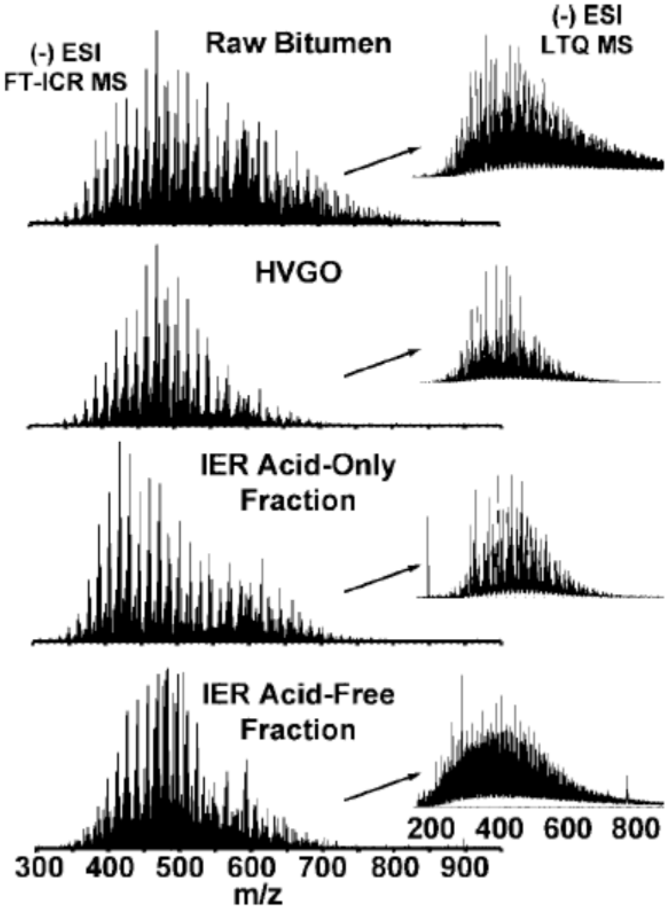

Figure 4-1 Broadband negative-ion ESI FT-ICR mass spectra of Athabasca bitumen, distillation-isolated HVGO, IER-isolated HVGO acid fraction, and IER-isolated HVGO acid-free fraction. Insets on the right show low-resolution linear ion-trap mass spectra that validate the molecular-weight distributions observed by FT-ICR MS [63]

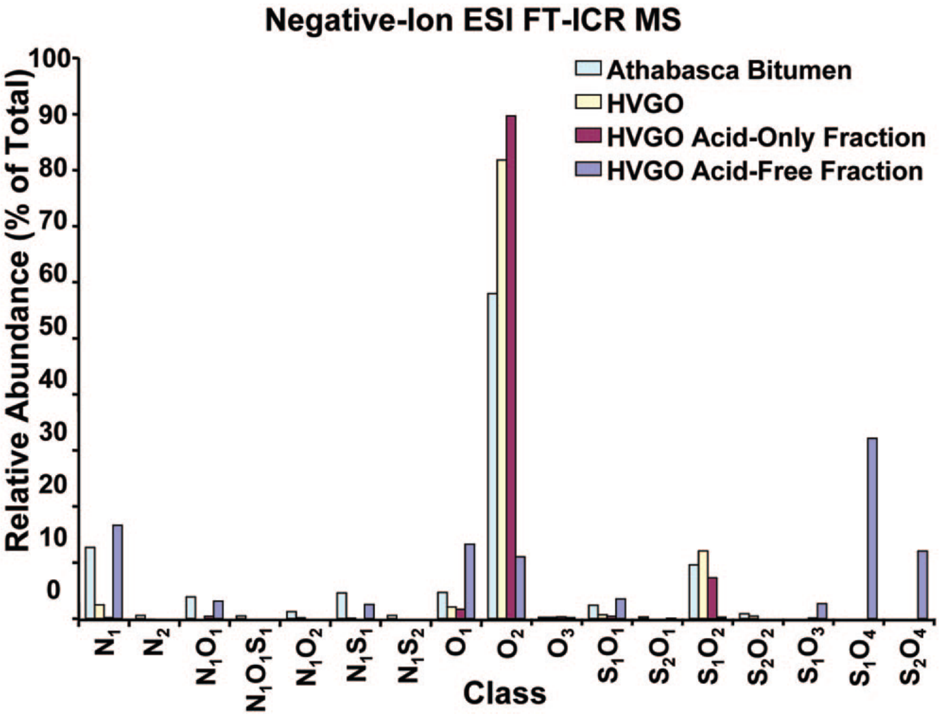

Figure 4-2 Heteroatom class analysis for Athabasca bitumen, HVGO, IER-isolated HVGO acid fraction, and IER-isolated HVGO acid-free fraction, derived from the high-resolution ESI FT-ICR mass spectra of Figure 4-1 [63]

During chemical separation of Sample 1 into Samples 2 and 3, a large fraction of the organic material remained in the lower layer (Sample 3) that included bitumen and liquid crystal domains. Hence Sample 2 includes only a fraction of the liquid crystal rich material and may not be fully representative of the liquid crystals as a whole. Further in spectroscopy, the relative sensitivities of the method to a specific molecular species is dependent on the chemical nature of constituents and mass fractions of all constituents present [64, 65]. So, analysis of a sample as a whole, or as a series of sub-fractions prepared on the basis of a specific property, such as polarity or boiling point range, can yield significantly different impressions as to the principal constituents of a sample from a mass or mole fraction perspective. However, as the negative-ion ESI/FT-ICR MS technique focuses on polar species, and suppresses HC class materials in the analysis, this latter effect may not be a determining factor for this study. In addition, all of the samples are enriched in liquid crystal materials relative to bitumen and thus share a range of properties and constituents. The one residual concern is that the O_{10+} class species may be artificially suppressed due to the need to eliminate salt prior to the analysis.

As Samples 2 and 3 both include liquid crystal rich materials, and present the most extreme elemental composition differences (Table 3-2), even though they have common functionalities (-C=O, C-O and –OH) (Figure 3-14), they provide perspectives on key features of the liquid crystal rich material. Combined with the abundance of O_x class species, it is clear that the liquid crystal rich materials include carboxylic acids (-COOH), oxyacids and other oxygen rich species. Given the low Si content of these two samples, its presence has little possible influence on FTIR analysis. It is also worth noting that nickel (>700ppm) is relatively more abundant in Sample 2 compared to Sample 1 (329ppm) and Sample 3 (51ppm).

The elemental analysis indicates an atom ratio for O/C of 0.83 ± 0.08 for Sample 2. This value is high relative to the ESI/FT-ICR MS abundance data where O/C ratios range from 0.25:1 to 0.7:1, even for the O_7 class. The ranges for the other O_x classes are lower. This outcome underscores the need for caution with respect to data interpretation. All of the samples were desalted using C18 solid phase extraction. Some hydro-soluble oxygen-containing substances were certainly washed off. Species soluble in water tend to be polar and in the present context, organic acids are likely candidates. High solubility species tend to be oxygenates. It would appear that species with high oxygen to carbon ratios were eliminated during desalting [61].

The heteroatom class species in sample 2 are different from the emulsions extracted from the interface between bitumen and water as shown in Figure 4-3 [66]. The heteroatom class species in liquid crystal rich materials contain more oxygen. For instance, the O_x Class species in Sample 2 are $O_{2\text{-}9}$, the N_xO_y class species in sample 2 are $NO_{3\text{-}8}$. The most abundant species in the 5 samples are O_4, O_5, O_6 and O_7. In the emulsions, the most abundant classes of species are O_2, O_3, O_4, SO_2, SO_3 and SO_4. Whether this is an artefact of their sample preparation process, or differences in SAGD vs mining operations for Athabasca bitumen is unclear.

Brady Masik [23] obtained liquid crystal rich materials from Athabasca bitumen C5 asphaltenes by solvent extraction. He found that the liquid crystal enriched sample possesses a narrower and lower molecular mass range and higher relative abundances of sulfur, oxygen and nitrogen than the parent asphaltenes. In his work the FT-ICR MS analysis was performed using positive-ion atmospheric pressure photoionization (APPI) 9.4 T FT-ICR MS. This technique highlights other chemical features of the sample. In addition, insufficient sample was available for elemental analysis. Thus direct comparisons with the present work are difficult. Even so, the mass range of the liquid crystal-enriched C5-asphaltene fraction and liquid crystal rich materials obtained in this work are comparable (m/z 150-500) according to Figure 3-18 and Figure 4-2. The most abundant heteroatom class species identified by Masik were S_1, HC, N_1, O_1, S_1O_1, O_2, etc. as shown in Figure 1-3. These differ from those identified for Athabasca bitumen obtained using the ESI sample preparation technique where the most abundant class species are O_2, N_1, S_1O_2, O_1, N_1O_1, S_1N_1 and S_1O_1 as shown in Figure 4-2. The hydrocarbon class (HC) is not presented in Figure 4-2, because ESI does not ionize nonpolar compounds. Even if they are present in a sample, no information is obtained [53]. The analyses in this work also used ESI preparation, but given the elemental analysis the liquid crystal rich materials are unlikely to comprise molecules made up only of carbon and hydrogen.

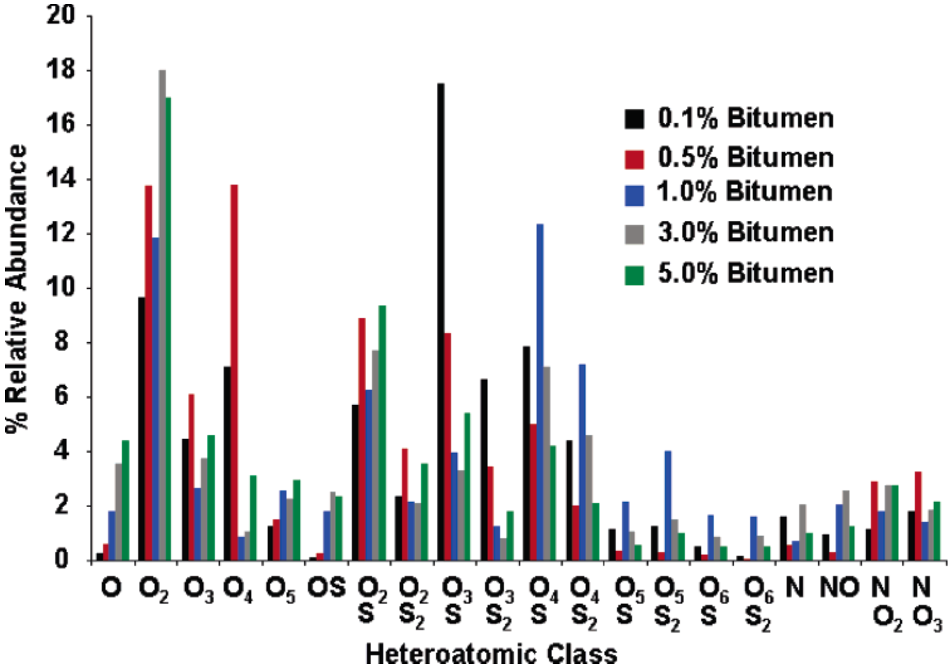

Figure 4-3 Negative-ion ESI acidic NSO class relative abundances (>1%) for 0.1%, 0.5%, 1.0%, 3.0%, and 5.0% bitumen emulsion interfacial material [66].

4.3 Possible Species Types Forming Liquid Crystals in SAGD Produced Water

Candidate species are heavily oxygenated. Rice and MacCarthy [67] performed detailed statistical mass based analyses of humic and fulvic acids, and humin from hundreds of samples from diverse sources. Their ranges of atomic ratios are presented in Table 4-1. They overlap with the corresponding ranges and uncertainties of Samples 1-3. Naturally occurring humic substances are potential candidates and they may dominate this fraction of Athabasca bitumen. Other candidate species, listed in Table 4-1, such as naphthenic acids possessing a nominal formula of $C_nH_{2n+z}O_2$ in bitumen [68] have too little oxygen to meet the mass balance constraint and are inconsistent with the ESI/FT-ICR MS results. Further, humic substances have been extracted from oil sands and linked to hydrocarbon resource weathering and processability [69] and are known to be present after desalting [61]. Bitumen and polysaccharides [70] provide other points for comparison and contrast. They illustrate just how different Samples 1-3 are from the bulk composition of bitumen and just how heavily oxygenated they are. This finding paves the way for future work on this topic because it remains unclear whether humic substances form liquid crystals on their own, in water or oil or at oil water interfaces.

Table 4-1 Atomic ratios of samples, bitumen and candidate species

Species	C	H	O	N	S
Sample 1	1	1.22 ± 0.07	0.62 ± 0.02	0.01 ± 0.00	0.02 ± 0.01
Sample 2	1	2.09 ± 0.37	0.83 ± 0.08	0.02 ± 0.02	0.06 ± 0.03
Sample 3	1	1.06 ± 0.07	0.37 ± 0.01	0.02 ± 0.01	0.02 ± 0.01
Bitumen [63, 71]	1	1.400	0.015	0.004	0.024
Naphthenic acid [68]	1	1.40-2.00	0.10-0.20	0	0
Humic acids[67]	1	0.08-1.85	0.08-1.20	0.05	0.01
Fulvic acids [67]	1	0.77-2.13	0.17-1.19	0.04	0.01
Humin [67]	1	0.82-1.72	0.37-0.61	0.06	0.00
Polysaccharides $(C_6H_{10}O_5)n$	1	1.7	0.83	0	0

Chapter 5 Conclusions and Future Work

5.1 Conclusions

- Spherical liquid crystal rich domains that are native to Athabasca bitumen transfer from Athabasca bitumen to SAGD produced water where they are enriched relative to bitumen and suspended inorganic solids. These liquid crystal domains range from 3 μm to 6 μm in diameter and are smaller on average than the domains arising in Athabasca bitumen. Vacuum froth treatment of SAGD produced water separates mineral matter, transferred to the froth, from these liquid crystal rich domains that remain in the water. At a pH less than 3.3, a large fraction of these liquid crystal domains remain suspended in the water while the Athabasca bitumen settles along with a fraction of the liquid crystal domains. The liquid crystal domains present in the froth treated water were not well partitioned from other components by physical separation i.e.: by applying the "coffee ring" effect.
- Samples of the froth treated water (Sample 1), the water suspension and settled residue at a pH of 3.3 (Samples 2 and 3) and edge and centre of "coffee rings" (Samples 4 and 5) were prepared in large enough batches to perform diverse chemical analyses. All five samples are shown to be enriched in oxygen relative to Athabasca bitumen. Sample 2, largely free of bitumen, mineral matter and clay is particularly enriched in oxygen.
- Detailed instrumental analysis revealed that the liquid crystal rich domains have a narrower and lower molar mass range and higher relative abundances of oxygen than found Athabasca bitumen. While there is a broad distribution of oxygen contents and molecular structures represented among the constituents, typical molecules include 4-8 oxygen atoms. Due to limitations in the chemical analysis procedure, and based on the elemental composition data, this is likely to be an underestimate of the average oxygen content of molecules.
- Humic substances including humic and fulvic acids, and humin are the only classes of materials known to be present that possess the correct elemental composition ranges. The liquid crystal domains are attributed to them, at least in part. Other potential candidate species, such as naphthenic acids, do not possess high enough oxygen

contents to match the oxygen mass balance constraint. Other classes of materials may also be present.

- Differences in analytical procedures and the absence of elemental composition data for liquid crystalline materials observed at mined bitumen + water interfaces preclude a definitive comparison between these materials but it would appear that their origins are similar.

5.2 Recommendations for Future Work

- These finding pave the way for future work as it remains unclear whether humic substances form liquid crystals on their own, in water or oil, or at oil water interfaces. Creation of model mixtures including humic substances + water + oil + salts and the observation of their behavior under diverse hydrodynamic conditions with cross polarized light will provide mechanistic insights relevant to oil sands applications and to environmental applications beyond the focus of the current work.
- Attempt to see if liquid crystal rich materials in industrial samples accumulate at oil-water interfaces using high-speed centrifuge but for much longer times. This might prove a better source of liquid crystal enriched samples that are “oil free” than currently realized.
- During sample concentration the question as to whether soluble materials form liquid crystals is an open one. The working hypothesis of the current work did not include this possibility.
- A mass balance on carbon from the raw material to the five samples could be performed. This would provide insights on the representative nature of the samples relative to the feed.

References

1. de Gennes, P.G. and J. Prost, *The physics of liquid crystals.* 2nd ed. The International Series of Monographs on Physics, ed. J. Birman, et al. 1993, New York: Oxford University Press. 597.
2. Simon, J., P. Bassoul, and S. Norvez, *Molecular materials. III. Towards opto-electronics finalities.* New J. Chem., 1989. 13(1): p. 13-31.
3. Brown, G.H. and W.G. Shaw, *The Mesomorphic State - Liquid Crystals.* Chemical Reviews, 1957. 57(6): p. 1049-1157.
4. Syrbu, S., R.Y. Golovanov, and V. Klopov, *Properties of Some Mesogens in the Liquid Crystal and Isotropic States.* Theoretical Foundations of Chemical Engineering, 2003. 37(2): p. 204-206.
5. van der Kooij, F.M., K. Kassapidou, and H.N. Lekkerkerker, *Liquid crystal phase transitions in suspensions of polydisperse plate-like particles.* Nature, 2000. 406(6798): p. 868-871.
6. Andrews, A.B., R.E. Guerra, O.C. Mullins, and P.N. Sen, *Diffusivity of Asphaltene Molecules by Fluorescence Correlation Spectroscopy.* The Journal of Physical Chemistry A, 2006. 110(26): p. 8093-8097.
7. Groenzin, H. and O.C. Mullins, *Asphaltene Molecular Size and Structure.* The Journal of Physical Chemistry A, 1999. 103(50): p. 11237-11245.
8. Groenzin, H. and O.C. Mullins, *Molecular Size and Structure of Asphaltenes from Various Sources.* Energy & Fuels, 2000. 14(3): p. 677-684.
9. Herod, A.A., K.D. Bartle, and R. Kandiyoti, *Characterization of heavy hydrocarbons by chromatographic and mass spectrometric methods: An overview.* Energy & Fuels, 2007. 21(4): p. 2176-2203.
10. Herod, A.A., K.D. Bartle, and R. Kandiyoti, *Comment on a Paper by Mullins, Martinez-Haya, and Marshall "Contrasting Perspective on Asphaltene Molecular Weight. This Comment vs the Overview of A. A. Herod, K. D. Bartle, and R. Kandiyoti".* Energy & Fuels, 2008. 22(6): p. 4312-4317.
11. Martínez-Haya, B., A.R. Hortal, P. Hurtado, M.D. Lobato, and J.M. Pedrosa, *Laser desorption/ionization determination of molecular weight distributions of polyaromatic carbonaceous compounds and their aggregates.* Journal of Mass Spectrometry, 2007. 42(6): p. 701-713.
12. Mullins, O.C., B. Martinez-Haya, and A.G. Marshall, *Contrasting perspective on asphaltene molecular weight. This comment vs the overview of A. A. Herod, K. D. Bartle, and R. Kandiyoti.* Energy & Fuels, 2008. 22(3): p. 1765-1773.
13. Qian, K., K.E. Edwards, M. Siskin, W.N. Olmstead, A.S. Mennito, G.J. Dechert, and N.E. Hoosain, *Desorption and Ionization of Heavy Petroleum Molecules and Measurement of Molecular Weight Distributions.* Energy & Fuels, 2007. 21(2): p. 1042-1047.
14. Wargadalam, V.J., K. Norinaga, and M. Iino, *Size and shape of a coal asphaltene studied by viscosity and diffusion coefficient measurements.* Fuel, 2002. 81(11-12): p. 1403-1407.

15. Bagheri, S.R., A. Bazyleva, M.R. Gray, W.C. McCaffrey, and J.M. Shaw, *Observation of Liquid Crystals in Heavy Petroleum Fractions.* Energy & Fuels, 2010. 24: p. 4327-4332.
16. Bagheri, S.R., et al., *Physical Properties of Liquid Crystals in Athabasca Bitumen Fractions.* Energy & Fuels, 2012. 26(8): p. 4978-4987.
17. Bagheri, S.R., et al., *Observation of Liquid Crystals in Heavy Petroleum Fractions.* Energy & Fuels, 2010. 24(8): p. 4327-4332.
18. Horvath-Svabo, G., J.H. Masliyah, and J. Czarnecki, *Friberg correlations in oil recovery.* Journal of Dispersion Science and Technology, 2006. 27(5): p. 625-633.
19. Czarnecki, J., *Stabilization of Water in Crude Oil Emulsions. Part 2.* Energy & Fuels, 2009. 23: p. 1253-1257.
20. Horváth-Szabó, G., J. Czarnecki, and J.H. Masliyah, *Sandwich Structures at Oil–Water Interfaces under Alkaline Conditions.* Journal of Colloid and Interface Science, 2002. 253(2): p. 427-434.
21. Chuan Qin, *On Organic Liquid Crystal Transfer from Bitumen-Rich to Water-Rich Phases: A Combined Laboratory and SAGD Field Study.* MSc thesis, University of Alberta. 2013.
22. S. Reza Bagheri, Brady Masik, P. Arboleda, Q. Wen, K.H. Michaelian and John M. Shaw, *Physical Properties of Liquid Crystals in Athabasca Bitumen Fractions.* Energy & Fuels, 2012, 26(8): p. 4978-4987.
23. Masik, B.K., *Separation and analysis of liquid crystalline material from heavy petroleum fractions*, in *Department of Chemical and Materials Engineering* 2011, University of Alberta: Edmonton.
24. Campbell, N.L., W.L. Duffy, G.I. Thomas, J.H. Wild, S.M. Kelly, K. Bartle, M. O'Neill, V. Minter, and R.P. Tuffin, *Nematic 2,5-disubstituted thiophenes.* Journal of Materials Chemistry, 2002. 12(9): p. 2706-2721.
25. Petrov, V.F. and A.I. Pavluchenko, *Furan as a structural fragment in liquid crystals.* Molecular Crystals and Liquid Crystals, 2003. 393: p. 1-13.
26. Wilderbeek, H.T.A., M.G.M. van der Meer, M.A.G. Jansen, L. Nelissen, H.R. Fischer, J.J.G.S. Van Es, C.W.M. Bastiaansen, J. Lub, and D.J. Broer, *Synthesis and properties of phenyl benzoate-based and biphenyl-based liquid crystalline thiol-ene monomers.* Liquid Crystals, 2003. 30(1): p. 93.
27. Masliyah, J., et al., *Understanding Water‐Based Bitumen Extraction from Athabasca Oil Sands.* The Canadian Journal of Chemical Engineering, 2004. 82(4): p. 628-654.
28. F. Rao, Q. Liu, *Froth treatment in Athabasca oil sands Bitumen recovery process: a review Energy Fuels,* 27 (2013), p. 7199–7207
29. Czarnecki, J., K. Moran, and X. Yang, *On the "Rag Layer" and Diluted Bitumen Froth Dewatering.* The Canadian Journal of Chemical Engineering, 2007. 85(5): p. 748-755.
30. Jimenez, Jaime. *The Field Performance of SAGD Projects in Canada.* International Petroleum Technology Conference. 2008.
31. Shen, C., *Chapter 17 - SAGD for Heavy Oil Recovery, in Enhanced Oil Recovery Field Case Studies*, S. James, Editor 2013, Gulf Professional Publishing: Boston. p. 413-445.
32. *Long Lake 2011-Surface Performance Presentation*, 2012, Nexen Inc.

33. Wong, T.-S., et al., *Nanochromatography Driven by the Coffee Ring Effect.* Analytical Chemistry, 2011. 83(6): p. 1871-1873.
34. Shen, X., C.-M. Ho, and T.-S. Wong, *Minimal size of coffee ring structure.* The Journal of Physical Chemistry B, 2010. 114(16): p. 5269-5274.
35. Crabtree, R.H. and D.M.P. Mingos, *Comprehensive Organometallic Chemistry III, Volumes 1 - 13*. 2007, Elsevier. p. 208-209.
36. Bagheri, S.R., et al., *Observation of Liquid Crystals in Heavy Petroleum Fractions* Energy & Fuels, 2010. 24(8): p. 4327-4332.
37. Romanova, U. G., et al. *The effect of oil sands bitumen extraction conditions on froth treatment performance.* Journal of Canadian Petroleum Technology, 2006, 45(9): p. 36-45.
38. Sundeep SrinivasaRajagopalan, *Study of Bitumen Liberation from Oil Sands Ores,* MSc thesis, University of Alberta. 2010.
39. S. Basu, K. Nandakumar andJacob H. Masliyah*, *On bitumen liberation from oil sands.* The Canadian Journal of Chemical Engineering, April 1997, 75(2): p. 476–479.
40. Sun P1, Ma R, Wang K, Zhong M, Wei J, Wu D, Sasaki T, Zhu H. *Suppression of the coffee-ring effect by self-assembling graphene oxide and monolayer titania.* Nanotechnology, 2013. 24(7).
41. Pella, E.; Colombo, B., *Simultaneous C-H-N and S microdetermination by combustion and gas chromatography.* Mikrochimica Acta, 1978. 69(3-4): p. 271-286.
42. Pella, E.; Andreoni, R., *Developments in the determination of organic oxygen by pyrolysis-gas chromatography.* Mikrochimica Acta, 1976. 66(1-2): p. 175-184.
43. Chua Ai Ming, Tokura Takako. *High Sensitivity Total Organic Carbon Analysis.* Customer Support Centre, Shimadzu (Asia Pacific) Pte Ltd. Shimadzu publication number AD-0007-TOC, July 2003.
44. Daniel P. Hautman, David J. Munch. *Method 300.1 The Determination of Inorganic Anions in Water by Ion Chromatography;* revision 1.0; USEPA, Office of Water, 1997
45. *Standard methods for the examination of water and wasterwater,* 20th Ed, 4500-Silica F, American Water Works Association, 1999.
46. Ruth E. Wolf, Ph.D., *Introduction to ICP-MS.* Research Chemist, USGS/CR/CICT, March 2005
47. Perkin Elmer Instruments. *The 30-Minute Guide to ICP-MS.* 2001
48. Thermo Nicolet Corporation. *Introduction to Fourier Transform Infrared Spectrometry.* 2001
49. R. L. Barbour, R. J. Jakobsen, W. Henry. *Inorganic compound speciation by Fourier transform infrared (FTIR).*SPIE Fourier Transform Infrared Spectroscopy. 1981. 289: p. 245-250
50. Qian, K; Robbins, W. K.; Hughey, C. A.; Cooper, H. J.; Rodgers, R. P.; Marshall, A. G., *Resolution and Identification of Elemental Compositions for More than 3000 Crude Acids in Heavy Petroleum by Negative-Ion Microelectrospray High-Field Fourier Transform Ion Cyclotron Resonance Mass Spectrometry.* Energy and Fuels, 2001. 15(6): p. 1505-1511

51. Sunghwan Kima, Ryan P. Rodgersb, Greg T. Blakneyb, Christopher L. Hendricksonb, Alan G. Marshallb. *Automated Electrospray Ionization FT-ICR Mass Spectrometry for Petroleum Analysis.* Journal of the American Society for Mass Spectrometry. 2009. 20(2)
52. Marshall, A.G. and Rodgers, R.P. *Petroleomics: chemistry of the underworld.* Proc. Natl. Acad. Sci. USA. 2008. 105: p. 18090–18095
53. Purcell, J.M., C.L. Hendrickson, R.P. Rodgers, and A.G. Marshall, *Atmospheric Pressure Photoionization Fourier Transform Ion Cyclotron Resonance Mass Spectrometry for Complex Mixture Analysis.* Analytical Chemistry, 2006. 78(16): p. 5906-5912.
54. Bruker Daltonics Inc. apex-Qe User Manual. Version 1.0 (May 2007).
55. Ryan P. Rodgers. *Advanced Mass Spectrometry's Contribution to the "Petroleome" Presentation.* National High Magnetic Field Lab Florida State University, USA
56. Shi, Q.*, Pan, N., Liu, P., Chung, K. H., Zhao, S., Zhang, Y., and Xu, C.*, *Characterization of Sulfur Compounds in Oilsands Bitumen by Methylation Followed by Positive-Ion Electrospray Ionization and Fourier Transform Ion Cyclotron Resonance Mass Spectrometry.* Energy & Fuels, 2010. 24(5): p. 3014-3019.
57. Panda SK, Andersson JT, Schrader W. *Mass-spectrometric analysis of complex volatile and nonvolatile crude oil components: A challenge.* Anal Bioanal Chem, 2007. 389: p. 1329–1339.
58. Kendrick E. *A mass scale based on CH2=14.0000 for high resolution mass spectrometry of organic compounds*. Anal Chem, 1963, 35(13): 2146-2154.
59. Hughey CA, Hendrickson CL, Rodgers RP, Marshall AG, Qian K. *Kendrick Mass Defect Spectrum: A Compact Visual Analysis for Ultrahigh-Resolution Broadband Mass Spectra*. Anal. Chem. 2001.73: p. 4676–4681
60. Barbara H. Stuart, John Wiley & Sons. *Infrared Spectroscopy: Fundamentals and Applications.* 2004. 5: p. 95-110
61. Yongyong Li, Chunming Xu, Keng H. Chung, and Quan Shi. *Molecular Characterization of Dissolved Organic Matter and Its Sub-fractions in Refinery Process Water by FT-ICR MS*. Energy & Fuels, 2010, accepted. DOI: 10.1021/acs.energyfuels.5b00333
62. Thurman, E. M. and Malcolm, R. L. *Preparative Isolation of Aquatic Humic Substances*. Environmental Science & Technology. 1981, 15(4): p. 463-466.
63. Donald F. Smith, Tanner M. Schaub, Sunghwan Kim, Ryan P. Rodgers, Parviz Rahimi, Alem Teclemariam, and Alan G. Marshall.*Characterization of Acidic Species in Athabasca Bitumen and Bitumen Heavy Vacuum Gas Oil by Negative-Ion ESI FT-ICR MS with and without Acid-Ion Exchange Resin Prefractionation.* Energy & Fuels, 2008, 22: p. 2372–2378
64. S. Lababidi, S. K. Panda, J. T. Andersson, and W. Schrader. *Deep Well Deposits: Effects of Extraction on Mass Spectrometric Results*. Energy & Fuels, 2013, 27: p. 1236-1245
65. S. Lababidi, S. K. Panda, J. T. Andersson, and W. Schrader. *Direct Coupling of Normal-Phase High-Performance Liquid Chromatography to Atmospheric Pressure Laser Ionization Fourier Transform Ion Cyclotron Resonance Mass*

Spectrometry for the Characterization of Crude Oil Samples. Analytical Chemistry, 2013, 85: p. 9478-9485

66. Lateefah A. Stanford, Ryan P. Rodgers and Alan G. Marshall. *Compositional Characterization of Bitumen/Water Emulsion Films by Negative- and Positive-Ion Electrospray Ionization and Field Desorption/Ionization Fourier Transform Ion Cyclotron Resonance Mass Spectrometry.* Energy & Fuels. 2007, 21: p. 963-972
67. James A. Rice and Patrick MacCarthy. *Statistical evaluation of the elemental composition of humic substances*. Org. Geochem. 1991, 17(5): p. 635-648
68. John V. Headley and Dena W. McMartin. *A Review of the Occurrence and Fate of Naphthenic Acids in Aquatic Environments.* Journal of environmental science and health Part A—Toxic/Hazardous Substances & Environmental Engineering. 2004, A39(8): p. 1989–2010
69. Leopoldo Gutierrez, Marek Pawlik. *Influence of humic acids on oil sand processing. Part I: Detection and quantification of humic acids in oil sand ores and their effect on bitumen wettability.* International Journal of Mineral Processing. 2014, 126: p. 117–125
70. Pettit R E. *Organic matter, humus, humate, humic acid, fulvic acid and humin: their importance in soil fertility and plant health*. 2004, Available at www.humate.info/mainpage.htm
71. Bazyleva, A.B., et al., *Bitumen and Heavy Oil Rheological Properties: Reconciliation with Viscosity Measurements.* Journal of Chemical & Engineering Data, 2009. 55(3): p. 1389-1397.